

# **Study of Microstructure and Mechanical Properties of Aluminium Alloy Cast Through Rapid Slurry Formation (RSF) Process**

Ph.D. THESIS

by

**Robin Gupta**  
(Id: 2012RMT9044)



**DEPARTMENT OF METALLURGICAL AND MATERIALS ENGINEERING  
MALAVIYA NATIONAL INSTITUTE OF TECHNOLOGY JAIPUR,  
JAIPUR-302017, RAJASTHAN (INDIA)**

**October 2017**

**Study of Microstructure and Mechanical Properties of Aluminium  
Alloy Cast Through Rapid Slurry Formation (RSF) Process**

A THESIS

Submitted in partial fulfillment of the  
requirements for the award of degree

*of*

**DOCTOR OF PHILOSOPHY**

in

**METALLURGICAL AND MATERIALS ENGINEERING**

*by*

**Robin Gupta**  
(ID: 2012RMT9044)



**DEPARTMENT OF METALLURGICAL AND MATERIALS ENGINEERING  
MALAVIYA NATIONAL INSTITUTE OF TECHNOLOGY JAIPUR,  
JAIPUR-302017, RAJASTHAN (INDIA)**

**October 2017**



*This thesis is dedicated to*

*My Parents: Sh. Shyam Lal & Smt. Narendra Gupta*

*My Wife: Rekha*

*My Son: Aarav Gupta*

*For their unconditional love, support and especially never ending patience*





**DEPARTMENT OF METALLURGICAL AND MATERIALS  
ENGINEERING  
MALAVIYA NATIONAL INSTITUTE OF TECHNOLOGY JAIPUR,  
RAJASTHAN (INDIA)**

**CERTIFICATE**

This is to certify that the thesis entitled “**Study of Microstructure and Mechanical Properties of Aluminium Alloy Cast Through Rapid Slurry Formation (RSF) Process**” is being submitted by me for the award of the degree of **Doctor of Philosophy** in Metallurgical and Materials Engineering, Malaviya National Institute of Technology Jaipur, is an original research work carried out by me. The content of the thesis has been checked using software “Plagiarism Detector”.

I have incorporated all the suggestions/queries/changes raised by the Examiner in the Thesis Evaluation Reports.

**(Robin Gupta)**

This is to certify that above statement made by the candidate is true to our knowledge.

**Prof. Dr. Ashok Sharma**  
**(Supervisor)**

**Prof. Dr. Upender Pandel**  
**(Joint Supervisor)**

Ph.D. viva-voce examination of Mr. Robin Gupta, Research Scholar, was held on 31-10-2017 in the seminar hall of the Department of Metallurgical and Materials Engineering, MNIT Jaipur. The candidate defended the viva-voce successfully to the satisfaction of Oral Defense Committee. The Committee recommends for the award of Ph.D. Degree.

**Signature of Supervisor(s)**

**Signature of External Examiner**

# ACKNOWLEDGEMENTS

---

First I would like to express my earnest gratitude and humble regards to my supervisors **Prof. Dr. Ashok Sharma, Prof. Dr. Upender Pandel, Prof. Dr. Lorenz Ratke** who provided me precious opportunity to pursue research under their guidance. Their guidance put me on a new platform of wonderful and challenging materials world. Their unique guiding quality, interest, working enthusiasm and analytical approach towards the experimental results impressed me so much. It is great honour for me to work with them. I would like to express my sincere thanks to **Prof. Dr. A. K. Bhargava and Dr. R. K. Duchaniya** for being in my DREC committee as well as for their encouragement, analytical insights and recommendations. I would like to thanks to **Mr. Lalchand Kumawat (Sr. Technician)** of department of Metallurgical and Materials Engineering, MNIT Jaipur for their help during PhD work.

I further extend my thanks to all the staff members of **Materials Research Center (MNIT Jaipur) and MSE (IIT Kanpur)** for providing characterization facilities. I express my deep appreciation to my friends and co-workers **Dr. Pramod Kumar Sain, Dr. Ornov Maulik, Dr. Avnish Kumar, Mr. Sachin Rathi, Mr. Anurag Hamilton, Dr. Vatsala Chaturvedi, Mr. Ankit Goyal, Mr. Arun Kumar, Dr. Anil Kumar, Mr. Akshay Kumar** and the post graduate students of the department of Metallurgical and Materials Engineering, MNIT Jaipur for their moral support and help. I would like to extend my sincere thanks to all the faculty and staff members of MNIT, Jaipur for their support during my Ph.D.

I would like to thank my parents and my family members for their unconditional love and support. Without them, this thesis would not be possible.

(Robin Gupta)

## ABSTRACT

---

In this thesis, experimental work for preparation of semi-solid slurry having globular morphology by rheometal process was carried out. Detailed study on A356 alloy at different stirring speeds (400, 600, 800, 1000 and 1200 rpm) was carried out. Analysis about variation in surface morphology of EEM during stirring at different time intervals (0, 5, 10, 15, 20, 25 and 30 sec) was also examined. Evolution of microstructure was observed using optical micrographs and scanning electron microscope (SEM). The microstructure exhibited network of eutectic Si surrounding the primary  $\alpha$ -Al phase. The average grain size of primary  $\alpha$ -Al phase decreased for stirring speed up to 1200 rpm. However at 1200 rpm high turbulence creates chance of entrapment for gas porosity. Therefore, best results in terms of average grain size and shape factor were obtained at 1000 rpm. The results revealed that as stirring time increased,  $\alpha$ -Al phase changed its morphology from dendritic to rosette to globular morphology for stirring time of 25 sec. The effect of flow pattern of the morphology of primary  $\alpha$ -Al phase was examined with baffles. Without baffle, crucible produced swirling motion and because of this vortex formation takes place which lacks adequate mixing. The use of baffles suppress vortex formation and convert swirling motion into preferred flow pattern so that proper mixing may takes place. A varying amount of Al-5Ti-1B master alloy (0.2, 0.4, 0.6 and 0.8 wt.%) was added to melt in conventional casting method. Results showed that up to 0.6 wt% of grain refiner the secondary dendritic arm spacing (SDAS) continuously decreased but for 0.8 wt.% SDAS increased. Hence, 0.6 wt.% of grain refiner was found optimum grain refiners as regards of SDAS value. Therefore, 0.6 wt.% grain refiner was further used in rheometal process. The addition of grain refiner to melt in rheometal process provides additional benefit to already refined structure due to the stirring of melt. Rate of coarsening kinetics was discussed with respect to conventional diffusional Lifshitz, Slyozov and Wagner (LSW) theory, coarsening by convective mass flow and coalescence by stirring speed. The rate of coarsening kinetics was found to be faster than predicted by diffusional LSW theory, but slower than predicted by convective mass flow. Effect of T5 heat treatment on microstructure, mechanical properties and wear analysis of A356 alloy in different processing conditions was observed. T5 heat treatment leads to refinement of  $\alpha$ -Al phase and Si needles, precipitation of  $Mg_2Si$  which improved the mechanical properties and wear resistance of the alloy when compared with their respective non-heat-treated alloy. Results showed that rheometal process with the use of baffles, addition of grain refiner and T5 heat treatment had improved the mechanical properties and wear resistance over other processing

conditions. X-Ray diffraction (XRD), SEM and differential scanning calorimetry (DSC) were employed to support the results during experimentation.

## Table of Content

---

Chapter	Page No.
<b>Chapter 1 Introduction</b>	1
1.1 Background	1
1.2 Outline of Thesis	3
1.3 Advantages of Rheometal Process	4
1.4 Industrial Applications of Rheometal Process	4
<b>Chapter 2 Literature Review</b>	5
2.1 Principle of Solidification	5
2.1.1 Homogenous nucleation	5
2.1.2 Heterogeneous nucleation	6
2.1.3 Solidification of alloy	8
2.2 Grain Refinement	15
2.2.1 Theories for grain refinement	16
2.3 Semi-Solid Metal Processing	18
2.3.1 Thixocasting	18
2.3.2 Rheocasting	19
2.4 Rheology	23
2.4.1 Fundamentals of rheology	24
2.4.2 Principle of rheology	27
2.4.3 Effective parameters of rheology	27
2.5 Coarsening Mechanism of SSM Process	35
2.6 Mechanical Properties of Cast Al-Si Alloys	39
2.7 Wear	40
2.7.1 Types of wear	40
2.7.2 Wear analysis of A356 alloy	42

2.8 Objectives of Present Study	43
<b>Chapter 3 Materials and Methods</b>	<b>44</b>
3.1 Synthesis of A356 Alloy	44
3.2 Preparation of Enthalpy Exchange Material (EEM)	44
3.3 Synthesis of Semi-Solid Slurry	45
3.3.1 Without grain refiner	45
3.3.2 Addition of Al-5Ti-1B master alloy	47
3.4 Heat Treatment	48
3.5 Characterization of A356 Alloy	49
3.5.1 Microstructural analysis	49
3.5.2 Porosity measurement	49
3.5.3 X-Ray diffraction (XRD) analysis	50
3.5.4 Thermal analysis	50
3.5.5 Scanning electron microscopy (SEM)	50
3.6 Mechanical Properties	50
3.6.1 Hardness	50
3.6.2 Tensile properties	51
3.6.3 Fractography	52
3.7 Wear Analysis	52
<b>Chapter 4 Microstructures Evolution Through RSF Process</b>	<b>55</b>
4.1 Effect of Time on EEM Dissolution During Stirring	55
4.2 Effect of Stirring Speed on Microstructure; Without and With baffles	58
4.3 XRD Analysis	66
4.4 Thermal Analysis	67
4.5 Coarsening Kinetics: Without Baffles	69

4.6 Coarsening Kinetics: With Baffles	77
4.7 Effect of Solid Fraction	79
4.8 SEM Analysis of Al-5Ti-1B Master Alloy	81
4.9 Effect of Grain Refiner in Conventional Cast A356 Alloy	82
4.10 Comparison of A356 Alloy in Different Processing Conditions	84
4.10.1 XRD analysis	84
4.10.2 Microstructural observations	85
<b>Chapter 5 Mechanical Properties (Without and With Heat Treatment)</b>	<b>87</b>
5.1 Microstructural Observations	87
5.2 XRD Analysis	89
5.3 Effect of Heat Treatment on Porosity	90
5.4 Mechanical Properties	91
5.5 Effect of Heat Treatment on the Morphology of Eutectic Si	96
5.6 EDS Analysis	97
5.7 Fractography	98
5.8 Wear Analysis	101
5.8.1 Analysis of specific wear rate	101
5.9 SEM Analysis of Worn Surfaces	102
5.10 Analysis of Wear Debris	106
<b>Chapter 6 Conclusions and Future Work</b>	<b>108</b>
<b>References</b>	<b>111</b>
<b>Appendix</b>	<b>123</b>

## List of Figure

Figure No.	Caption	Page No.
Fig. 2.1	Change in Gibb's free energy for homogeneous nucleation	6
Fig. 2.2	Heterogeneous nucleation of spherical cap on a flat mold wall	7
Fig. 2.3	Free energy curve for homogeneous and heterogeneous nucleation	8
Fig. 2.4	Constitutional undercooling on solidification	9
Fig. 2.5	Phase diagram of Al with an element B	10
Fig. 2.6	Solidification under equilibrium conditions	11
Fig. 2.7	Solidification in non-equilibrium conditions	12
Fig. 2.8	Advancing solid-liquid interface having initial solute concentrations $C_S$ and $C_L$ in solid and liquid respectively	13
Fig. 2.9	Variation of grain size with growth restriction factor	17
Fig 2.10	Schematic illustration of thixocasting process	19
Fig. 2.11	Schematic diagram for direct slurry formation process	20
Fig. 2.12	Schematic illustration of new rheocasting (NRC) process	21
Fig. 2.13	Schematic representation of SSR process	21
Fig.2.14	Continuous rheocasting process	22
Fig. 2.15	Schematic illustration of rheometal process	23
Fig. 2.16	Different types of fluid behavior	25
Fig. 2.17	Comparison between proposed model and the conventional Herschel-Bulkley model	27
Fig. 2.18	Apparent viscosity vs solid fraction of Sn-15Pb alloy sheared continuously and cooled at $0.33\text{K min}^{-1}$ at different shear rates $\dot{\gamma}_0$	28
Fig. 2.19	Variation of apparent viscosity with solid fraction (at shear rate $266\text{ sec}^{-1}$ )	29
Fig. 2.20	Effect of EEM amount on the average grain size	30
Fig. 2.21	Steady state apparent viscosity vs. shear rate in Sn-15Pb alloy for various solid fractions $f_s$	31
Fig. 2.22	Slurry microstructures produced at (a) 600 (b) 1200 and (c) 1800 rpm for solid fraction 5% and temperature $627\text{ }^\circ\text{C}$	32
Fig. 2.23	Effect of rotation speed on the average grain size	32



Fig. 2.24	Morphology of primary phase in ZL101 alloy obtained at various pouring temperature (a) 650 (b) 630 and (c) 615 °C with slightly electromagnetic stirring	33
Fig. 2.25	Microstructure of water quenched melt	34
Fig. 2.26	Microstructure of Al-7Si-0.6Mg with stirring at temperature (a) 605 (b) 600 (c) 590 and (d) 580 °C	35
Fig. 2.27	Microstructures of ingots (a) cast over the cooling plate with a pouring temperature of 640 °C and a cooling length of 400 mm and after isothermal holding at 580 °C for (b) 5, (c) 15 and (d) 30 min	36
Fig. 2.28	The optical micrograph of the processed specimens after soaking at 590 °C for different durations, (a) 3, (b) 6, (c) 10 and (d) 15 min	37
Fig. 2.29	Evolution of cube of average globule diameter as function of isothermal soaking time at 610–631 °C in semi-solid state for different materials	38
Fig. 3.1	Schematic set-up for rheometal process	46
Fig. 3.2	Schematic illustration of different stage involved in rheometal process	46
Fig. 3.3	Schematic representation of die used in rheometal process	48
Fig. 3.4	Schematic depiction of the Brinell indentation	51
Fig. 3.5	Dimensions of tensile sample	51
Fig. 3.6	Schematic representation of pin on disc apparatus	53
Fig. 3.7	Flow chart for materials and methods used in rheometal process	54
Fig. 4.1	Optical micrographs of EEM for primary $\alpha$ -Al phase at stirring time (a) 0, (b) 5, (c) 10, (d) 15, (e) 20 and (f) 25 seconds	56
Fig. 4.2	Weight of EEM with different stirring time	57
Fig. 4.3	SEM micrographs of EEM for eutectic Si at stirring time (a) 0, (b) 5, (c) 10, (d) 15, (e) 20 and (f) 25 seconds	58
Fig. 4.4	Typical flow pattern in (a) unbaffled and (b) baffled crucible	61

Fig. 4.5	Optical micrographs of (a) as-cast, stirred at (b) 400, (c) 600, (d) 800, (e) 1000 and (f) 1200 rpm water quenched semi-solid slurry at 0 min holding time	62
Fig. 4.6	Effect of stirring speed on average grain size and shape factor of primary $\alpha$ -Al phase	63
Fig. 4.7	Microstructures of rheometal processed A356 alloy (a) without and (b) with baffle stirred at 1000 rpm	64
Fig. 4.8	Effect of stirring speed on morphology of eutectic silicon for (a) as-cast (b) 400 (c) 600, (d) 800, (e) 1000 and (f) 1200 rpm at 30% solid fraction and 0 min holding time	65
Fig. 4.9	XRD analysis for (a) as-cast and (b) 1000 rpm, 0 min in A356 alloy	67
Fig. 4.10	DSC analysis for as-cast and 1000 rpm, 0 min in A356 alloy	68
Fig. 4.11	Microstructure of RSF processed A356 alloy at different rpm with different holding times	70
Fig. 4.12	Variation of average grain size in A356 alloy with stirring speed and holding time	72
Fig. 4.13	Variation of cube of mean particle size with holding time	73
Fig. 4.14	Variation of square of mean particle size with holding time	75
Fig. 4.15	Microstructure of RSF processed A356 alloy (a) without and (b) with baffle stirred at 1000 rpm but with different holding times	78
Fig.4.16	Microstructure of RSF processed alloys at (a) 20 (b) 30 (c) 40 wt.% solid fraction for 1000 rpm, 0 min	79
Fig. 4.17	Effect of solid fraction on average grain size and shape factor of $\alpha$ -Al particles	80
Fig. 4.18	Effect of solid fraction (a) 20, (b) 30 and (c) 40 wt.% on Si morphology	81
Fig. 4.19	SEM micrographs of Al-5Ti-1B master alloy with X-ray mapping	82
Fig. 4.20	Microstructures of A356 alloy with varying content (a) 0.2, (b) 0.4, (c) 0.6 and (d) 0.8 wt.% grain refiner	83

Fig. 4.21	Effect of grain refiner on SDAS of A356 alloy	84
Fig. 4.22	XRD pattern for (a) Al-5Ti-1B master alloy, (b) as-cast, (c) conventional cast and (d) RSF cast A356 alloy	85
Fig. 4.23	Microstructures of RSF processed A356 alloy sheared at 1000 rpm for (a) without and (b) with 0.6% Al-5Ti-1B grain refiner	86
Fig. 5.1	Microstructure of RSF non-heat-treated samples (a) A, (b) B, (c) C, (d) D and (e) E	88
Fig. 5.2	Microstructure of RSF heat-treated samples (a) A, (b) B, (c) C, (d) D and (e) E	89
Fig. 5.3	XRD of A356 alloy for (a) non-heated sample A, (b) heat-treated sample A, (c) non-heated sample E and (d) heat-treated sample E	90
Fig. 5.4	Effect of heat treatment on porosity in different processing conditions	91
Fig. 5.5	Effect of heat treatment on hardness of A356 alloy	92
Fig. 5.6	Effect of heat treatment on (a) tensile strength, (b) yield strength and (c) elongation of A356 alloy	93
Fig. 5.7	Quality index (QI) of A356 alloy in different processing conditions	95
Fig. 5.8	Morphology of eutectic Si in non-heat-treated (a) as-cast and (b) baffle with grain refiner	96
Fig. 5.9	Morphology of eutectic Si in heat-treated (a) as-cast and (b) baffle with grain refiner	97
Fig. 5.10	EDS analysis of non-heat-treated sample E	97
Fig. 5.11	EDS analysis of heat-treated sample E	98
Fig. 5.12	Fracture surface of RSF non-heat-treated A356 alloy in different processing conditions; (a) A, (b) B, (c) C. (d) D and (e) E	99
Fig. 5.13	Fracture surface of RSF heat-treated A356 alloy in different processing conditions; (a) A, (b) B, (c) C. (d) D, (e) E	100
Fig. 5.14	Specific wear rate in various processing conditions	101

Fig. 5.15	SEM micrographs of worn surfaces for non-heat-treated samples (a) A, (b) B, (c) C, (d) D and (e) E	103
Fig.5.16	SEM micrographs of worn surfaces for heat-treated samples (a) A, (b) B, (c) C, (d) D and (e) E	105
Fig. 5.17	SEM micrographs of worn surfaces for non-heat-treated samples (a) A, (b) E and (c) heat- treated sample E	106

---

## List of Table

<b>Table No.</b>	<b>Caption</b>	<b>Page No.</b>
Table 3.1	Chemical composition of A356 alloy	44
Table 3.2	Dimensions of EEM for different solid fractions	45
Table 3.3	Weight of EEM after dissolution in melt with different stirring time	47
Table 3.4	Different conditions used for mechanical properties	49
Table 3.5	Experimental parameters used for wear analysis	53
Table 4.1	Data obtained from DSC curve	68
Table 4.2	Experimental value of coarsening rate constant (K)	74
Table 4.3	Experimental value of coarsening rate constant due to convective mass flow (K)	75

## List of Abbreviations

SSMP	Semi-solid metal processing
DSF	Direct slurry forming
NRC	New-rheocasting
SSR	Semi-solid rheocasting
CRP	Continuous rheocasting process
RSF	Rapid slurry formation
EEM	Enthalpy exchange material
GR	Grain refiner
SDAS	Secondary dendritic arm spacing ( $\mu\text{m}$ )
ASTM	American society for testing and materials
OM	Optical micrographs
XRD	X-ray diffraction
SEM	Scanning electron microscope
EDS	Energy Dispersive X-Ray Spectroscopy
DSC	Differential scanning calorimetry
YS	Yield strength (MPa)
UTS	Ultimate tensile strength (MPa)
GRF	Growth restriction factor
LSW	Lifshitz, Slyozov and Wagner

# CHAPTER 1

## INTRODUCTION

---

### 1.1 Background

Light-weight materials like Al alloys have a vital role in improving fuel economy and reducing vehicle weight in the automotive sector. Aluminum alloys are widely used in aerospace and automobile industries. Aluminium alloys with silicon exhibit high strength, and high wear resistance. These qualities, together with their excellent castability, make these alloys very interesting for the automotive industry [1-2].

Semi-solid metal (SSM) processing allows to manufacturing cast alloys with a non-dendritic morphology. In SSM process material is partially solid and partially liquid. The material as a whole, a composite of liquid and solid behaves neither as a liquid nor as a solid, but something in between. Two well-known SSM processing routes known as rheocasting and thixoforming have been developed. Thixoforming is used to describe the near net shaping of a partially melted non-dendritic alloy slug within a metal die: thixocasting if in a closed die or thixoforging if in an open die [3]. Rheocasting is a semi-solid process in which slurry exhibits a globular morphology owing to application of shear forces [3]. Since in any rheocasting processes slurry is cast into molds, the preparation of slurry is an essential part of any rheocasting process. A special method to prepare slurry rapidly and cost effectively was developed a decade ago by Wessen and co-workers and is known as rapid slurry formation (RSF) or Rheometal process after the company selling this technology on the market [4].

In the rheometal process semi-solid slurry is prepared by immersing specified amount of solid alloy (having the same composition like melt) in the melt. The solid alloy is known as enthalpy exchange material (EEM) and also serves as an internal cooling agent and simultaneously as a stirrer. In this process enthalpy exchange between a superheated melt and EEM takes place. As the EEM extracts heat from the surrounding melt and melts by itself, the slurry is generated having globular morphology [4].

A356 alloy exhibits good mechanical properties and is required for producing the parts having high strength to weight used. A356 alloy also has wide applications in the automotive and aerospace sector [5].

In RSF process, rheology of melt plays a critical role in deciding the quality of semi-solid mass and subsequently the mechanical properties of cast component. There are various process parameters such as stirring time, solid fraction, and shear rate which influence the rheological characteristics of liquid and also the properties of solidified alloy. Therefore, a detailed study is required, so that desired microstructure and mechanical properties can be obtained by this process.

When stirring of the liquid is carried out, due to rotation flow turbulent eddies may take place, which leads to vortex formation. Vortex formation causes air aspiration of gases. To avoid the vortex formation baffles are used. Baffles impede rotational flow and diminished unwanted flow so that proper mixing takes place. Therefore, in present investigation baffles are used to enhance quality of casting [5].

The grain size is an important quality characteristic for a sound casting and grain size affect the mechanical properties of the alloy. It is desirable to have small grains since a fine-grained structure in a casting ensures high mechanical properties, improves feeding to eliminate shrinkage porosity and micro-porosities. Therefore, grain refinement is one of the effective treatments widely used to improve the quality of the casting. The grain refiners commonly used in aluminum industry are master alloy of Al-Ti, Al-Ti-B, and Al-Ti-C for the grain refinement [2]. In the current research work a varying amount of Al-5Ti-1B master alloy (0.2, 0.4, 0.6 and 0.8 wt.%) was added to melt in conventional casting method. Results showed that upto 0.6 wt% of grain refiner the secondary dendritic arm spacing (SDAS) continuously decreased but for 0.8 wt.% SDAS increased. Hence, 0.6 wt.% of grain refiner was found optimum grain refiners as regards of SDAS value. Therefore, 0.6 wt.% grain refiner was further used in the rheometal process. The addition of grain refiner to melt in the rheometal process provides additional benefit to already refined structure due to the stirring of the melt. Effects of T5 treatment (artificial aging at 170°C for 20 hrs) on microstructures and mechanical properties were investigated. T5 heat treatment led to further refinement of  $\alpha$ -Al phase and Si needles, precipitation of Mg<sub>2</sub>Si phase, which further improved the mechanical properties of the alloy when compared to respective non-heat-treated conditions. Comparisons between microstructure and mechanical properties of non-heat-treated and heat-treated A356 alloy in different processing conditions was also conceded. The Quality Index (QI) for the A356 alloy in various processing conditions was measured. Wear studies on the same processing conditions were also carried out. Characterizations were



employed with optical micrographs (OM), X-ray diffractometer (XRD), Scanning electron microscope (SEM) and Differential scanning calorimetry (DSC).

## 1.2 Outline of Thesis

The thesis has been divided into six chapters.

**Chapter 1** includes the background and outline of current work. It also includes advantages and industrial applications of the rheometal process.

**Chapter 2** contains the fundamental aspects of solidification, grain refinement, semi-solid metal processing and rheology. Study about the different process of rheocasting such as direct slurry formation (DSF), sub-liquidus casting (SLC), new rheocasting (NRC), continuous rheocasting (CRP) and rheometal process takes place. This chapter covers the relevant literature about the effect of different process parameters on apparent viscosity of the semi-solid slurry. A brief review of mechanical properties and wear analysis is presented.

**Chapter 3** deals with the materials and methods used in the thesis. The chapter is separated into two parts. First part is concerned about the synthesis of A356 alloy, preparation of enthalpy exchange material (EEM), synthesis of semi-solid slurry with and without grain refiner and heat treatment of the semi-solid mass. The second part provides information about various characterization techniques used in the thesis.

**Chapter 4** This chapter discusses microstructure evolution based on different process parameters for the A356 alloy in the rheometal process. The effect of stirring time on the morphology of primary  $\alpha$ -Al is also observed. A comparative study of casting without and with the use of baffle has been carried out. Optimization of grain refiner with different wt.% of Al-5Ti-1B in conventional cast A356 alloy has also taken place. The addition of optimum grain refiner in rheometal cast A356 alloy has been made to observe the effect of grain refiner on the morphology of primary  $\alpha$ -Al phase.

**Chapters 5** deals with the mechanical properties and wear analysis of A356 alloy (with and without heat treatment) under different processing conditions.

**Chapter 6** presents the conclusions derived from present research work and suggestions for future work.

**Appendix** (I – VII) introduce the charge calculation, the mass of EEM, Reynolds number, parameters for coarsening rate constant, the calculation for  $K_{\text{calculated}}$  used in diffusive mass flow, calculations for  $K_{\text{calculated}}$  used in convective mass flow and a list of publications.

### **1.3 Advantages of Rheometal Process**

Rheometal process exhibits several advantages

- (i) Modification of dendritic structure into a globular structure.
- (ii) Weight saving and near net shape.
- (iii) Good mechanical properties and wear resistance.
- (iv) High productivity and increased die life [6-7].

### **1.4 Industrial Applications of Rheometal Process**

There are two companies which are working on the concept of rheometal process and producing many types of equipment- Fujian Rheomet Light Metal Co. Ltd., China and Rheometal, Sweden. These companies are specialized in manufacturing of light alloy castings, vehicle parts (e.g. vehicle hub and air compressor scroll), automobile parts, medical equipment and communication devices [6-7].

# CHAPTER 2

## LITERATURE REVIEW

---

This chapter contains the fundamental aspects of solidification, grain refinement, semi-solid metal processing and rheology. This chapter covers the relevant literature about the effects of different process parameters on the apparent viscosity of a semi-solid slurry. Review of mechanical properties and wear analysis are also presented briefly.

### 2.1 Principle of Solidification

While a liquid metal is cooled from a temperature above its melting point or for alloys above the liquidus temperature, solidification takes place once these temperatures are passed by a few degrees. Solidification, the transformation of a liquid to a solid, starts with nuclei of the solid phase, which grow into the melt determined essentially by the rate of heat extraction and in alloys by the solute redistribution both in the melt and the growing solid. Most often, melts are cast into molds (permanent, sand, ceramic shells etc.) and solidification always starts at the mold walls and the solidification front moves inward, essentially perpendicular to the melting or liquidus temperature isotherm [8-9].

#### 2.1.1 Homogeneous nucleation

When pure metal cools in a liquid state, then it transforms in a solid state at fixed temperature. Thermodynamically for pure metals, there is only one temperature where solid and liquid can co-exist [10]. Critical radius and free energy for homogeneous nucleation can be given as

$$r_{homogeneous}^* = \frac{-2 \gamma_{sl}}{\Delta G_v} \quad (2.1)$$

$$\Delta G^* = \frac{16}{3} \frac{\pi \gamma_{sl}^3}{(\Delta G_v)^2} \quad (2.2)$$

Where,  $\gamma_{sl}$  is the surface energy (J/m<sup>2</sup>) of solid–liquid interface. For an undercooling  $\Delta T$ , per unit volume, Gibb's free energy  $\Delta G_v$  can be approximated as

$$\Delta G_v = \Delta T \Delta S = \frac{\Delta H_f \Delta T}{T_m} \quad (2.3)$$

$\Delta T$  = undercooling (K) below liquidus temperature,  $\Delta S$  = change in entropy (J/K/m<sup>3</sup>) for liquid to solid phase transformation,  $\Delta H_f$  = enthalpy of solidification and  $T_m$  = temperature of melting. If embryo of solid is bigger than the critical radius ( $r^*$ ), then the embryo survives and develop into a nucleus [11]. Figure 2.1 shows the change in Gibb's free energy for homogeneous nucleation.

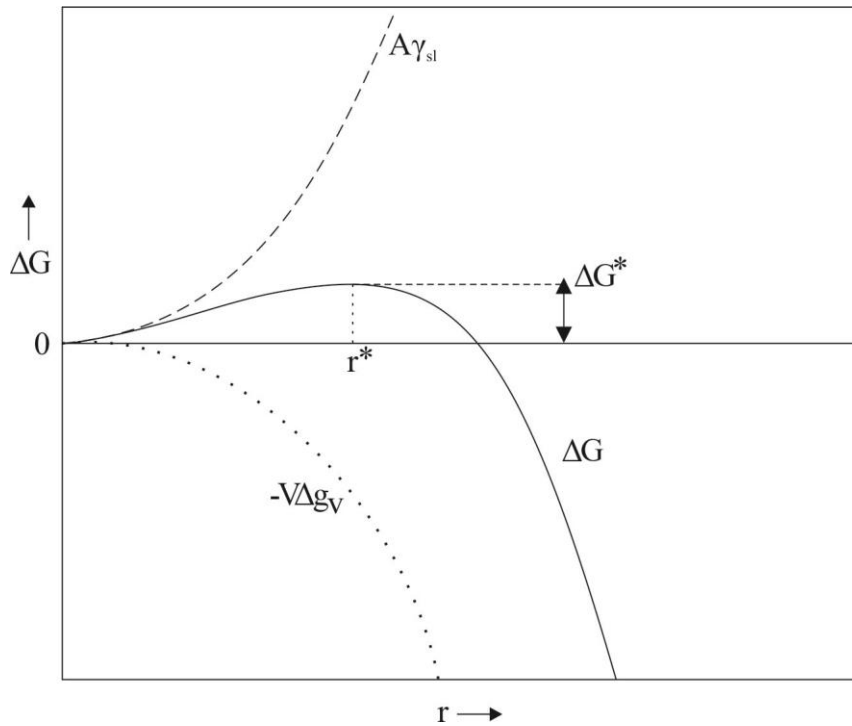
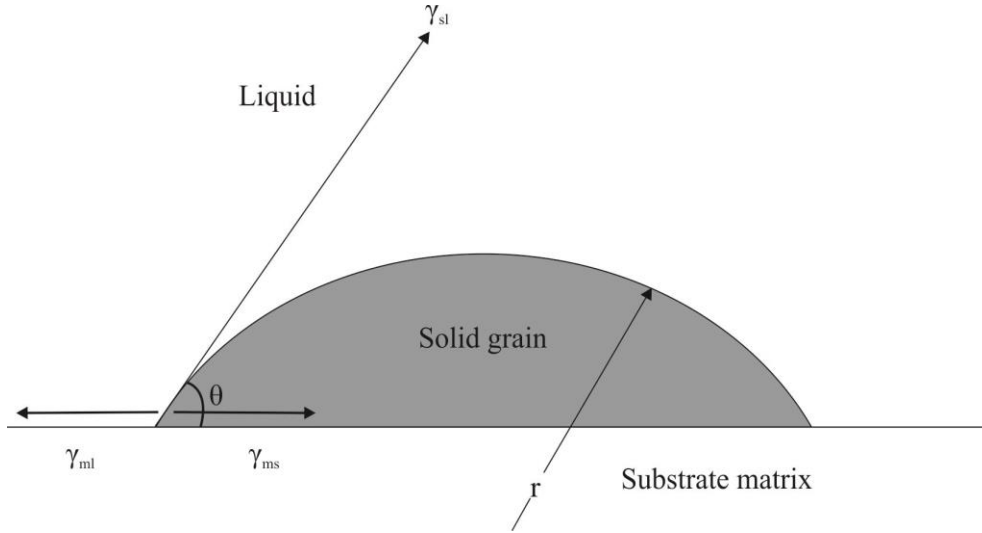


Fig. 2.1 Change in Gibb's free energy for homogeneous nucleation [12].

### 2.1.2 Heterogeneous nucleation

Heterogeneous nucleation occurs due to foreign particles which reduced critical free energy so that stable nuclei may form at lower energy or the nucleation may take place at certain points (Fig.2.2). Heterogeneous nucleation requires less energy as compared to the homogeneous nucleation. Hence, heterogeneous nucleation occurs more rapidly than homogeneous nucleation [13]. In heterogeneous nucleation the foreign particles works as nucleus if wet by the liquid, it should make low contact angle and liquid should have some structural affinity with solid [14]. If foreign particle is wetted by both solid and liquid, then force equilibrium can be given as

$$\gamma_{ms} = \gamma_{ml} - \gamma_{sl} \cos\theta \quad (2.4)$$



**Fig. 2.2 Heterogeneous nucleation of spherical cap on a flat mold wall [7].**

Now from Eq. (2.4)

$$\cos \theta = \frac{\gamma_{ml} - \gamma_{ms}}{\gamma_{sl}} \quad (2.5)$$

Gibb's free energy for heterogeneous nucleation can be given regarding wetting angle  $\theta$  and cap radius  $r$  as;

$$\Delta G_{\text{hetro}} = \left( -\frac{4}{3} \pi r^3 \Delta G_v + 4\pi r^2 \gamma_{sl} \right) G(\theta) \quad (2.6)$$

$$\Delta G_{\text{hetro}} = \Delta G_{\text{homo}} G(\theta) \quad (2.7)$$

$$G(\theta) = \left( \frac{2 - 3\cos\theta + \cos^3\theta}{4} \right) \quad (2.8)$$

Now by differentiating Eq. (2.6) it can be shown that

$$r^* = -\frac{2\gamma_{sl}}{\Delta G_v} \quad (2.9)$$

$$\Delta G^* = \left( \frac{16}{3} \frac{\pi \gamma_{sl}^3}{(\Delta G_v)^2} \right) G(\theta) \quad (2.10)$$

So from above equations, it is cleared that critical energy or free energy barrier for heterogeneous nucleation ( $\Delta G_c$ ) is less when compared to the energy barrier of homogeneous nucleation ( $\Delta G_c$ ) by factor  $G(\theta)$  and is shown in Fig.2.3.

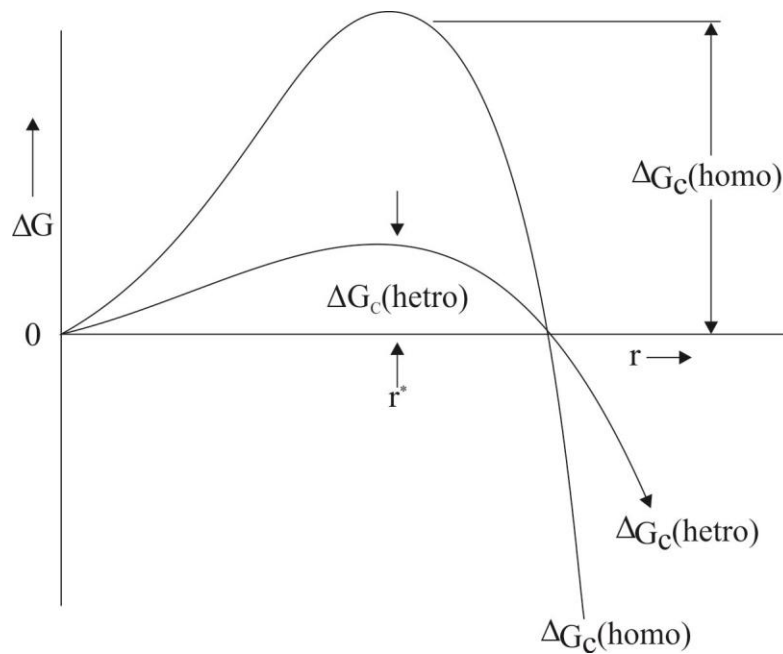
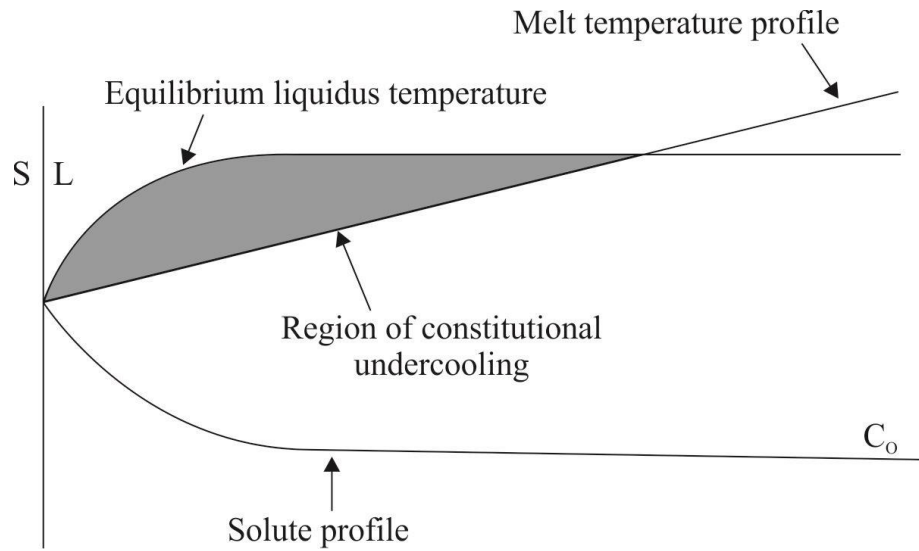


Fig. 2.3 Free energy curve for homogeneous and heterogeneous nucleation [12].

### 2.1.3 Solidification of alloy

#### Constitutional supercooling

In pure metals, solidification occurs at fixed temperature. However nucleation starts only after a certain supercooling through recalescence. For pure metal, the temperature of the liquid attains the equilibrium freezing temperature only at the interface. In such a situation, the solid surface grows with a planer interface. The situation is different for an alloy. The temperature profile for an alloy is shown in Fig 2.4. From Fig. 2.4 it is cleared that the melt temperature is less than the equilibrium temperature for considerable distance. Thus there is a net build up of solute elements at the interface during solidification which establishes a solute concentration gradient. As the supercooling increase, the transition from planer to dendritic is observed. Such supercooling results when solid freezes with a composition difference from that of liquid from which it forms or due to segregation of alloying element ahead of the solid-liquid interface, this is called constitutional supercooling [14].



**Fig. 2.4 Constitutional undercooling on solidification [14].**

**(a) Equilibrium solidification**

Considering the solidification of an alloy A having concentration  $C_0$  in the binary phase diagram of A with an element B as shown in Fig. 2.5. It is assumed that solidus and liquidus follow straight lines and the partition coefficient  $k$  is given as

$$k = \frac{C_s}{C_L} \quad (2.11)$$

Where  $C_s$  and  $C_L$  = concentrations of solute in solid and liquid respectively.

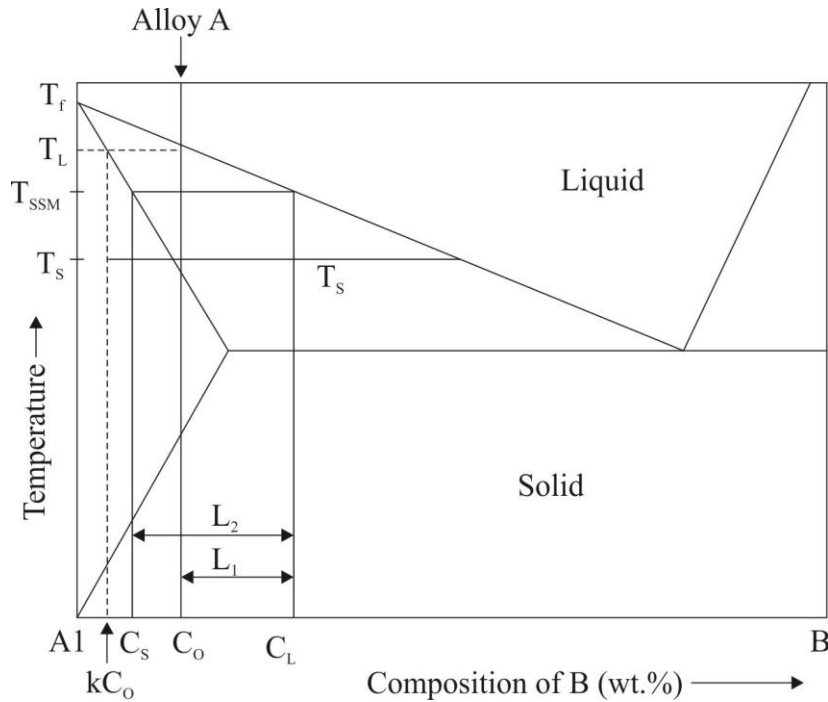


**Fig. 2.5 Phase diagram of Al with an element B [15].**

Equilibrium solidification assumes that complete mixing of the components occurs in both liquid and solid at any temperature between the liquidus temperature and room temperature. In this case the solid would be a homogeneous alloy with the same composition  $C_o$  [15]. The calculation of the fraction solid for a temperature in the interval between liquidus and eutectic temperature is given. When a certain volume fraction of solid, ( $f_s$ ) is formed, a certain volume fraction of liquid, ( $f_L$ ) is remain since,

$$f_s + f_L = 1 \quad (2.12)$$

Now from the law of the conservation of mass;

(Solute in solid) + (Solute in liquid) = (total solute)

$$C_s f_s + C_L f_L = C_o \quad (2.13)$$

Where  $C_s$  and  $C_L$  = concentrations of solute in solid and liquid respectively. Now from Eq. 2.12 and 2.13

$$C_s f_s + C_L (1 - f_s) = C_o$$



$$f_s = \left( \frac{C_L - C_o}{C_L - C_S} \right) \quad (2.14)$$

In equilibrium solidification, solid and liquid are homogeneous to each other since composition followed, the solidus and the liquidus line (Fig. 2.6).

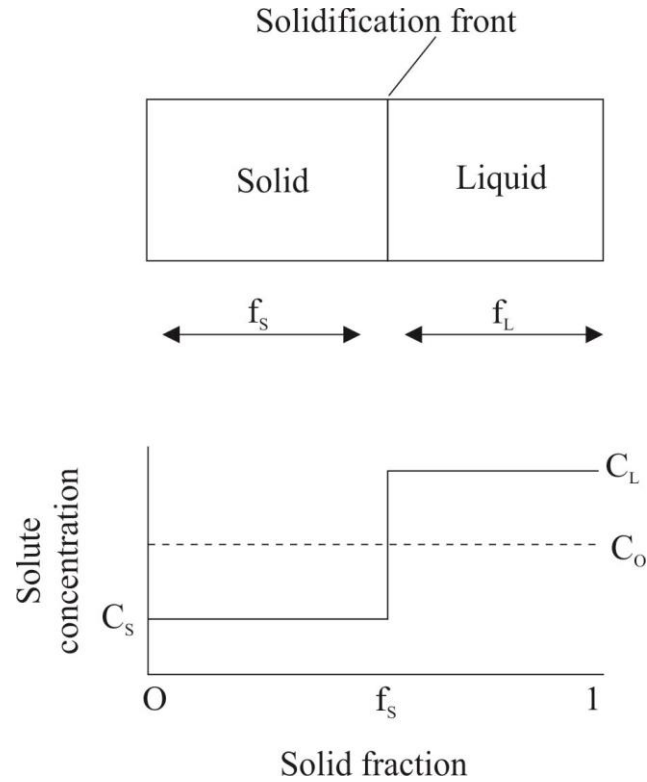


**Fig. 2.6 Solidification under equilibrium conditions [11].**

At a point, the relative amount of solid and liquid at temperature T can be given by lever rule [11].

If,

$$L_1 = C_L - C_o$$

and  $L_2 = C_L - C_S$

Therefore, Eq. (2.14) can be written as

$$f_s = \left( \frac{C_L - C_o}{C_L - C_S} \right) = \frac{L_1}{L_2}$$

This is Equilibrium Lever Rule.

So by using the Eq. 2.12 and 2.13 and equilibrium lever rule the final semi-solid temperature can be given as

$$T_{SSM} = \frac{T_f[f_s(1-k)] - T_L}{f_s(1-k) - 1} \quad (2.15)$$

Where,  $T_f$  = melting point of Al,

$T_L$  = temperature at composition  $C_o$ ,

$T_{SSM}$  = semi-solid temperature

Eq. (2.15) provides a semi-solid temperature for given solid fraction.

**(b) Non-equilibrium solidification (Scheil's equation)**

Scheil's equation assumes that the solute is always completely mixed in the liquid, and distributed uniformly with concentration  $C_L$ . It also considers that in the solid no diffusion takes place. Based on Fig. 2.7 let us assume that initially a uniform solute concentration in the liquid with a value of  $= C_o$  exists. The first solid formed has a composition  $kC_o$ , where  $k$  is the partition coefficient.

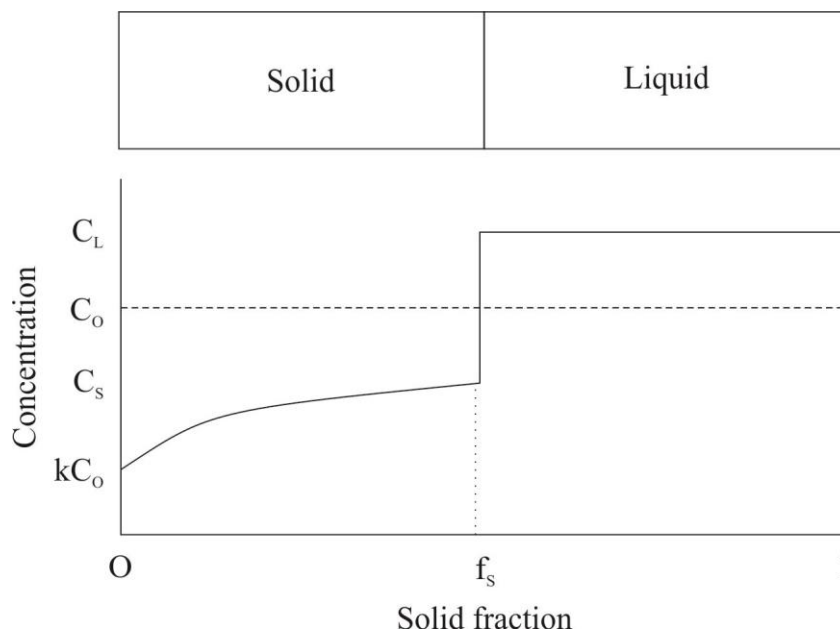


**Fig. 2.7 Solidification in non-equilibrium conditions [16].**

If  $k$  is high ( $\approx 1$ ), then it designates that solute is equally distributed between solid and liquid, so segregation tendency is small. However, if  $k$  becomes small ( $< 1$ ) then the liquid exhibits a higher solute concentration than the solid and a tendency of segregation exists [16]. When solid formed, the excess of solute is rejected ahead of the advancing front.

Figure 2.8 reveals that concentration of solute in solid and liquid are  $C_S$  and  $C_L$  respectively. Here it is assumed that some variations (by small amount  $df_s$ ) in solid-liquid interface takes place since the concentration of  $dC_L$  increased due to the rejected solute concentration in the liquid.

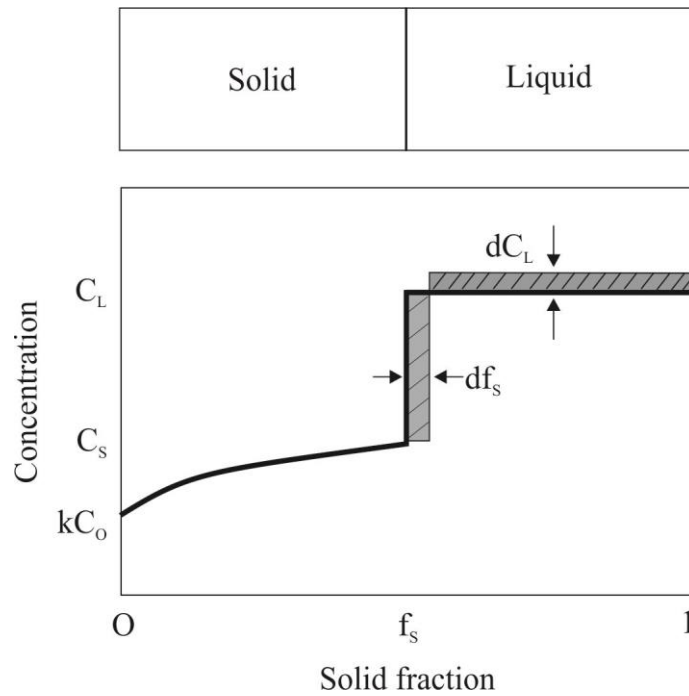


**Fig. 2.8 Advancing solid-liquid interface having initial solute concentrations  $C_S$  and  $C_L$  in solid and liquid respectively [16].**

Assuming that total amount of solute in the system is conserved, the shaded areas are set equal.

$$(C_L - C_S)df_s = dC_L \cdot f_L \quad (2.16)$$

$f_s$  = volume fraction of solid

$f_L$  = volume fraction of liquid

Since

$$f_s + f_L = 1 \quad (2.17)$$

Rewriting Eq. (2.16) using Eq. 2.11 and 2.17

$$(C_L - kC_L)df_s = dC_L \cdot (1 - f_s)$$

$$\frac{df_s}{(1 - f_s)} = \frac{dC_L}{C_L(1 - k)}$$

Now integrating Eq. (2.16) using boundary conditions of Scheil's equation

$$C_L=C_o, \quad f_s=0$$

$$\int_0^{f_s} \frac{df}{(1-f_s)} = \frac{1}{(1-k)} \int_{C_o}^{C_L} \frac{dC_L}{C_L} \quad (2.18)$$

Now by solving above Eq. (2.18) we have

$$C_L = C_o(1 - f_s)^{(k-1)} \quad (2.19)$$

From Eq. (2.11) and (2.19) it follows

$$C_s = kC_o(1 - f_s)^{(k-1)} \quad (2.20)$$

These equations are known as non-equilibrium lever rule or the Scheil's equations [11].

Since solidus and liquidus are assumed to be straight lines, one can write this equation also in terms of temperature leading after some simple algebraic manipulations to

$$\left( \frac{T_{SSM} - T_f}{T_L - T_f} \right) = (1 - f_s)^{(k-1)}$$

or, 
$$T_{SSM} = (T_L - T_f)(1 - f_s)^{(k-1)} + T_f$$

or, 
$$T_{SSM} = T_f - (T_f - T_L)(1 - f_s)^{(k-1)} \quad (2.21)$$

Here,  $T_f$  = melting point of component A,

$T_L$  = temperature at composition  $C_o$  i.e. where first solid forms,

$T_{SSM}$  = semi-solid temperature.

Eq. (2.21) gives the semi-solid temperature of the slurry for a given solid fraction.

## 2.2 Grain Refinement

In grain refinement, the grain size of  $\alpha$ -Al phase is reduced to improve the feed ability, shrinkage porosity and to improve the mechanical properties of Al alloy, since for instance yield strength and ultimate tensile strength increase with a reduction of grain size. The grain refinement is carried out with the addition of a grain refiner in the melt, which provides more number of nucleating sites and thus forms grains of smaller size [17].

Many investigators observed grain refinement due to nucleating particles and solute concentration itself. Nucleating particles provide heterogeneous nucleating sites at which the primary phase nucleates at low undercoolings, whereas solute gives the constitutional undercooling which restricts grain growth and thus reduces grain size [18-19].

Al-Ti-B master alloys are frequently employed for grain refinement in Al alloys. However, other inoculants e.g. Al-Ti-C and Al-B are also used as grain refiners [20]. Although Al-Si alloys typically have excellent castability, weldability and mechanical properties. Hypoeutectic Al-Si alloys can exhibit a coarse columnar dendritic  $\alpha$ -Al network during solidification, if the cooling rate or rate of heat extraction is small, like in sand casting. The reliability of cast hypoeutectic Al-Si alloys further depends upon the solid fraction, size and morphology of primary  $\alpha$ -Al. Hence,  $\alpha$ -Al phase exhibits immense importance. The castability of hypo-eutectic Al-Si alloys can be enhanced by reducing the grain size of  $\alpha$ -Al [21]. So grain refinement is of prior importance [22].

According to Kissling and Wallace [23], grain refinement in Al alloys can be carried out by three methods;

- (a) Rapid cooling,
- (b) The agitation of the melt/semi-solid metal processing,
- (c) The addition of grain refiners to the melt.

In the first method, a fine grain structure is produced owing to high cooling rate, which can be achieved in permanent metallic molds or thin parts. In the second method, grain refinement is observed due to mechanical or electromagnetic stirring, which leads to suppression of dendrites and convert them into a fine-grained equiaxed structure. In industries, the grain refinement is carried out by the addition of grain refiners in the melt, which nucleates new crystals during solidification process [21].

### 2.2.1 Theories of grain refinement

So far the available theories can be grouped into two paradigms;

(a) Nucleant particle theory

(b) Solute theory

The former provides more nucleating sites while later restrict the growth of these nucleated particles i.e. the complementary role of nucleant particles and solute pile up eventually refining the grain size.

#### (a) Nucleant particle theory

Various theories such as phase diagram theory, hyper nucleation theory, peritectic theory and duplex theory were given to explain the mechanism of grain refinement and among them, duplex nucleation theory is widely accepted [24]. This theory was provided by Mohanty et al. [25] and further by Schumacher et al. [26]. Mohanty et al. [25] added  $TiB_2$  particles to a melt (A356 alloy) with different percentages of titanium. Based on this theory when Ti was not present in melt then  $TiB_2$  particles were shifted to the inter-dendritic region and grain refinement was not observed. However, when Ti was in hyper-peritectic concentration, then  $TiB_2$  was at the center of Al grains with a layer of  $TiAl_3$  on  $TiB_2$  particles and  $\alpha$ -Al on  $TiAl_3$ . A layer of  $TiAl_3$  between  $TiB_2$  and  $\alpha$ -Al was also observed when Ti was in hypo-eutectic concentrations. There was no strong evidence for this theory and got much criticism. Schumacher et al. [26] recommended that  $TiAl_3$  mainly occur due to adsorption effect at the interface of boride and aluminide. However, the reason for the stability of  $TiAl_3$  layer was not cleared. So the stability of  $TiAl_3$  layer can be explained based on the impurity of Tantalum, which shifts the peritectic concentration due to peritectic reaction with Al and provides stability to  $TiAl_3$ .

Classical nucleation theory was applied to calculate the rate of formation of spherical-cap nuclei on refiner particles. The nucleation rate on a particle is dependent on the undercooling, the contact angle  $\theta$ , and the particle size. Classical nucleation theory in calculations used only single values of  $\theta$  and particle size [27].

Greer and co-workers [27] gave the well accepted free growth model to explain the nucleation on inoculants particles. According to the model, the effectiveness of a refiner may be determined by

a free-growth condition in which the undercooling for free growth is inversely proportional to the particle diameter. As the melt is cooled below the liquidus temperature, free growth of crystals occurs first on the largest inoculant particles, and then on more, smaller particles. All the growing crystals release latent heat that is distributed uniformly through the melt, slowing the rate of cooling, and eventually causing the temperature to rise (recalescence). After the temperature has started to rise, there is no further initiation of free growth. Thus recalescence limits the refinement of grain size.

**(b) Solute theory**

This theory was recommended by Johnsson et al. [28] and explained the influence of grain refinement by nucleants and segregating solutes. The segregation was calculated by a so-called growth restriction factor (GRF). Actually, solutes control the grain growth once the  $\alpha$ -Al phase has nucleated at a nucleating particle. It was proposed that the nucleant particles and the segregation of solute elements (e.g. Ti, Si) exhibit a significant role in grain refinement [29]. The GRF (Q) can be given as;

$$Q = m (k-1) \tag{2.23}$$

Where, m = gradient of the liquidus, and k= partition coefficient of solute at the solid-liquid interface.

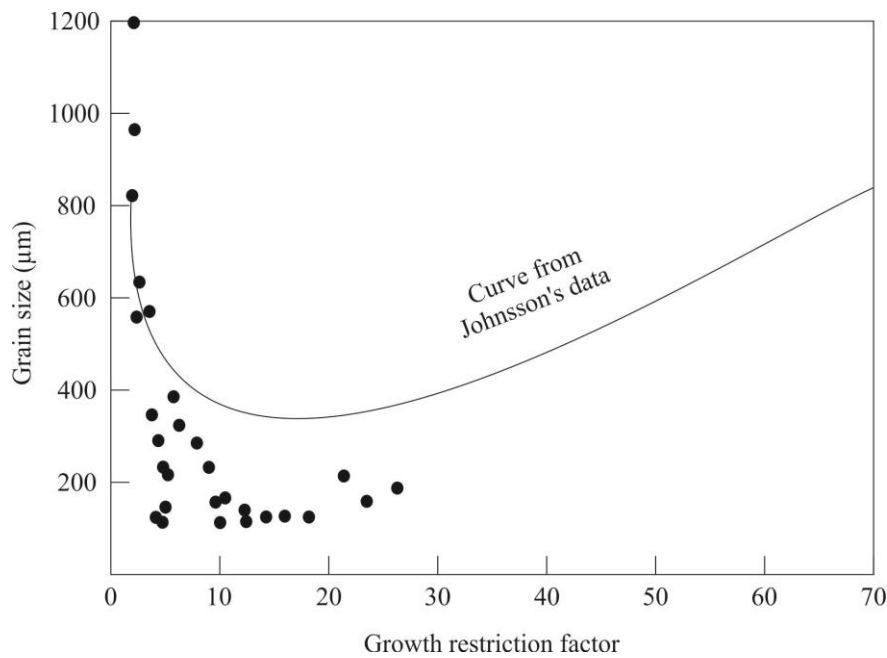


**Fig. 2.9 Variation of grain size with growth restriction factor [11].**

The quantity  $m(k-1)$  shows the effect of solute on the grain size. For titanium,  $m(k-1) = 245.6$ , while, for silicon, it is only 5.9; hence, small amounts of titanium produce a large decrease in grain size, while much higher amounts of silicon are required for a similar effect. It should be noted that solute titanium significantly reduces the grain size even when no  $TiB_2$  nucleants are added [19].

## **2.3 Semi-Solid Metal Processing**

Al-Si alloys have good castability and good corrosion resistance. A356 (Al-7Si-0.3Mg) exhibits good mechanical properties and widely used in the field of automotive and aerospace industries. In conventional cast A356 alloy, the primary  $\alpha$ -Al phase exhibits dendritic morphology. Dendritic morphology leads to poor castability and shrinkage porosity. However, finer dendritic structure with lower value of SDAS gives rise to improved mechanical properties. The same can be achieved by rapid cooling, mechanical vibrations and by adding grain refiner to the melt. There is another method called semi-solid metal (SSM) forming where globular  $\alpha$ -Al phase forms instead of dendrites. This also gives rise to improved mechanical properties [30].

In SSM processing the SSM slurry is formed in the mushy zone i.e. partial solid and partial liquid behavior. SSM processing has been widely used for 45 years, but initially, it was employed by the Spencer [30] in 1971 during his doctorate work at MIT under Prof. Flemings. The Sn-15Pb alloy was used to evaluate the behavior of the alloy using the Couette viscometer. It was observed that Sn-15Pb alloy exhibited thixotropic behavior [31]. SSM slurry can be prepared by two methods known as Thixocasting and Rheocasting.

### **2.3.1 Thixocasting**

Thixocasting produces a non-dendritic structure in two steps and involves an intermediate solidification step; the semi-solid billet is cut to specified length, re-heated into the mushy zone to get the desired solid fraction [30].



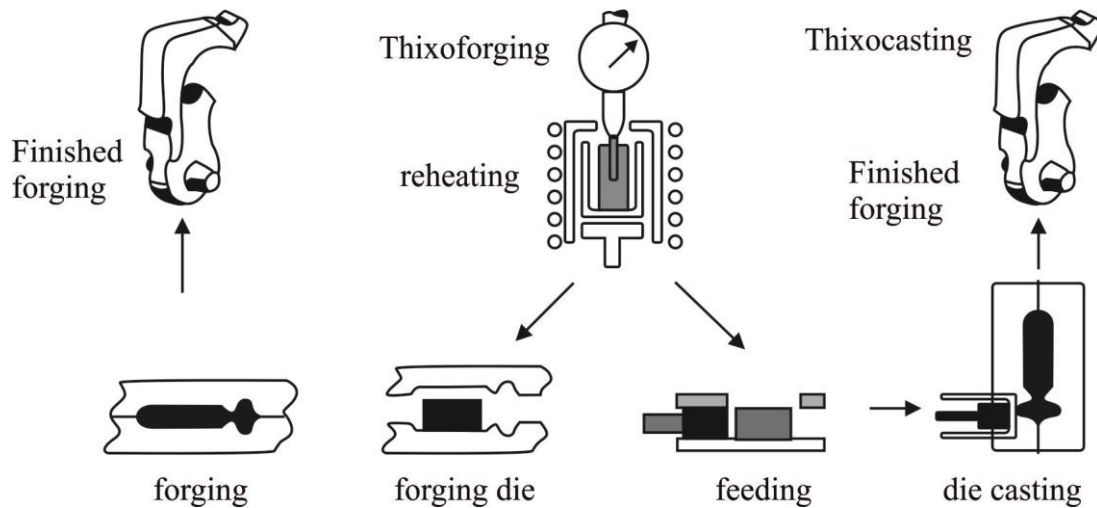


**Fig 2.10 Schematic illustration of thixocasting process [30].**

### **2.3.2 Rheocasting**

In rheocasting, the alloy is held in the semi-solid region based on its phase diagram. In the rheocasting process, the alloy is cooled in a semi-solid state and transferred in the mold without any intermediate solidification step. Finally, it is cooled to obtain the desired solid fraction and properties [30-32].

The major rheocasting processes are (i) direct slurry forming (DSF), (ii) new-rheocasting (NRC), (iv) semi-solid rheocasting (SSR), (v) continuous rheocasting (CRP) and (vi) rheometal process [33-38].

#### **(i) Direct slurry formation (DSF)**

This process involves the bulk production and holding of semi-solid slurry in a charging vessel. The process can be divided in three steps: formation of semi-solid metal, maintenance of the slurry suspension and transport the semi-solid mixture to the die casting machine. Die casting operations have furnaces for melting ingot, and the molten alloy is transported to holding furnaces at the casting press.

In this process, heat is removed through the walls of the furnace, dendrites tend to form at the outer walls of the furnace and grow inward as solidification progress. Mechanically scraping the walls of the furnace at regular intervals during solidification breaks growing dendrites from the wall and moves them into the bulk of the crucible. With sufficient stirring action, these dendritic

structures are moved through the melt and coarsened into rounded structures by the flow of liquid around them.

To overcome vertical segregation, an impellor with inclined rotating blades forces the flow of material upward in the melt. The final mixing system in the furnace consisted of an anchor shaped rotor with vertical shearing rods located close to the furnace walls for the scraping of solidifying material, and an auger located within the rotor shape to promote vertical homogeneity [Fig. 2.11].

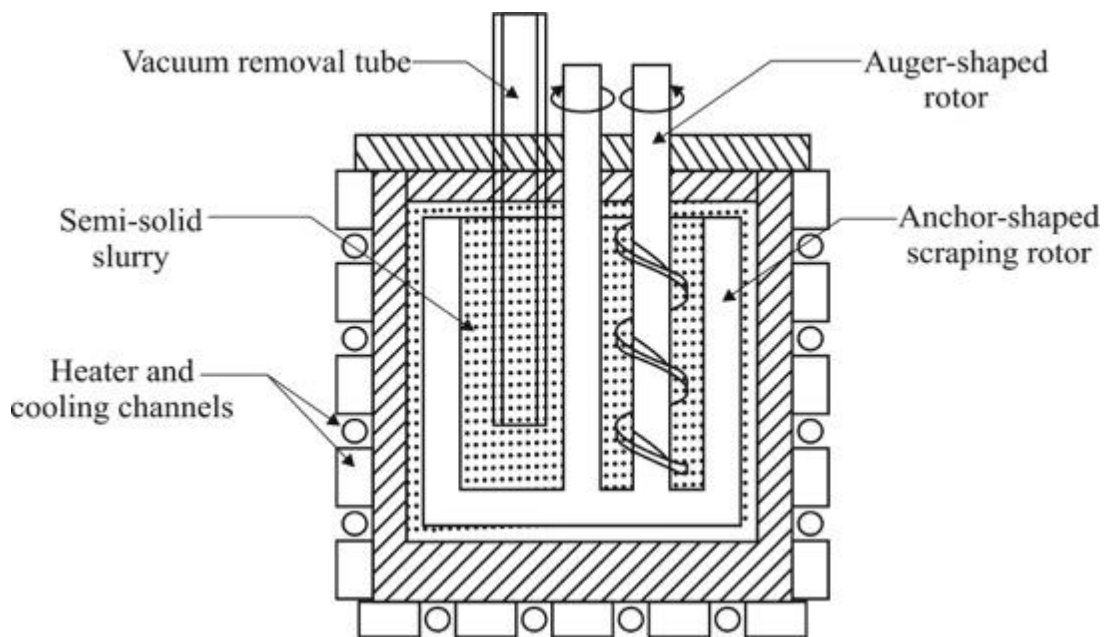


**Fig. 2.11 Schematic diagram for direct slurry formation process [33].**

### **(ii) New rheocasting process (NRC)**

In the NRC process a fully liquid melt is taken from the furnace and poured into steel cups. By cooling of the melt into the semi-solid region a globular microstructure is attained. In the final position of the cup the temperature is equalized over the cross-section of the cup. The semi-solid melt is then poured into the inclined sleeve of a squeeze casting machine, the sleeve docks to the die, and the slug is cast into shape. Figure 2.12 shows the schematic illustration of new rheocasting (NRC) process [32]. Until now, the NRC process has been used for cast and wrought Al alloys and Mg alloys.

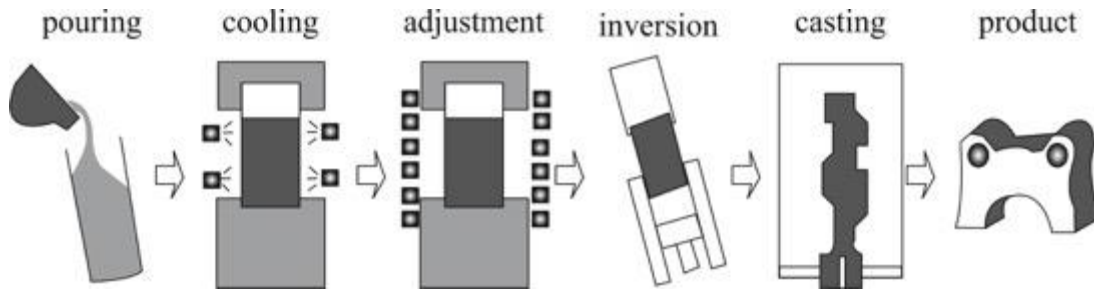


Fig. 2.12 Schematic illustration of new rheocasting (NRC) process [32].

### (iii) Semi-solid rheocasting (SSR)

The semi-solid rheocasting (SSR) process the alloy is being heated upto semi-solid temperature. In this process cold finger is a mean to rapidly decrease the temperature and stir the melt. And then transfer the semi-solid material to a high pressure die casting machine (Fig.2.13) [32].

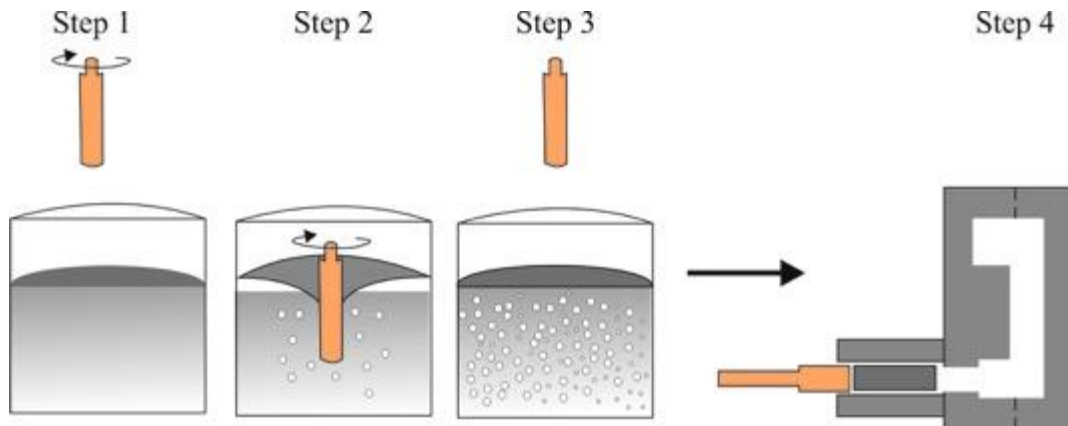
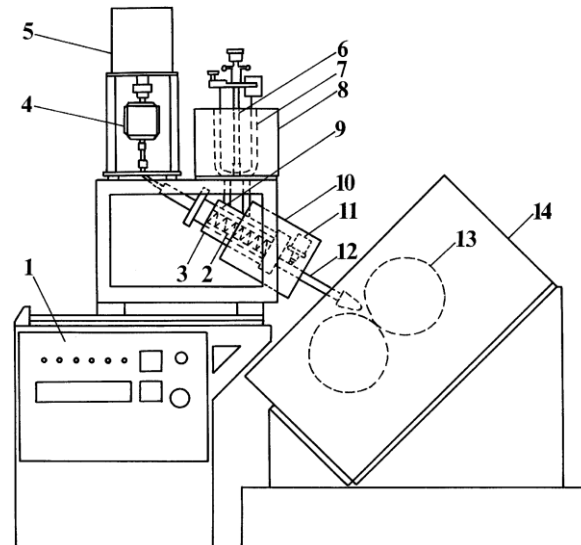


Fig. 2.13 Schematic representation of SSR process [32].

### (iv) Continuous rheocasting process (CRP)

The continuous rheoconversion process (CRP) can be applied to both thixocasting and rheocasting. The process combined two separate techniques, liquid mixing and passive stirring, to achieve globular morphology [34].

In CRP process the melting of the alloy is carried out in an inert gas atmosphere. In this process a stirring apparatus to produce high quality slurry by mechanical stirring and a twin roll rotary caster to produce the alloy sheet with homogeneous microstructure [34].



**Fig. 2.14 Schematic illustration of continuous rheocasting apparatus. 1: Controller, 2: stirrer, 3: isothermal heater, 4: rotation detector, 5: rotation motor, 6: stopper, 7: graphite crucible, 8: melting furnace, 9: graphite mold, 10: additional reheater, 11: stopper, 12: nozzle, 13: twin rollers, and 14: twin roller caster [34].**

#### **(v) Rheometal process**

In this process, the semi-solid slurry is prepared by immersing a specified amount of solid alloy (having the same composition as the melt) in the melt. The solid alloy is known as enthalpy exchange material (EEM) which serves as an internal cooling agent and simultaneously as a stirrer. In this process enthalpy exchange, between a superheated melt and EEM takes place. As the EEM extracts heat from the melt and melts by itself, the slurry is generated having globular morphology. Figure 2.11 shows the schematic representation of the rheometal process.

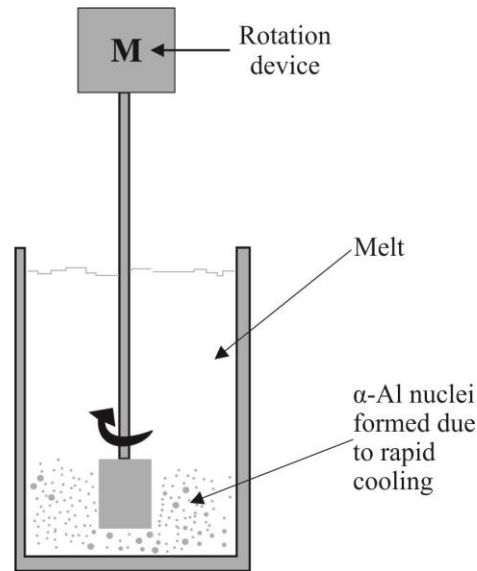


Fig. 2.15 Schematic illustration of rheometal process [35].

The enthalpy exchange in rheometal process can be explained using following equations indicating cooling and partial solidification of superheated melt ( $dQ_{out}$ ) and the heating and partial melting of the EEM ( $dQ_{in}$ )

$$dQ_{in} = m_{eem} \times C_{p\ eem} \times (T_{SSM} - T_{eem}) + \Delta H_{eem} \times (1 - f_s) m_{eem}$$

$$dQ_{out} = m_{melt} \times C_{p\ melt} \times (T_{melt} - T_{SSM}) + \Delta H_{melt} \times f_s \times m_{melt}$$

Where,  $m_{eem}$  = mass of EEM,  $m_{melt}$  = mass of melt,  $C_p$  = specific heat,  $T_{melt}$  = temperature of melt,  $T_{eem}$  = temperature of EEM before mixing,  $\Delta H$  = latent heat,  $f_s$  = final solid fraction and  $T_{SSM}$  = semi-solid temperature of slurry.

$$dQ_{out} = dQ_{in} \quad (2.24)$$

From these equations, the volume or mass ratio between the melt and the EEM can be calculated for the given solid fraction of the semi-solid slurry [35-38].

## 2.4 Rheology

Rheology is science which studies deformation and flow of material simultaneously. The term rheology was provided by scientists Professor Marcus Reiner [39] in 1920's and accepted by the American Society of Rheology in 1929. Initially, the materials like lubricants, plastics, paints and rubber were used to study rheological behavior of materials [39]. In the beginning,

most of the theories were concerned with reversible phenomena, but later it was observed that non-reversible phenomena are also important [40].

Nowadays rheology is expanded and utilized for different purposes. It is used for development and processing of plastics, paint, metals, food, polymers, biological fluids, and suspensions. It is also used in filtration, forming materials, cosmetics, refining in the petroleum industry and coating [41].

### **2.4.1 Fundamentals of rheology**

Fundamentals of rheology are as given below;

#### **(a) The basic law**

Isaac Newton gave the basic law of viscometry to define the flow behavior of an ideal liquid [42-43].

$$\tau = \eta \dot{\gamma} \quad (2.25)$$

Where,  $\tau$  = shear stress,  $\eta$  = dynamic viscosity and  $\dot{\gamma}$  = shear rate

#### **(b) Newtonian fluids**

Fluids which obey the Newton's law (Eq. 2.25), in which shear stress is linear proportional to the shear rate, are called Newtonian fluids. In a plot of shear stress versus shear-rate, the straight line stands for Newtonian fluid whose slope is the dynamic viscosity (Fig. 2.16). Viscosity describes resistance to flow and is defined as internal friction of the fluid. For Newtonian fluids, the viscosity of the fluid is constant regardless of shear rate [44]. Most gases and liquids (water, benzene, and ethyl alcohol) are examples of Newtonian fluids [45-46].

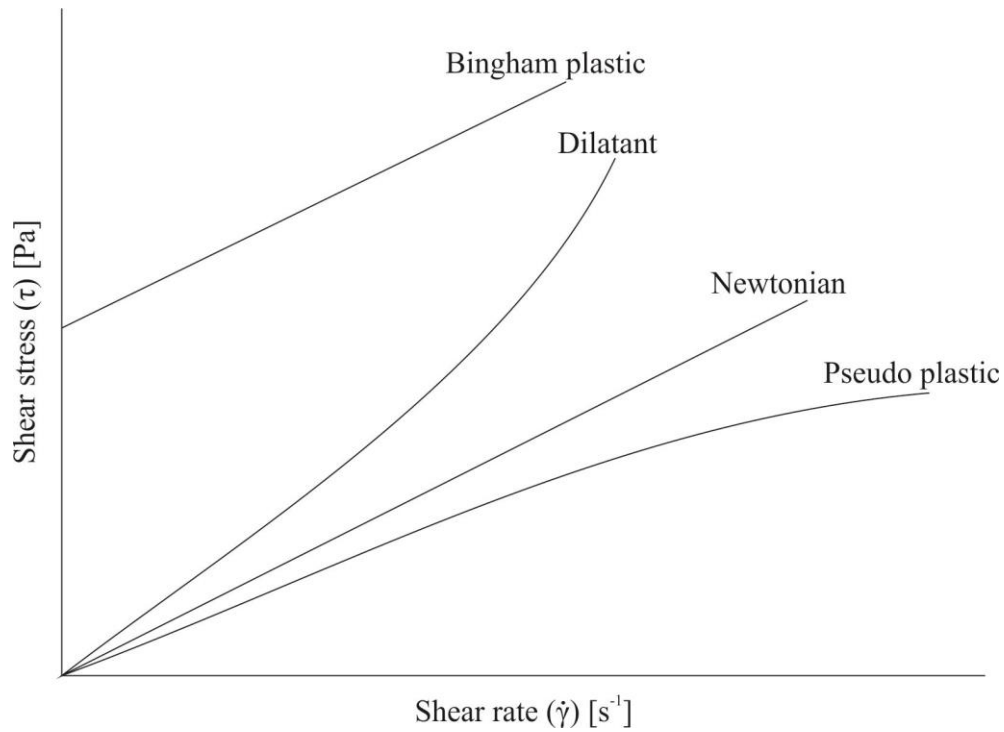


**Fig. 2.16 Different types of fluid behavior [44].**

### (c) Non-Newtonian fluids

The fluids which do not follow Newton's law i.e. for which viscosity is not constant are known as non-Newtonian fluids. For non-Newtonian fluids, the flow curves (Fig. 2.16) are non-linear and can be described for instance as

$$\tau = K\dot{\gamma}^n \quad (2.26)$$

$$\eta = K\dot{\gamma}^{n-1} \quad (2.27)$$

Where, K= proportionality constant and n= power law index.

Newtonian fluids are a unique case of Eq. 2.27 for  $n = 1$ . Hence, n shows the non-Newtonian behavior (fluid behavior). A pseudo-plastic behavior of the material is evident for  $n < 1$ . Examples of such type of fluids are gelatin, blood, milk. While shear thickening behavior takes place for  $n > 1$ . Examples are sugar in water, an aqueous suspension of rice starch, etc [47].

The fluids for which, the viscosity increases with the shear rate are known as dilatants fluids or shear thickening [48]. For dilatants fluids, the power law exponent is greater than one. Since the viscosity of pseudo-plastic and dilatants fluid is not constant, the viscosity of such fluids is referred as apparent viscosity. In time-dependent fluids, the viscosity varies with time and also referred as apparent viscosity. The behavior of these fluids is shown in Fig.2.16 [49-51].

One of the most significant parameters which show the rheological behavior of the material is viscosity ( $\eta$ ). It has a vital role similar to the fluidity in liquid metals and modules of strength for solids [52]. Based on review articles, viscometry is a suitable route to study the rheological behavior of material [53]. The viscosity of SSM slurry depends upon number of parameters and can be given by

$$\eta = f(\dot{\gamma}, t, T_{SSM}, \dot{T}, f_s) \quad (2.28)$$

Where;  $\eta$ = Viscosity,  $\dot{\gamma}$  = shear rate,  $t$  = holding time,  $T_{SSM}$  = semi-solid temperature,  $\dot{T}$ = cooling rate,  $f_s$ = solid fraction [54].

The existence of yield stress can be considered when the SSM slurry treated as Bingham fluid. Herschel–Bulkley model describes the deformation characteristics of such fluids and can be given as

$$\tau = \tau_0 + K\dot{\gamma}^n \quad (2.29)$$

Where  $\tau_0$ = yield stress. Eq. (2.27) is used when the material does not have plastic behavior. If the material exhibits plastic behavior, then a term of yield stress can be added and is given by Eq. (2.29). Eq. 2.29 gives the steady state flow curves which used to fit theoretical and experimental value of yield stress. However, different investigators [55-57] reported substantial differences between theoretical and experimental values. For example, the shear rate exponent  $n = 0.83$  for a semi-solid slurry of Sn–15Pb with a solid fraction of 0.45 [55], while  $n = 1.29$  by Modigell and Koke [56]. To scrutinize the dominance of the proposed model, the model was compared with the Herschel–Bulkley model (Fig. 2.17).



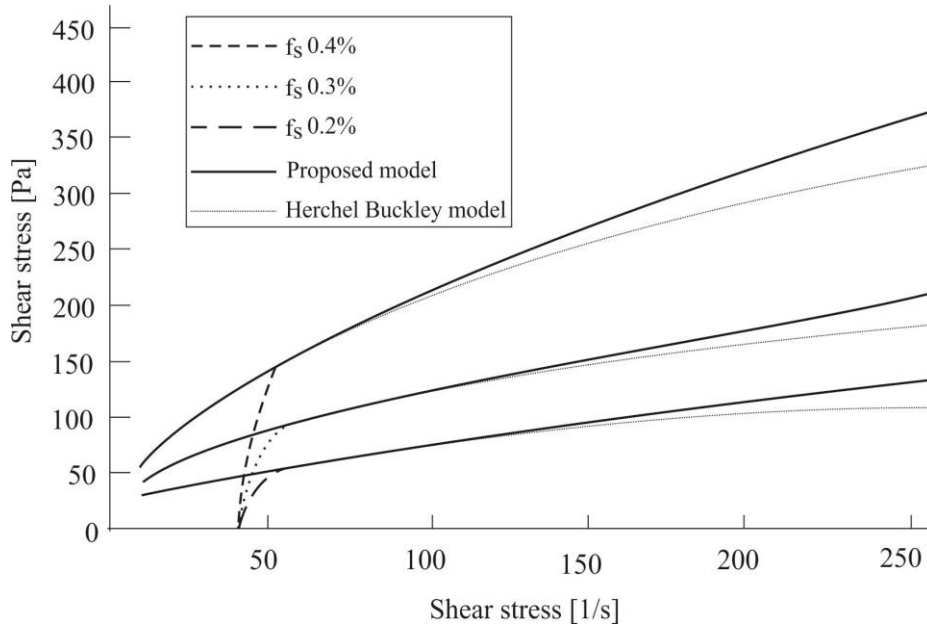


**Fig. 2.17 Comparison between proposed model and the conventional Herschel-Bulkley model [57].**

Figure 2.17 shows that the Herschel–Bulkley model predict the flow behavior for the low value of shear rate. At a higher value of shear rate, the model showed deviations between theoretical and experimental values. Therefore, the model parameters should calibrate for the higher value of shear rates, in which lower value of shear rates modeled with error [57].

## 2.4.2 Principle of rheology

The rheological behavior can be analyzed when the flow behavior of slurry under deformation is carried out [55-58]. Flemings et al. [58] investigated the rheological behavior of an Al-4.5% Cu alloy. The observations showed that at solid fraction lower than 0.5, there was a small variation in apparent viscosity, but when the solid fraction was higher than 0.5, there was a continuous variation in apparent viscosity even with slight variations in solid fraction. Simlandi et al. [59] studied the rheological behavior of Al-7Si (A356) alloy via a concentric cylinder viscometer. The phenomenon of agglomeration and de-agglomeration of particles in the semi-solid slurry was given using the structural parameter ( $\lambda$ ).

## 2.4.3 Effective parameters of rheology

### (a) Solid fraction

Solid fraction is an important parameter which affects the viscosity of primary  $\alpha$ -Al phase, e.g. dendrites in the case of Al–Si alloys [62]. Generally for a given shear rate, as solid fraction increases, the apparent viscosity increases, slowly for a low solid fraction and rapidly for a high solid fraction. Figure 2.18 demonstrates the continuous cooling experiments for Sn–15Pb alloy [63].

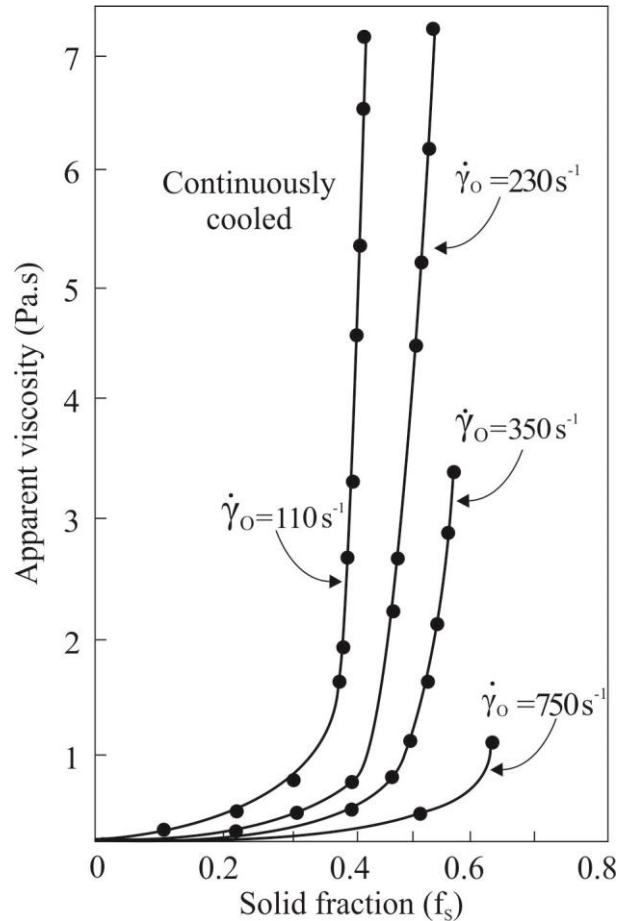


**Fig. 2.18** Apparent viscosity vs solid fraction of Sn-15Pb alloy sheared continuously and cooled at 0.33K  $\text{min}^{-1}$  at different shear rates  $\dot{\gamma}_0$  [63].

Figure 2.18 shows that when solid fraction was less than 0.6, the viscosity of slurry increases slowly and exhibits pseudo-plastic behavior (steady state behavior), but for a solid fraction higher than 0.6, the apparent viscosity rapidly increases and illustrates thixotropy behavior (transient state behavior).

Barman et al. [64] gave a numerical model to observe the transport phenomena during solidification of Al-alloy with linear electromagnetic stirring using a set of governing equations of mass, momentum, and energy. The numerical study engages the prediction of temperature,

velocity, and solid fraction distribution in the mould. The numerical predictions of temperature variations were in good agreement with experiments. The experimental study showed the consequence of solid fraction on the apparent viscosity of an A356 alloy. Their observation revealed that as solid fraction increased upto 0.55, the viscosity of the slurry increased at a very low rate. Afterwards, it increases rapidly for higher values of solid fraction. Figure 2.19 shows the comparison, between experimental values and theoretical values obtained with the model given by Barman. Both show a similar trend. The main significance of the model is that the formation of microstructures can be explained well with the help of simulated flow fields.

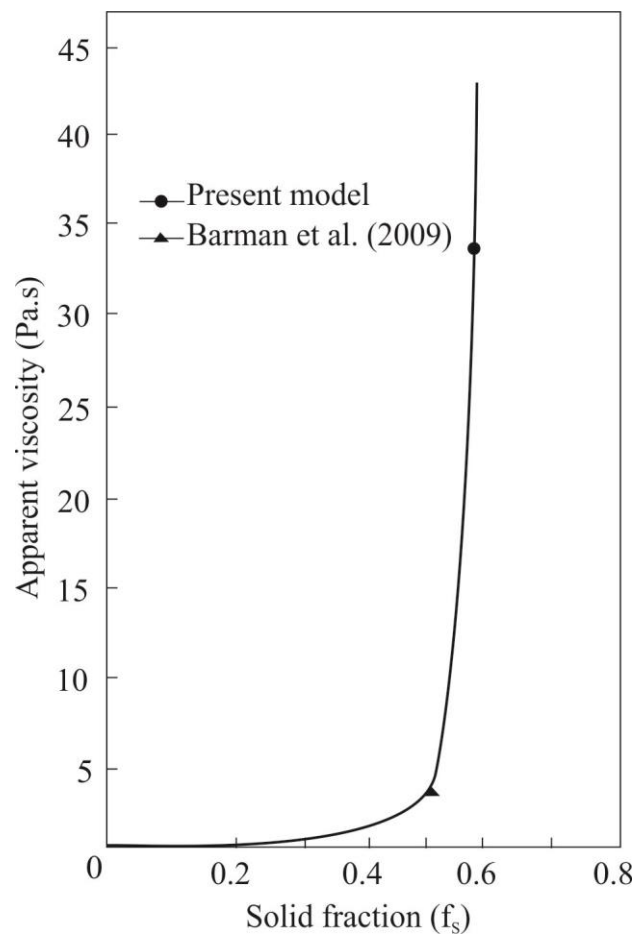


**Fig. 2.19** Variation of apparent viscosity with solid fraction (at shear rate  $266 \text{ sec}^{-1}$ ) [64].

Granath et al. [65] studied the RSF process for the A356 alloy with different values of solid fraction (mass of EEM) from 4 to 7wt.%. Figure 2.20 confirms that average grain size of  $\alpha$ -Al phase decreased as solid fraction increased.

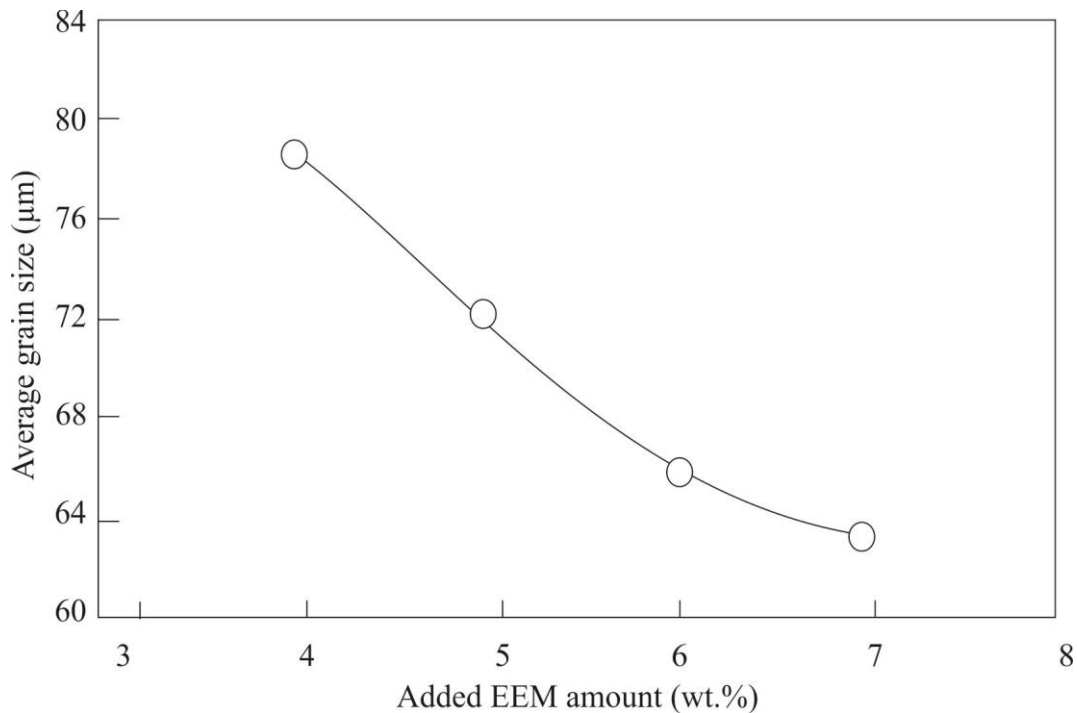


**Fig. 2.20 Effect of EEM amount on the average grain size [65].**

**(b) Shear rate**

Isothermal steady state experiments leads to a more specific rheological characterization. The steady state defines as a condition in which the viscosity of semi-solid slurry for a given solid fraction and shear rate does not vary with extended shearing time. Hence, for a given alloy, the steady-state viscosity is a function of solid fraction and shear rate and not time. The semi-solid slurry with less than 0.6 solid fraction exhibits two different rheological behavior; (a) pseudo-plastic and (b) thixotropic. Pseudo-plastic revealed the steady-state behavior, while thixotropy illustrates time-dependent transient state behavior [66]. Joly and Mehrabian [63] showed that Sn–15Pb alloy exhibited shear thinning (or pseudo-plastic) behavior. This shear thinning was also confirmed by Turng and Wang [67]. In an SSM slurry for a given solid fraction, the steady-state viscosity decreased as shear rate increased and approached an asymptotic value when shear rate become infinite (Fig. 2.21). Such pseudo-plastic behavior was also observed by Das et al. [68].

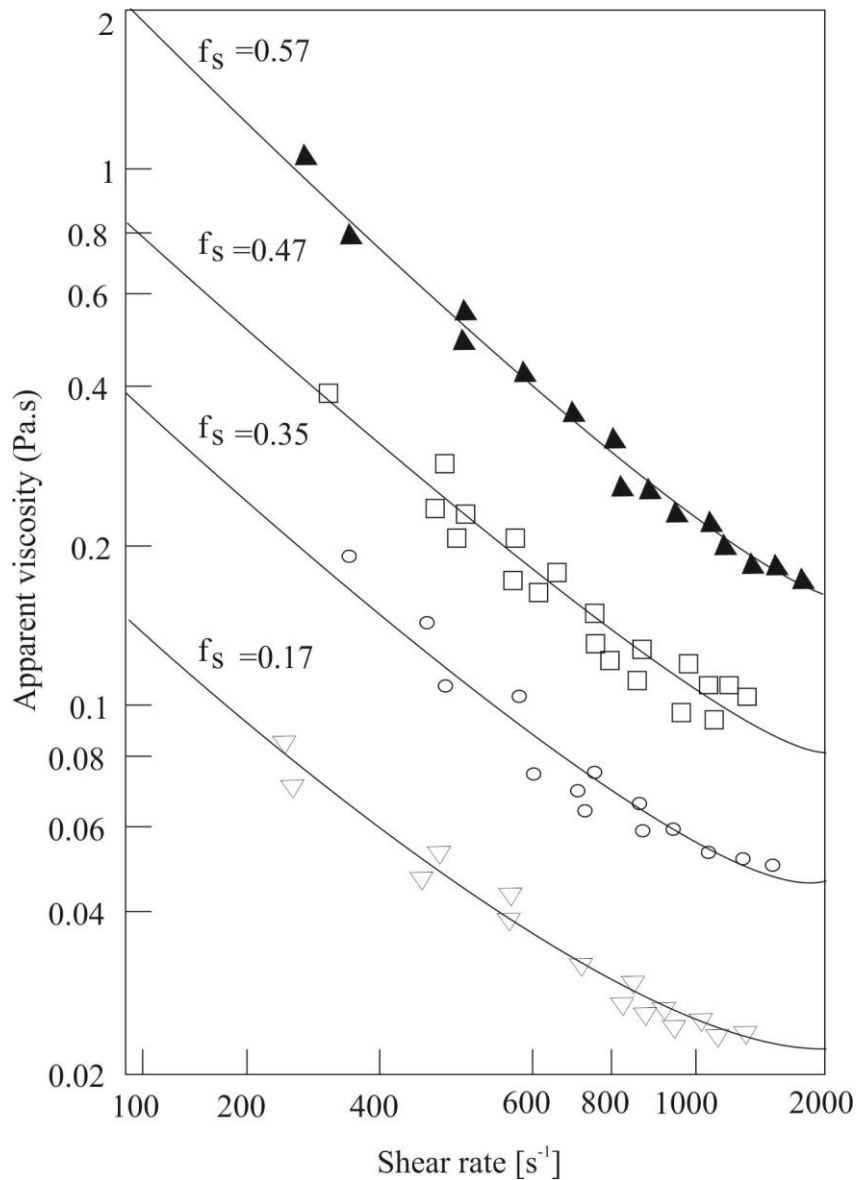


**Fig. 2.21 Steady state apparent viscosity vs. shear rate in Sn-15Pb alloy for various solid fractions  $f_s$  [63].**

Shear rate affects the average grain size of primary  $\alpha$ -Al phase. As shear rate increased, the average grain size decreased i.e. shear rate showed grain refinement. Granath et al. [65] demonstrated the effect of rotation speed on the morphology of A356 alloy produced by RSF method. The rotation speed was varied from 600 to 1800 rpm for solid fraction about 5wt.% and temperature of the slurry was about 627 °C. Das et al. [68] showed that as the shear rate increased the viscosity of the slurry decreased. The decreasing trend in viscosity is attributed to the breakage of structural linkage i.e. de-agglomeration of primary  $\alpha$ -Al particles within semi-solid slurry. Hence, the steady state viscosity for any shear rate depends on the agglomeration and de-agglomeration between particles. Figure 2.22 shows that average grain size of  $\alpha$ -Al phase decreased as rotation

speed increases and attains the average grain size about 69  $\mu\text{m}$  for a rotation speed of 1800 rpm (Fig. 2.23).

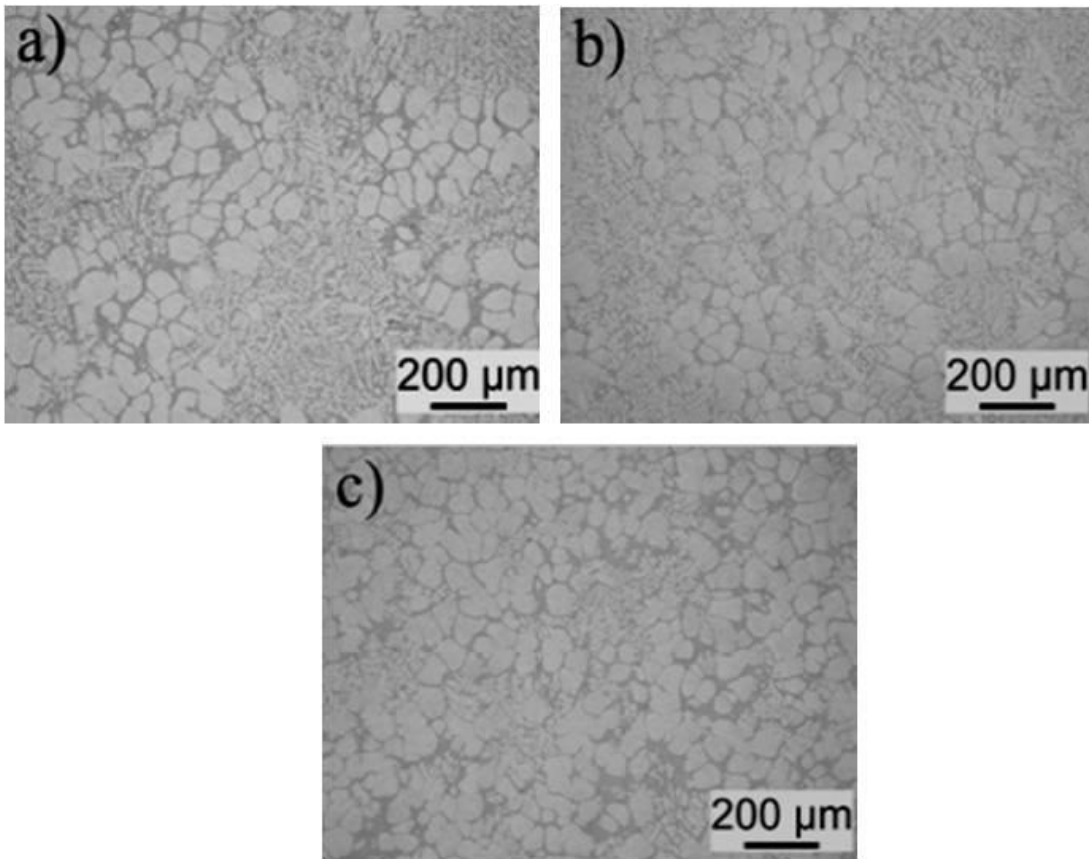


**Fig. 2.22** Slurry microstructures produced at (a) 600 (b) 1200 and (c) 1800 rpm for solid fraction 5% and temperature 627°C [65].

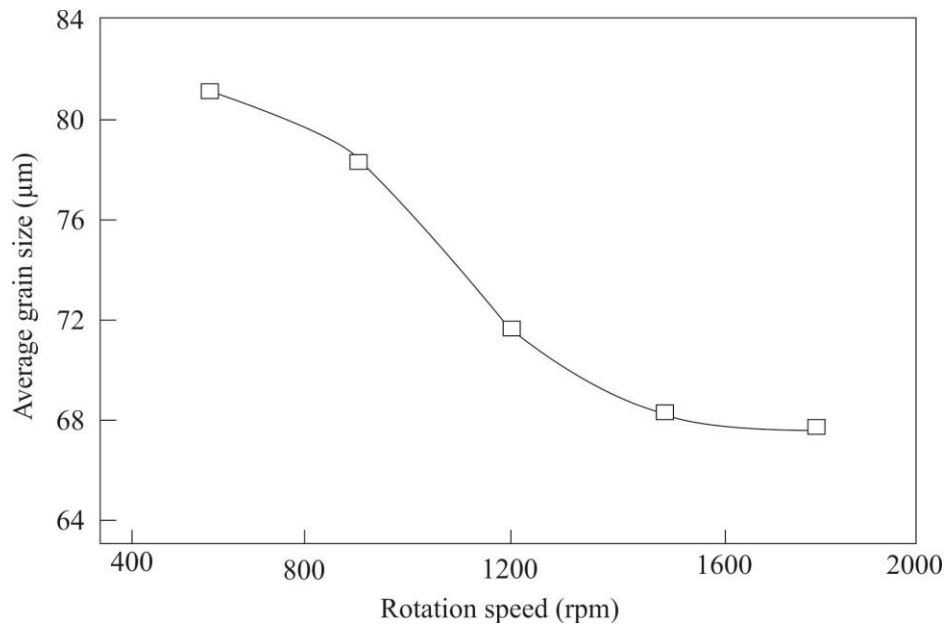


**Fig. 2.23** Effect of rotation speed on the average grain size [65].

### (c) Temperature

Temperature plays a significant role in semi-solid metal processing. As temperature increases, the viscosity of fluid decreases. Temperature provides the activation energy to the molecules of the fluid that caused motion in them. Motion occurred when the fluid molecules slide on each other and the ease of flow depend upon the molecular chain and the force of attraction between the molecules.

Zheng et al. [69] showed the effect of temperature with electromagnetic stirring on semi-solid ZL 101 (Al-7.46 Si-0.49 Mg) alloy.

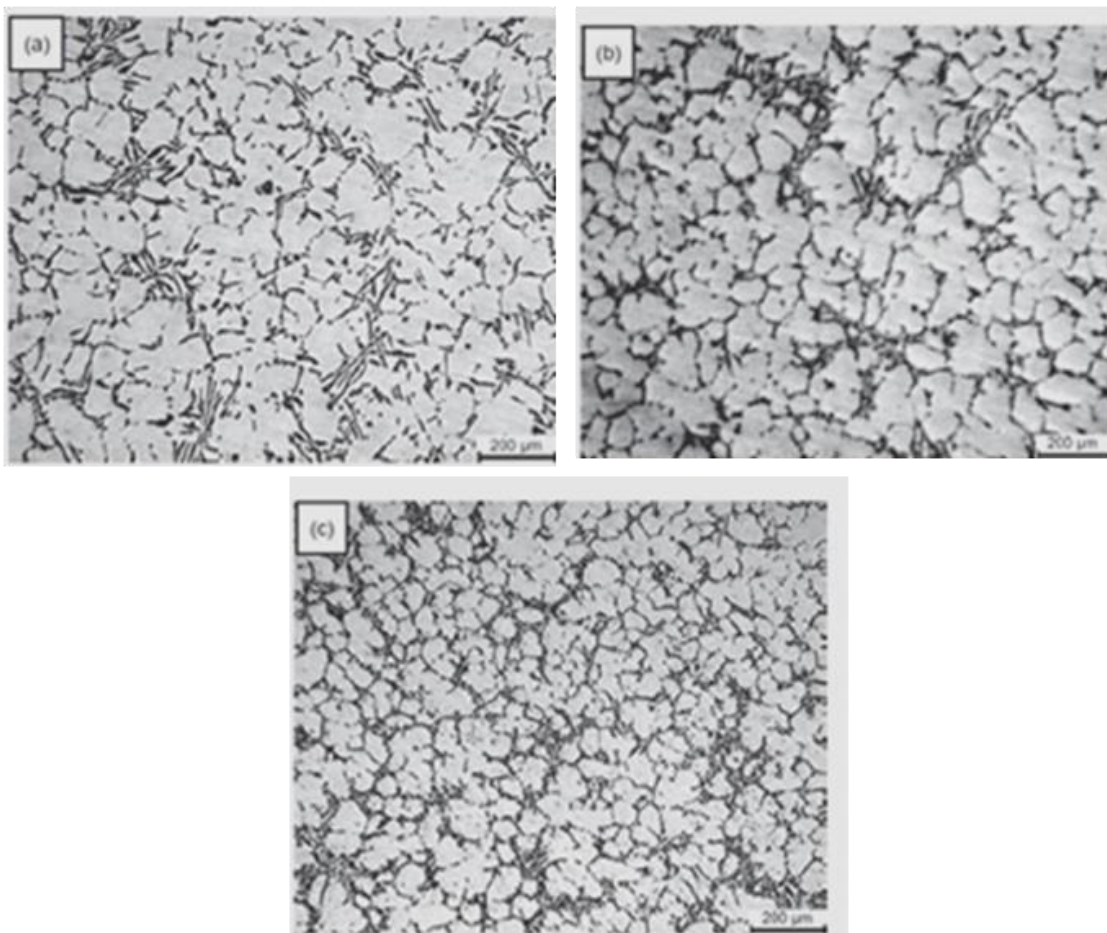


**Fig. 2.24 Morphology of primary phase in ZL101 alloy with stirring at various pouring temperature (a) 650 (b) 630, and (c) 615° C [69].**

Figure 2.24(a) illustrates that  $\alpha$ -Al phase has priority to rosette-like, few globular-like and particle-like morphology with coarse grain size. In Fig. 2.24(b), the majority of  $\alpha$ -Al comprises globular-like and particle-like morphology and few have rosette-like morphology with reduced grain size. Furthermore, in Fig. 2.24(c)  $\alpha$ -Al phase have globular-like and particle-like

morphology and more refined grains when compared with the grain in Fig. 2.24 (a-b) [69]. Hence, observation showed that as pouring temperature decreased the grain size of  $\alpha$ -Al phase also decreased.

Birrol [70] studied the morphology of Al-7Si-0.6Mg in a semi-solid state. Figure 2.25 shows that conventionally cast hypo-eutectic Al alloy illustrated dendritic morphology.

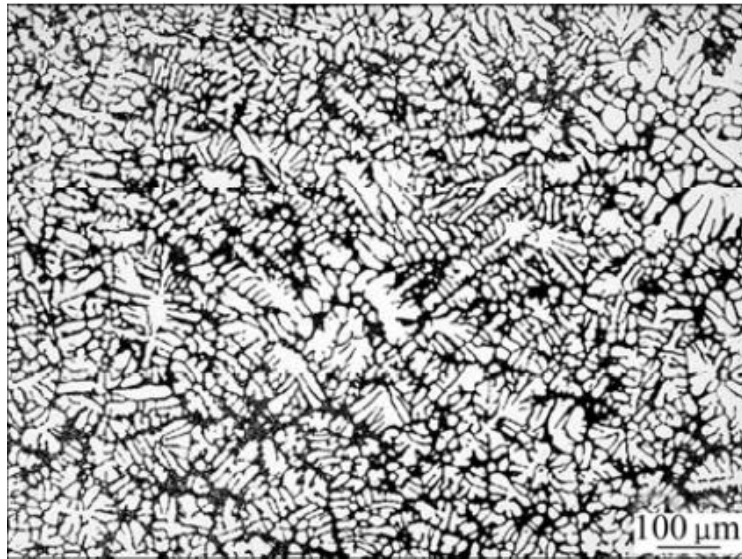


**Fig. 2.25 Microstructure of water quenched melt [70].**

Figure 2.26(a-d) demonstrates that when alloy was stirred in the semi-solid region, the dendritic network changed its morphology into globular morphology (Fig. 2.26). The semi-solid temperatures were estimated from the cooling curve between solid fraction and temperature.



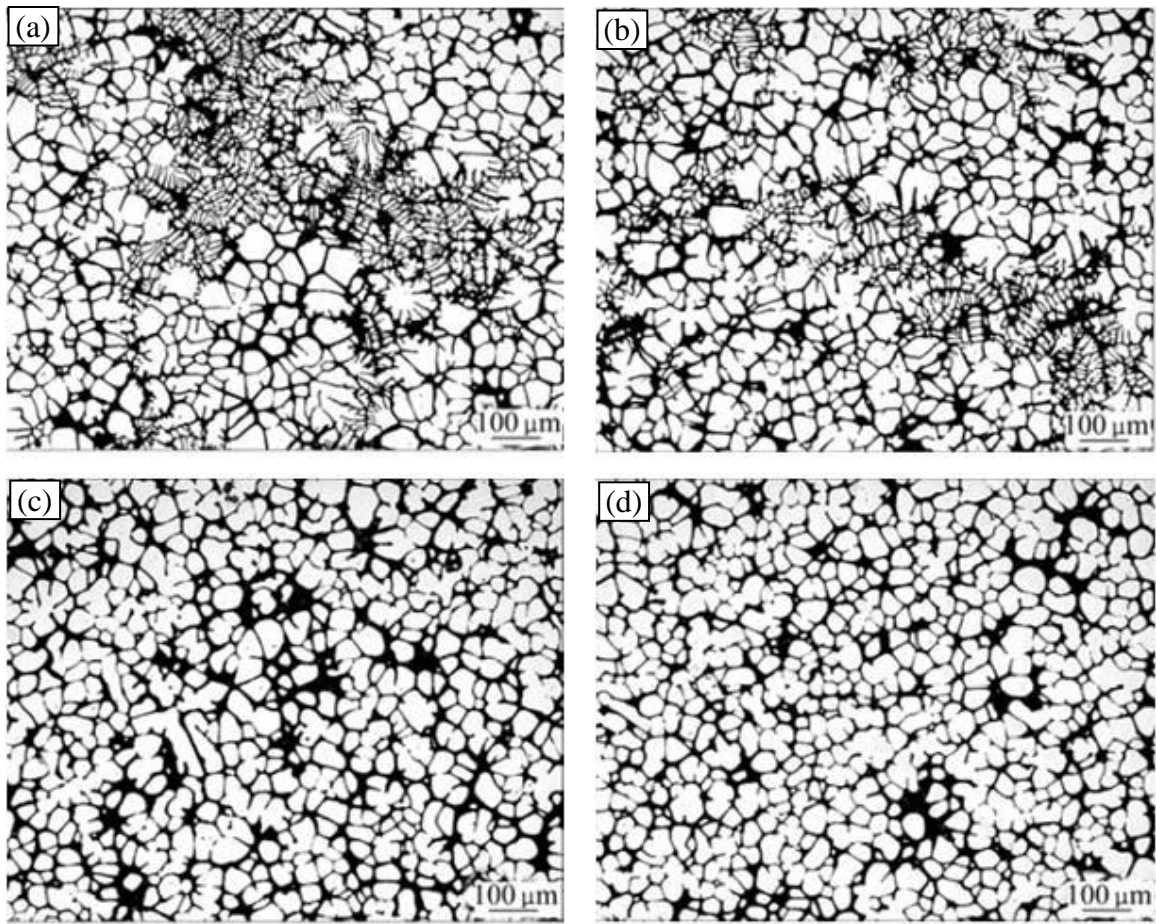


Fig. 2.26 Microstructures of Al-7Si-0.6Mg with stirring at temperature (a) 605 (b) 600 (c) 590, and (d) 580 °C [70].

The result shows that as semi-solid temperature decreased the average grain size of  $\alpha$ -Al phase decreased. The average grain size of  $\alpha$ -Al globules was about 30 $\mu$ m for the temperature of 580°C.

## 2.5 Coarsening Mechanism of SSM Process

In coarsening mechanism particles grow by reducing solid-liquid interfacial free energy. In general coarsening is a power law which relates average grain size with time as follows;

$$D^n - D_0^n = Kt \quad (2.30)$$

Where;  $D_0$  = initial average grain size,  $D$  = mean grain size after time  $t$ ,  $n$  = coarsening index and  $K$  = coarsening rate constant. Two different mechanisms known as Ostwald ripening and coalescence were given to explain the coarsening mechanism [33]. Ostwald ripening occurs by mass transport between differently curved interfaces of for instance particles. Coalescence also always

occurs, but the coalescence rate depends on the square of the particle number and thus increases with fraction solid drastically.

Many investigators [71-74] studied the coarsening kinetics in different alloys. Birol [71] studied the coarsening kinetics of A357 alloy cast through cooling slope process (Fig.2.27).

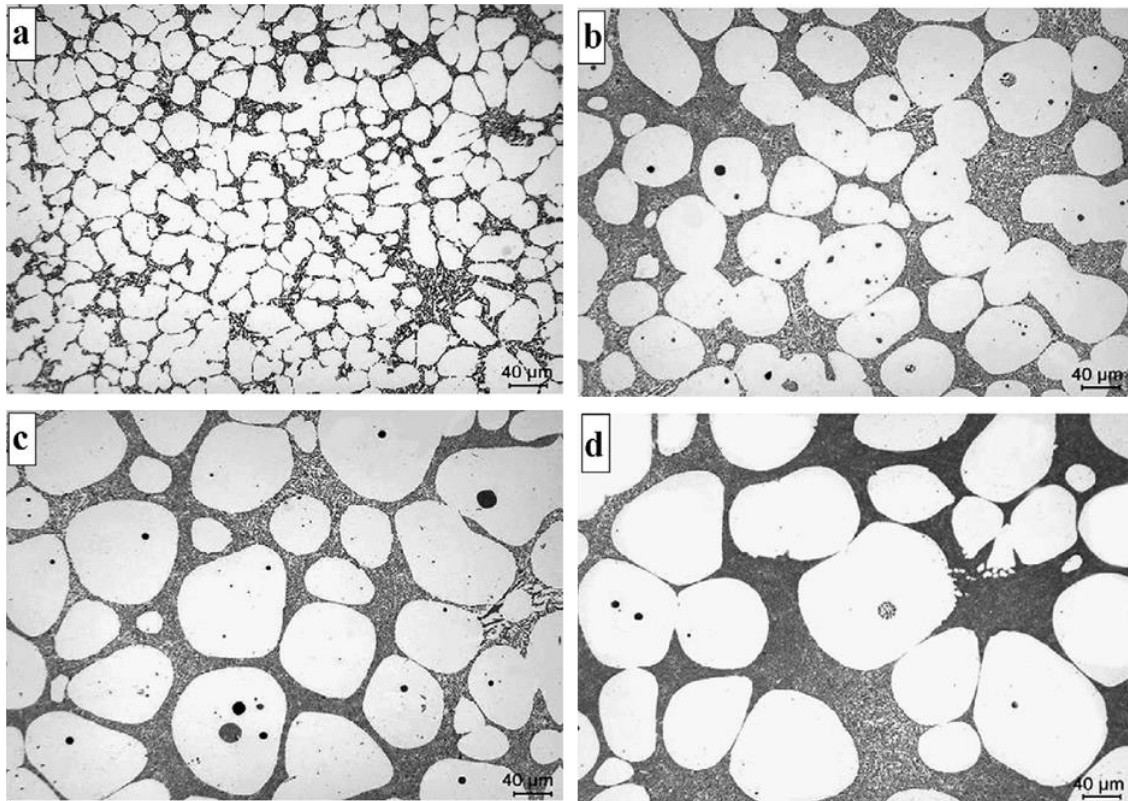


**Fig.2.27** Microstructures of ingots (a) cast over the cooling plate with a pouring temperature of 640 °C and a cooling length of 400mm and after isothermal holding at 580 °C for (b) 5, (c) 15 and (d) 30 min [71].

In cooling slope process the cooling plate was adjusted at 60° with respect to the horizontal plane and was cooled by water circulation underneath. The surface of the plate was coated with boron nitride to avoid adherence of molten alloy. A pre-heated sprue was used so that molten metal could fill mold easily. The melt, which has become semi-solid by the end of the cooling plate filled the mold and solidified very fast. The transformation, from dendritic primary  $\alpha$ -Al phase in the conventionally cast A357 alloy to non-dendritic one in ingots cast over a cooling plate from pouring temperatures between 620 and 640 °C and with cooling lengths between 200 and 400 mm takes place [71].

The results showed that coalescence occurred in the early periods of isothermal holding, while Ostwald ripening acquired as the key mechanism in the later stages.

Lashkari et al. [72] studied the coarsening of the semi-solid A356 alloy at pouring temperature of 595 °C. Their observation showed that as holding time increased, the coarsening of primary  $\alpha$ -Al phase occurred because of two mechanisms, Ostwald ripening and coalescence.

Haghdadi et al. [73] observed the coarsening rate constant of A356 alloy cast through the accumulative back extrusion (ABE) process.

In the ABE process the work piece is put into the die cavity. Any cycle of ABE process consists of a back extrusion followed back-pressing. These operations are being performed through twin punch setup, the punches slide on each other. In the first step the work piece is extruded into the gap between the inner punch and the die through the back extrusion process. In the second step the back extruded material is pressed back by the outer punch. As the outer punch is pushed down the inner punch is loosely lift up by undergoing material flow. The latter causes the deformation without any reduction in cross section of work piece. Moreover, the inner punch is remained inside the cup during the second step thereby preventing the cup to collapse [73].

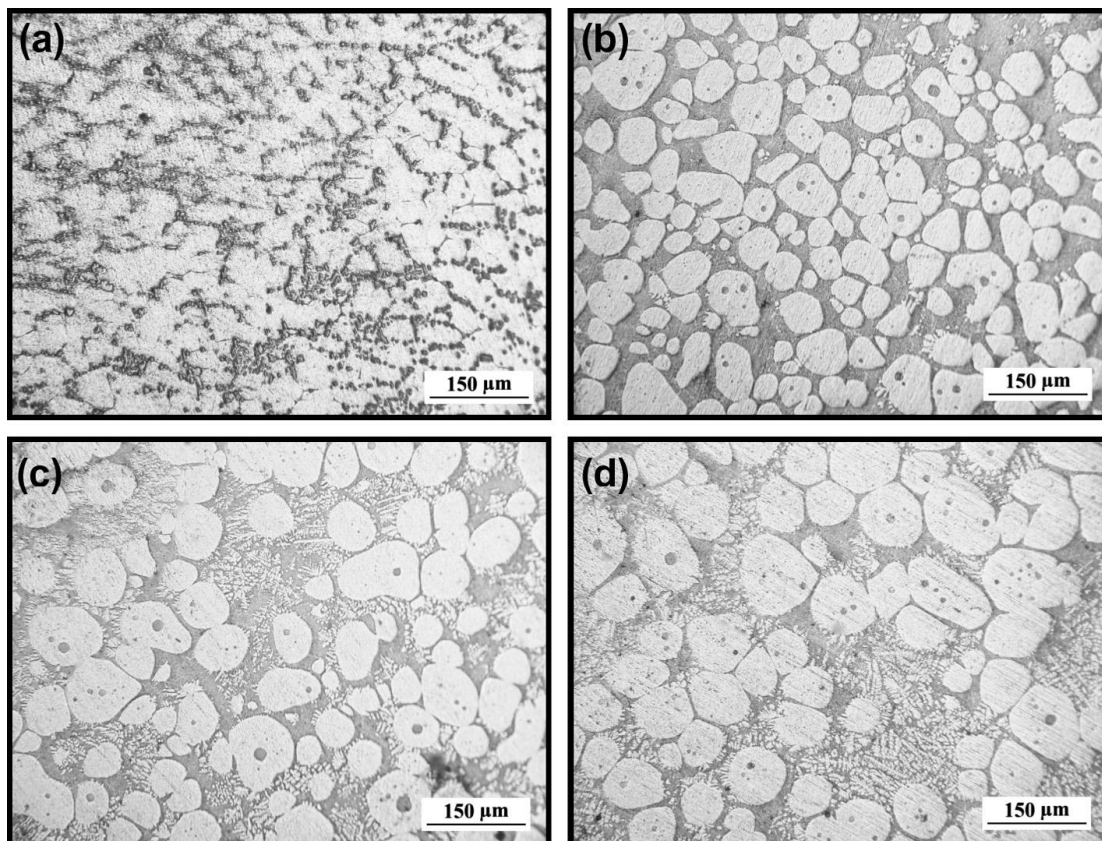
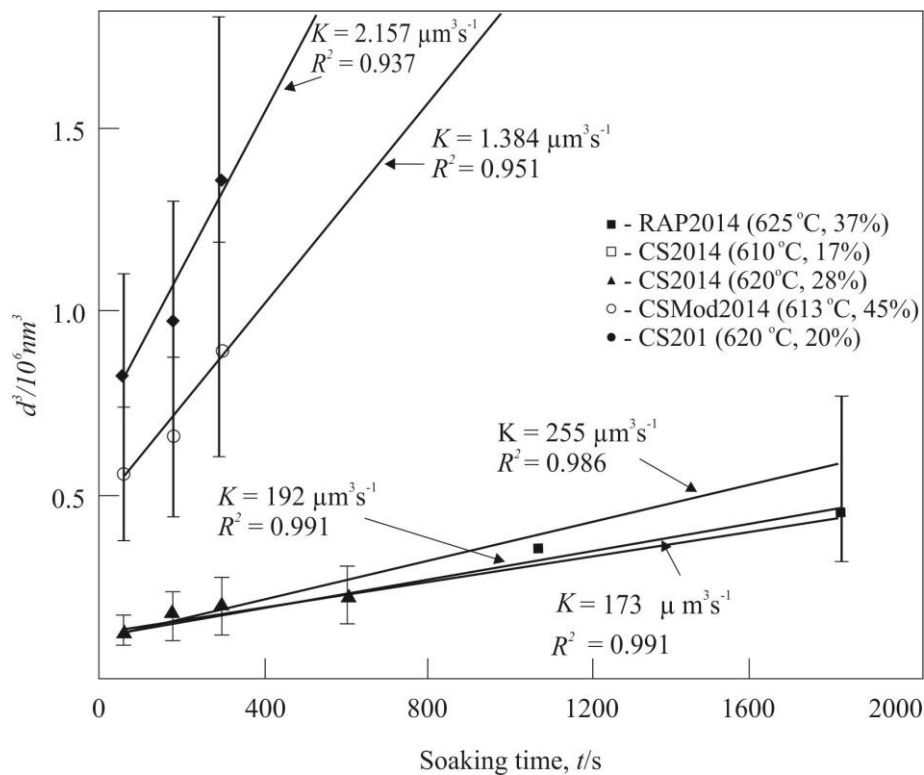


Fig.2.28 The optical micrograph of the processed specimens after soaking at 590°C for different durations, (a) 3, (b) 6, (c) 10 and (d) 15 min [73].

The experimental value of coarsening rate constant obtained in ABE process was higher than the value of coarsening rate constant in another process (SIMA, ultrasonic vibrations and angular oscillations).

The strain induced melt activated (SIMA) process involves the partial melting of heavily deformed alloy in order to obtain a fine equiaxed microstructure. The process consists of four discrete stages. First, the alloy is cast in convenient sizes to obtain a typical dendritic microstructure. Subsequently, mechanical working is done so that a directional microstructure is introduced and the thickness of the casting is decreased. The third stage involves the introduction of a critical level of stored energy in the alloy by cold working. Finally, the deformed alloy is partially remelted, within the range of 15–50 vol. % liquid, and held isothermally for a short time. The transformation of the deformed dendrites microstructure into equiaxed takes place [73].

Atkinson et al. [74] studied the coarsening of recrystallization and partial melting (RAP) 2014 and cooling slope (CS) of 2014 (Al-4Cu-0.8Si) and 201 (Al-4Cu-0.05Si) alloy. The coarsening rate for CS 201 was higher than the RAP 2014 or CS 2014 (Fig.2.29).



**Fig.2.29 Evolution of cube of average globule diameter as function of isothermal soaking time at 610–631 °C in semi-solid state for different materials [74].**

The RAP route involves mechanical working, e.g. extrusion, below recrystallization temperature followed by reheating to the semi-solid state. Recrystallization occurs during the reheating, and liquid penetrates the recrystallized boundaries to give the required spheroidal microstructure [74].

## 2.6 Mechanical Properties of Cast Al-Si Alloys

The utilization of cast Al-Si alloys depends upon the mechanical properties. Mechanical properties of cast Al-Si alloy rely upon various parameters for example; chemical composition, microstructure, casting process, grain refinement, eutectic modification, and post-processing such as thermal treatment. Their multi-phase microstructure influences the tensile properties of aluminium alloys. The mechanical properties of Al alloy can be attributed to individual phase components ( $\alpha$ -Al and Si) and morphology of these phases. According to Wang [75], the mechanical properties of Al alloys depend upon dendrite arm spacing (DAS), Mg content, size and shape of eutectic silicon. Therefore, mechanical properties of Al-Si alloy can be determined based on chemical composition, morphology of  $\alpha$ -Al and eutectic Si particles and another intermetallic phase that is present in the microstructure.

Several investigators [76-79] attempted heat treatment on semi-solid metal (SSM) cast components. Barbora et al. [76] studied the effect of T6 treatment on mechanical properties of Al-7Si alloy synthesized by the swirled equilibrium enthalpy device (SEED) process. Burapa et al. [77] studied the mechanical properties of Al-Si-Mg-Fe alloy cast through the gas induced semi-solid (GISS) process. The results signified that ultimate tensile strength and elongation depend on shape factor and grain size of  $\alpha$ -Al phase. Lin et al. [78] studied the microstructure and mechanical properties of 5052 Al alloy cast by ultrasonic vibration (USV) rheocasting process and shaped with gravity casting (GC) and high pressure die casting (HPDC). Results showed that the rheo-HPDC samples comprised a higher value of tensile strength and elongation than the value of tensile strength and elongation (%) in conventional HPDC samples. Chaoa et al. [79] studied the effects of rheocasting and heat treatment on microstructure and mechanical properties of the A356 alloy. The T5 treatment for different times (0, 5, 10, 15, 20 and 25 h) was carried out and observations revealed that aging for 20 h, exhibited the highest impact on mechanical properties.

## **2.7 Wear**

When two surfaces touch to each other, then damage on the surface of subsurface takes place. Wear is a progressive removal of material from one or both surface. Wear is deliberated using 'wear rate.' Wear rate is defined as "the loss of material per unit time or sliding distance." Mild wear occurs when worn surfaces are smooth and debris are small in size (0.01 $\mu\text{m}$  to 1 $\mu\text{m}$  in size). Whereas, severe wear has debris size about 20  $\mu\text{m}$  to 200  $\mu\text{m}$ . Different parameters for wear are roughness of the surface, sliding distance, sliding speed, applied load, composition of the alloy, mechanical properties of the alloy, area of contact, lubrication and running time. Different wear mechanisms are adhesive wear, delamination wear, corrosive wear, abrasive wear and fretting wear [79]. Two methods can protect the wear sensitive surfaces:- separation of surfaces with lubricant and by surface modification by a protective layer for instance [80].

### **2.7.1 Types of wear**

Depending on the movement or the media used in an interaction under an applied load, the wear is of following types;

#### **Adhesive wear**

This type of wear takes place when two bodies have relative motion to each other. The relative movement can be unidirectional or in the opposite direction. Adhesive wear is due to transfer of material from one surface to another surface with rotation of solid welded junctions of asperities. It leaves pits, voids or cavities on the surface. Adhesive wear takes place with low velocity, small load and smooth surfaces. This wear occurs due to adhesive bond set up whenever atoms come into contact. This is a universal type of wear and mainly occurs with any machine and cannot be eliminated but can be reduced. The addition of alloying element in the material changes the adhesion between the surfaces. i.e. addition of grain refiner in Al-Si alloy improves its machinability. During sliding, the fine grains further reduce friction as well as wear [81].

#### **Delamination wear**

Wear due to fracture beginning from surface fatigue is known as delamination wear. This leads to a sequence of pits or voids. It takes place in the rolling or sliding contact bodies such as bearings. Due to repeated cyclic load, crack occurs on the subsurface. The subsurface cracks

propagate and attach with other cracks, arrive at the surface and produce wear particles. Similarly, the surface cracks move downward into the bulk, unite with other cracks and release wear particles. Some factors influence the crack transmission. The relative humidity in the air is one of the important factors. For high moisture environment, the rate of crack growth is greater than the rate of crack growth in dry air [82].

### **Corrosive Wear**

This kind of wear occurs when sliding takes place in the corrosive or oxidative atmosphere. During sliding the oxygen from the common environment or gasses present in the surrounding can react with the solid surface. The extreme existence of anti-wear additives or other chemical mediator can lead to corrosive wear. At high temperature, oxygen can react with sliding surface and form oxides which direct to oxidative wear. This leads to the formation of corrosive/oxide layer [81].

### **Abrasive wear**

Abrasive wear mainly takes place due to sliding of hard particles along a soft surface. At high loads, it occurs more easily than adhesive wear or due to high revolution at small loads, or after the adhesive wear and continues to rotate. It leads to ploughing and cutting phenomenon. In ploughing, the material is removed from both sides and grooves formed. During sliding, the entrapped debris occurs between contact surfaces and grooves formed on one or both surface. The ridges formed during abrasion wear mechanism become flattened after some sliding distance and split due to repeated cyclic system [83]. This caused subsurface deformation and surface as well as subsurface crack nucleation. The hardness play an important role to manage the abrasive wear. The wear rate is inversely proportional to the hardness [84].

### **Fretting wear**

It mainly occurs due to reciprocal movement between two surfaces. This is two-step mechanism. In the beginning, adhesive wear occurs due to rubbing of surfaces and surfaces get oxidized because vast amount of energy stored in wear particles [81].

## **2.7.2 Wear analysis of A356 alloy**

Since Al-Si alloy has good feed ability, mechanical properties and wear resistance, they are extensively used in marine, automobile, aerospace sector and also used in various machine

parts such as cylinder blocks, connecting rods, pistons and engine blocks. Such applications require excellent tribological properties of Al-Si alloys. The tribological properties depend on the correlation between the microstructure and mechanical properties [85]. Several investigators studied wear of Al alloys. Das et al. [86] studied wear of an A356 alloy prepared in the cooling slope rheocasting process. The results exemplified that rheocast A356 alloy at 60° cooling slope showed lower wear rate when compared to 45° slope rheocast and gravity cast samples. Rheocast A356 alloy at an angle of 60° exhibited more and more globular  $\alpha$ -Al phase, while rheocast A356 alloy at an angle of 45° illustrated mixture of dendrites, rosette and spherical  $\alpha$ -Al phase, whereas gravity cast A356 alloy comprised dendritic morphology. Dey et al. [87] studied the wear analysis of A356 alloy. The results confirmed that rheocast A356 alloy comprised higher mechanical properties and wear resistance than conventional cast A356 alloy. Alhawari et al. [88] investigated the wear properties of A356/Al<sub>2</sub>O<sub>3</sub> metal matrix composite in a semi-solid state. The results demonstrated a lower volume loss for semi-solid cast metal matrix composite when compared with conventional casting method. Kumar et al. [89] studied the effect of grain refiner and modifier on the wear properties of Al-7Si and Al-7Si-2.5Cu alloys. The observations manifested that grain refiner and modifier increased the wear resistance of the alloy. Thuong et al. [90] illustrated the microstructure evolution and wear analysis of A356 alloy prepared by the equal channel angular pressing process (ECAP). Their observations showed that microstructure was more homogeneous for the ECAP processed A356 alloy than the conventional cast A356 alloy. The wear resistance of ECAP processed alloy was higher than conventional cast A356 alloy owing to higher hardness and uniform distribution of Si phase.

As discussed in literature in Al-Si alloy, the primary  $\alpha$ -Al phase is dendritic, which leads to inferior mechanical properties. If dendritic morphology can be changed to non-dendritic morphology, then the casting products will be free from any defects, and alloy possess higher mechanical properties. Semi-solid processing (SSP) is one of the methods of producing spherical structure and is also an attractive material processing method than traditional casting and forging processes. In the present work, A356 alloy is used since the alloy illustrated foundry importance, good castability and wide freezing range. Therefore, A356 alloy has been selected for semi-solid metal processing by rheometal process.



## 2.8 Objectives of Present Study

On the basis of literature review, the objectives of the present research work are categorized in following heads.

- Study of different process parameters (stirring speed, solid fraction, and holding time) for SSM slurry by RSF process on the morphology of primary  $\alpha$ -Al and eutectic Si of A356 alloy.
- Analysis of variation in surface morphology of EEM during stirring at various time intervals
- Investigation of the above effects with different characterization techniques such as XRD, DSC, SEM and SEM with EDX.
- The effect of flow pattern on the morphology of  $\alpha$ -Al phase without and with baffles.
- Optimization of grain refiner with different content of Al-5Ti-1B in conventional cast A356 alloy. The addition of optimum grain refiner in rheometal cast A356 alloy to observe the effect of grain refiner on the morphology of primary  $\alpha$ -Al phase.
- Study about mechanical properties and wear analysis of A356 alloy in different processing conditions with the help of a T5 heat treatment. Comparison between the non-heat-treated and heat-treated A356 alloy.

# CHAPTER 3

## MATERIALS AND METHODS

---

This chapter deals with the materials and methods used in the thesis. The chapter is divided into two parts. First part is concerned about the synthesis of A356 alloy, preparation of enthalpy exchange material (EEM), synthesis of semi-solid slurry with and without grain refiner and heat treatment of the semi-solid mass. The second part provides information about various characterization techniques used in the thesis.

### 3.1 Synthesis of A356 Alloy

The A356 alloy was prepared from Al-13%Si master alloy and pure Al using standard mass balance equation. Calculations for preparing A356 alloy from Al-13% Si and pure Al is given in appendix 1.

As-cast A356 alloy was cast by a conventional casting method. Melting was carried out in an electric resistance furnace maintained at a temperature of 720°C with an accuracy of  $\pm 5$  °C. Flux was used to remove dross and to avoid oxidation of the melt. Hexa-chloro-ethane (C<sub>2</sub>Cl<sub>6</sub>) tablets were used for degassing of the melt. After degassing, the melt was poured in the permanent steel mold. Steel mold was coated with lime and dried before pouring the melt. After that, castings were used for further examination. The chemical composition of the A356 alloy is given in table 3.1.

**Table.3.1: Chemical composition of the A356 alloy**

Element	Si	Mg	Cu	Fe	Mn	Ti	Pb	Sn	Zn	Al
% wt	6.8	0.4	0.15	0.18	0.026	0.09	0.026	0.024	0.04	Balance

### 3.2 Preparation of Enthalpy Exchange Material (EEM)

The EEM had the same composition as that of the melt. A356 was melted in an electric resistance furnace maintained at a temperature of 700°C with the accuracy of  $\pm 5$  °C. The fluxing and degassing was done to avoid the formation of dross and removal of gasses from the melt respectively. After degassing, the melt was poured into the cylindrical die of predefined

dimensions. A steel rod was placed in the center of the mold to hold the EEM mass. The steel rod was coated with lime to prevent any iron pick up by the melt. After solidification, the solid EEM attached to steel rod was taken out. The calculations for EEM with solid fraction of 20, 30 and 40 wt.% of melt are given in appendix 2. Dimensions of EEM for obtaining different solid fractions are given in Table 3.2.

**Table.3.2: Dimensions of EEM for different solid fractions**

Solid fraction (wt.%)	Mass of EEM (kg)	Length of EEM (m)	Diameter of EEM (m)
20	0.264	0.051	0.05
30	0.373	0.073	0.05
40	0.496	0.097	0.05

Trials runs were taken for 20, 30 and 40 wt.% semi-solid slurry at different stirring speeds (400, 600, 800, 1000 and 1200 rpm). The microstructural features regarding average grain size and shape factor of primary  $\alpha$ -Al phase were studied and found optimum for the solid fraction of 30 wt.% for each and every stirring speed. Falak et al. [91] studied the rheocasting of Al-7.1%Si alloy for stirring speeds of 500, 1000, 1500 and 2000 rpm at the solid fraction of 11, 24 and 38 wt.%. Their observation showed that for the given shear rate as the solid fraction increased the average grain size and shaped factor of primary  $\alpha$ -Al phase continuously increased. Cosic et al. [92] studied the effect of solid fraction (30, 40 and 50 wt.%) at the stirring speed of 500 rpm for Al-18Si alloy. The results showed that as solid fraction increased the average grain size of primary  $\alpha$ -Al phase continuously increased. From the observation, it was also found that as the solid fraction increased the coarsening of Si particles occurred due to agglomeration and sintering of Si particles. Because of this agglomeration process, the hardness of the alloy decreased as solid fraction increased. Hence, based on the previous findings and present investigation 30 wt.% semi-solid slurry was taken for detailed study by the experiments.

### 3.3 Synthesis of Semi-Solid Slurry

#### 3.3.1 Without grain refiner

A schematic diagram of the experimental set-up used in the process is shown in Fig. 3.1. The steel rod with EEM was joined to a motor having a rotation speed of 1800 rpm. Figure 3.2 indicates the formation of semi-solid slurry in different stages.

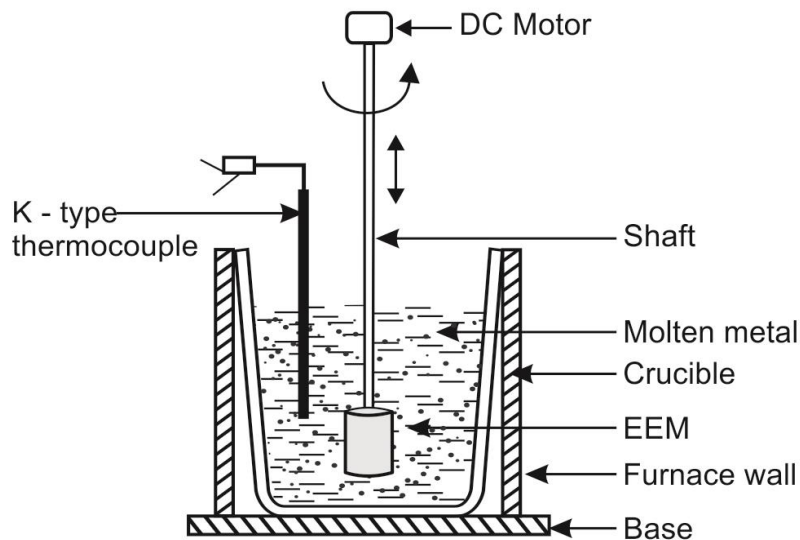


**Fig.3.1. Schematic set-up for rheometal process.**

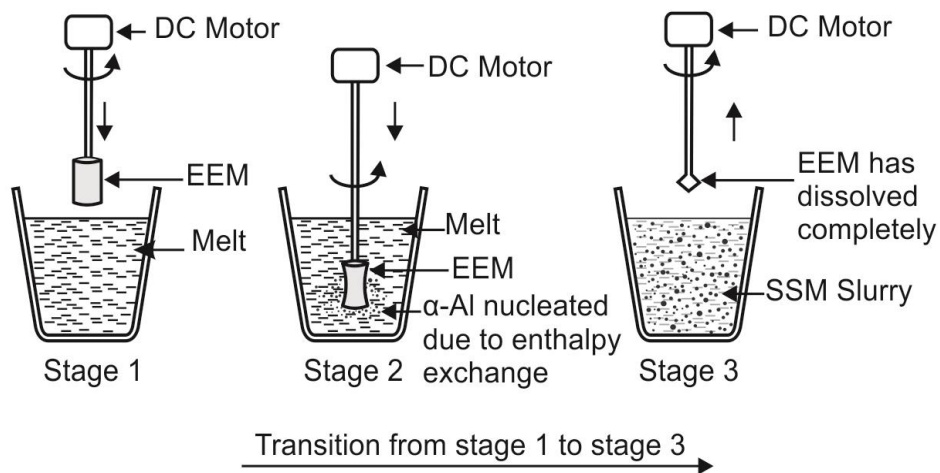


**Fig. 3.2 Schematic illustration of different stage involved in rheometal process.**

In this process, 1.35 kg of A356alloy was taken in a graphite crucible and melted in an electric resistance furnace maintained at a fixed temperature 700 °C with the accuracy of  $\pm 5^\circ\text{C}$ . A K-type thermocouple was used to measure the actual temperature of the melt. The EEM initially at room temperature was immersed slowly in the melt and was stirred at different stirring speeds (400, 600, 800, 1000 and 1200 rpm). During stirring, the slurry was rapidly formed within 30 seconds at a temperature of 597°C. Pompe et al. [93] showed that a high quenching

rate is required to preserve the solid-liquid microstructures. Therefore, the slurry was quenched in the water after achieving the desired conditions.

For the study of surface morphology of EEM at different time intervals, experiments at stirring speed of 1000 rpm were conducted. Therefore, before complete dissolution, the EEM was taken out from the melt after different stirring times 5, 10, 15, 20 and 25 seconds. The weight of EEM at varying time intervals was taken and showed in table 3.3. The microstructural examination was conducted at the outer surface of partially melted EEM at different time intervals. A new EEM was used for each test. For obtaining microstructure total, 7 EEMs were used.

**Table.3.3: Weight of EEM after dissolution in melt with different stirring time**

Time (Sec)	0	5	10	15	20	25	30
Mass (kg)	0.373	0.192	0.172	0.129	0.101	0.061	0.003

Coarsening kinetics after 3, 5, 10, and 15 mins at different stirring speeds (400, 600, 800, 1000 and 1200 rpm) was also considered. The semi-solid slurry was isothermally kept at a temperature of 597 °C followed by quenching in water at different holding time.

Effects of varying solid fraction (20, 30 and 40 wt.%) for stirring speed of 1000 rpm, temperature 597°C and 0 min holding time was also observed.

Experiments for without and with baffled crucible were also executed. Baffles were employed to study the effect of flow pattern on the melt for stirring speed of 1000 rpm. Four baffles of equal width were placed along the crucible walls at the azimuthal variation of 90°.

### **3.3.2 Addition of Al-5Ti-1B master alloy**

A varying amount of Al-5Ti-1B master alloy (0.2, 0.4, 0.6 and 0.8 wt.%) was added to melt in conventional casting method to obtain the optimum level of grain refiner regarding SDAS value. The optimum level of grain refiner was added in the rheometal slurry to facilitate more nucleation sites in the melt. The addition of grain refiner was done by wrapping the grain refiner in an Al foil to prevent its loss from the furnace. After addition of grain refiner, the furnace power was turned off and the degassed melt was kept for 5 minutes before stirring. The EEM initially at room temperature was slowly immersed into the melt and stirring started at a

preset rotational speed of 1000 rpm with the help of D.C. motor. After this, the formation of semi-solid slurry took place within 30 seconds. This was followed by transferring the slurry into the water for quenching to restore the microstructure at a given temperature.

S. No.	Experiment conditions	Sample designation
--------	-----------------------	--------------------

### 3.4 Heat Treatment

The mechanical properties of A356 alloy in different processing conditions were studied with T5 heat treatment. Different processing conditions used in the present work are shown in table 3.4.

The semi-solid mass at a temperature of 597°C was transferred in the die with an inner diameter of 84 mm, 12 mm wall thickness and height of 99 mm. The die was preheated to 300°C (Fig.3.3) followed by a pressure of 30MPa on the semi-solid mass through the plunger. Later on, the casting was ejected from the die with the help of tools. In the T5 heat treatment, the aging of some cast components was carried out at 170°C for the period of 20 hrs.

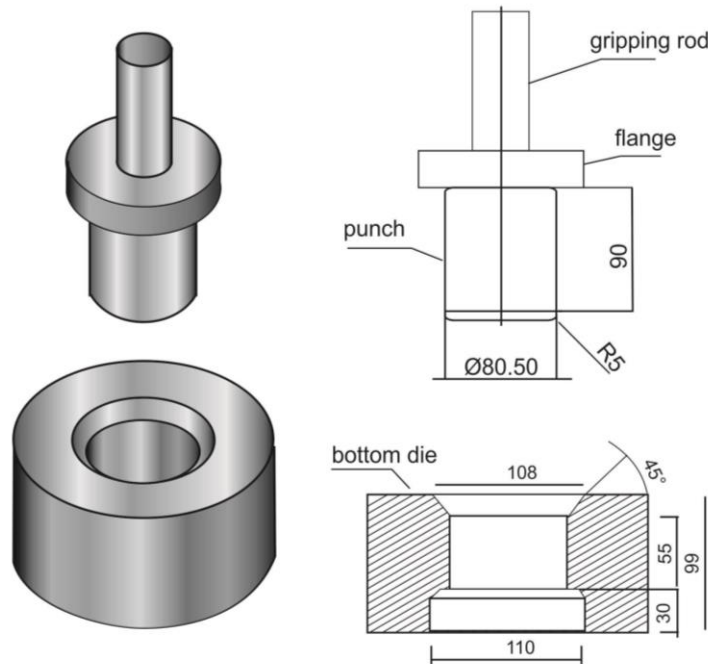


Fig. 3.3 Schematic representation of die used in rheometal process.

1	As-cast	A
2	Without baffle, without grain refiner	B
3	Baffle without grain refiner	C
4	Grain refiner without baffle	D
5	Baffle with grain refiner	E

**Table.3.4: Different conditions used for mechanical properties**

### 3.5 Characterization of A356 Alloy

#### 3.5.1 Microstructural analysis

Microstructure investigations were carried with standard metallographic procedures for Al alloys. The samples were polished using emery paper of grade 0/0, 1/0, 2/0, 3/0, 4/0 and disc polished with alumina of grit 600, 800, and 1000. The samples were etched with Keller's reagent and samples were placed under the optical microscope (Model: SuXma- Met I, Conation Technologies). ASTM International test standards E 112-12 were used for measuring the average grain size. Shape factor was also measured as the ratio of shortest length to maximum length which is given as;

$$SF = \frac{d_{min}}{d_{max}} \quad (3.1)$$

#### 3.5.2 Porosity measurement

The porosity for A356 alloy in different processing conditions was calculated using Archimedes principle [5] in the following manner

$$P (\%) = [1-(D_a/D_m)] \times 100 \quad (3.2)$$

Where;

$D_a$  = Experimental density of sample

$D_m$  = Theoretical density of sample

Here  $D_m = 2.685 \text{ gm/cm}^3$  for A356 alloy.

The experimental density of the samples was calculated using the Mettler Toledo, ME-DNY-4 density measurement kit.

### **3.5.3 X-Ray diffraction (XRD) analysis**

To identify the stoichiometry of existing phase, XRD analysis was carried out for the A356 alloy in different conditions using X'pert Pro PANalytica X-Ray diffractometer unit with a  $\text{CuK}\alpha$  ( $\lambda = 0.1540598 \text{ nm}$ ) source. Diffraction measurements were performed in the angle range of  $20^\circ$  to  $90^\circ$  at step size  $0.05^\circ$  with scan step time 0.8sec using  $\text{Cu-K}\alpha$  radiation (40kV, 40mA).

### **3.5.4 Thermal analysis**

Pieces of 10mg in weight were used as a sample, for differential scanning calorimetry (DSC) (Netzsch DSC 404 F3) analysis were properly cleaned. Nitrogen gas was used for controlled atmospheric conditions and the cooling rate was 10 K/min. DSC was used to record the eutectic and liquidus temperature of the alloy under different conditions.

### **3.5.5 Scanning electron microscopy (SEM)**

The morphology of cast A356 alloy was also examined using SEM (Nova Nano450SEM, FEI, North America) operated at 15-20 kV. Energy dispersive X-ray spectroscopy (EDS) detector (Bruker, Germany) was employed for phase composition and elemental mapping for phase identification.

In addition to this morphology of non-heat-treated and heat-treated samples were characterized using W-SEM (Carl Zeiss) at Department of Material Science and Engineering, IIT Kanpur.

## **3.6 Mechanical Properties**

### **3.6.1 Hardness**



The hardness of test specimens was calculated using the Brinell hardness testing machine. The polished sample was placed under the microscope for proper selection of the area to obtain the hardness value. The steel ball indenter of 10 mm was used under the load of 500 kgf for a dwell time of 15s to get the indentation mark (Fig.3.4). Four readings were taken for each sample and the hardness value was calculated using formula,

$$\text{BHN} = \frac{P}{\frac{\pi D}{2}(D - \sqrt{D^2 - d^2})} \quad (3.3)$$

Where;

D = Diameter of ball indenter

d = diameter of indentation

P =load.

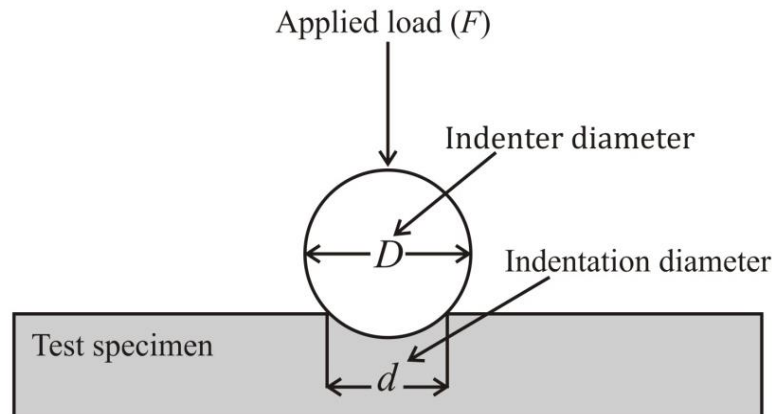


**Fig. 3.4 Schematic depiction of the Brinell indentation.**

### 3.6.2 Tensile properties

Tensile properties for non-heat-treated and heat-treated samples were calculated to evaluate the impact of heat treatment on A356 alloy. Tensile test specimens were machined, and dimension of tensile specimens is given in Fig.4.4. Tensile tests were performed H25KTinius Olsen machine at room temperature with a strain rate of 1 mm/min. For obtaining the results, five specimens were used each and every time. The ultimate tensile strength (UTS), yield strength (YS) and ductility regarding percentage elongation were calculated.

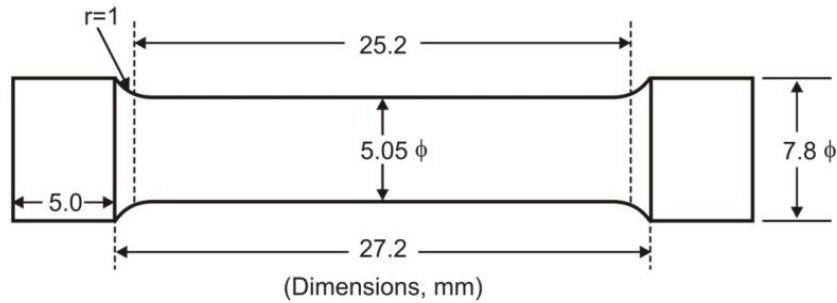


**Fig. 3.5 Dimensions of tensile sample.**

### 3.6.3 Fractography

Fracture surface characterization studies for all non-heat-treated and heat-treated samples were performed on tensile fracture surface with SEM to observe the mode of fracture.

### 3.7 Wear Analysis

Experiments for wear analysis of A356 alloy were conducted with a pin on disc test machine. Dry sliding wear tests were carried out on 6 mm diameter and 25 mm long cylindrical wear pins. The round faces of the specimens were kept in contact with the slider disc. The counterface disc was made of EN31 steel. The diameter of the disc was 50 mm and was cleaned with acetone before each wear test. The tests were carried out at a sliding velocity of 1 m/s and 15N loads for a total sliding distance of 3600 m. Table 3.5 shows experimental parameters used in the present investigation. After each experiment, the steel disc was reground to restore the original surface conditions and new test pin was used for each experiment. Test pins were cleaned with acetone before the test. Tests were conducted at room temperature. Weight loss after wear was calculated by subtracting the final weight from the initial weight. The volume loss was measured by dividing the weight loss by the density of the alloy.

$$\text{Volume loss} = \frac{\text{weight loss}}{\text{density}} \quad (3.4)$$

Where:

$$\text{Volume loss} = \text{m}^3$$

$$\text{Weight loss (g)} = (\text{Weight before wear} - \text{weight after wear})$$

$$\text{Density (g/cm}^3\text{)} = 2.685 \text{ for A356 alloy (standard value)}$$

Specific wear rate was also calculated by dividing the volume loss with load and total sliding distance. SEM was employed to analyze the worn surfaces.

$$S. W. R = \frac{\text{Volume loss}}{\text{load} \times \text{sliding distance}} \quad (3.5)$$

S.W.R=Specific wear rate (mm<sup>3</sup>/N mm)

Load= applied load (Newton)

Sliding distance= total distance (m) (3600m)

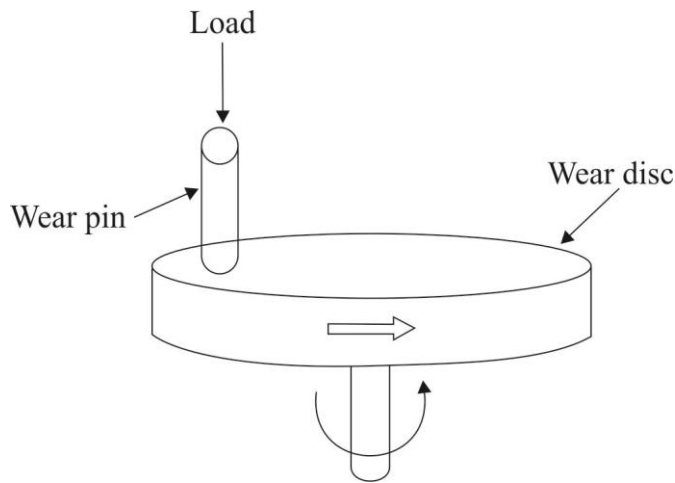


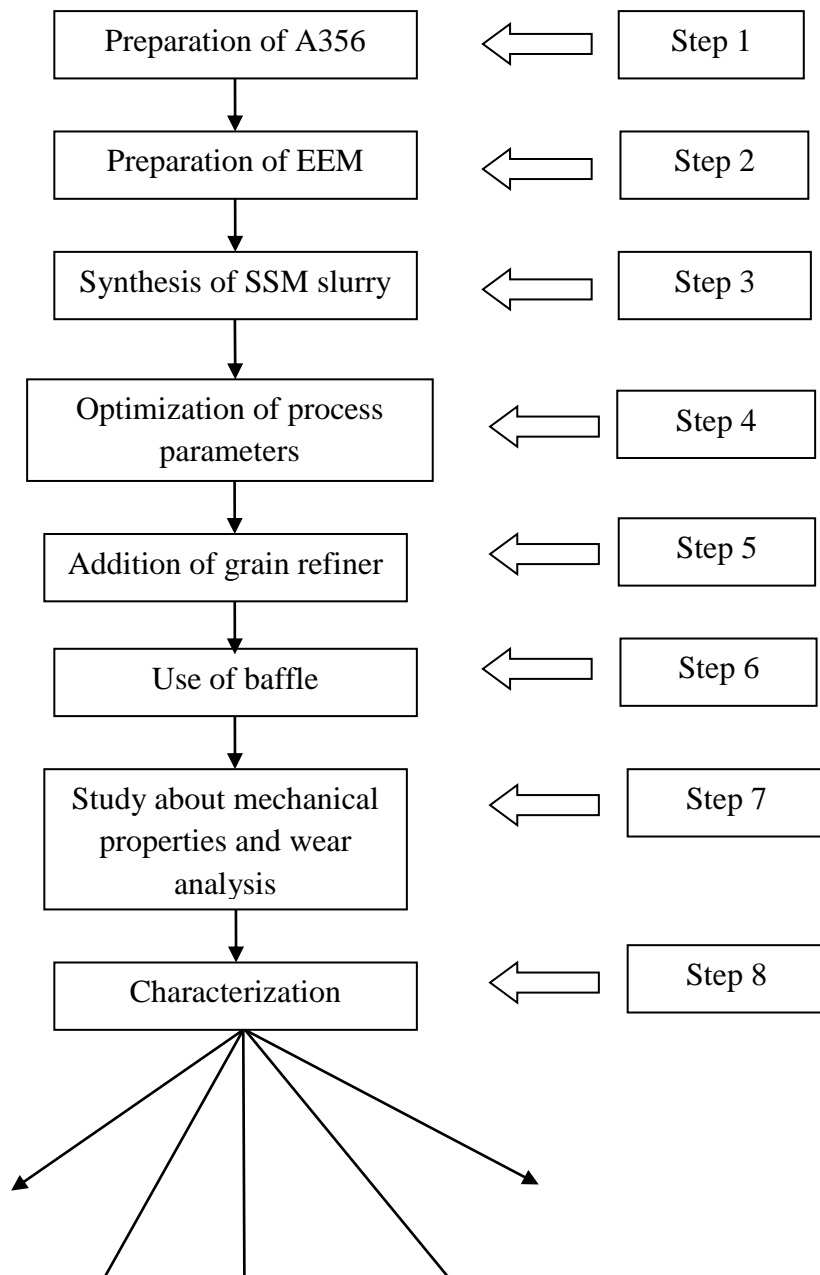
**Fig. 3.6 Schematic representation of pin on disc apparatus.**

**Table.3.5: Experimental parameters used for wear analysis**

S. No.	Name of parameters	Range
1	Room temperature	28 °C
2	Humidity	40
3	Load	15 N
4	Speed	1m/s
5	rpm	375
6	Radius of disc	25 mm
7	Distance	3600 m

8	Duration	60 min
---	----------	--------

Flow chart for materials and methods used in RSF process is shown in Fig.3.7.



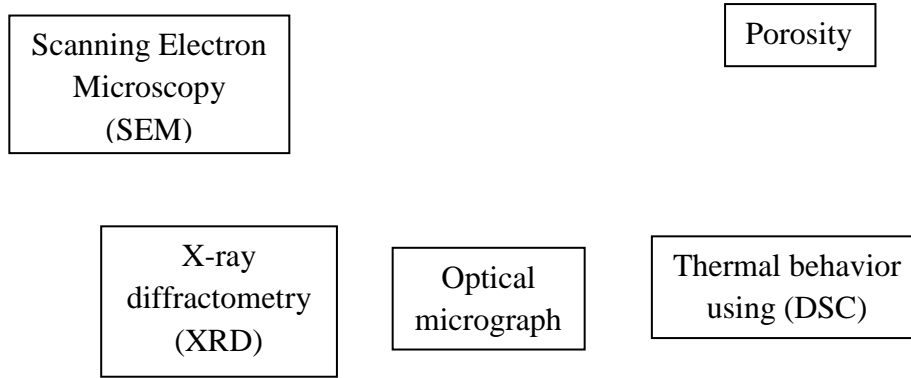


Fig.3.7 Flow chart for materials and methods used in rheometal process.

## CHAPTER 4

### MICROSTRUCTURES EVOLUTION THROUGH RSF PROCESS

---

This chapter discusses the microstructure evolution as it depends on different process parameters for the A356 alloy in the rheometal process. Microstructural changes from dendritic to rosette and later to globular morphology as a function of stirring time takes place. Stirring speed converts the dendritic  $\alpha$ -Al phase to globular morphology. The average grain size of  $\alpha$ -Al decreased as stirring speed increased. The effect of flow pattern on the morphology  $\alpha$ -Al phase has also been studied with the help of baffles. Without baffle, a swirling motion in the crucible is produced and within this vortex formation an adequate mixing does not take place. The uses of baffles suppress vortex formation and converts the swirling motion into a preferred flow pattern so that proper mixing may take place. Optimization of grain refiner with different content of Al-5Ti-1B in conventional cast A356 alloy has also been carried out. The addition of optimum grain refiner in rheometal cast A356 alloy is done to observe the additional effect of grain refiner on the morphology of primary  $\alpha$ -Al phase. The rate of coarsening kinetics was discussed on conventional diffusional Lifshitz, Slyozov and Wagner (LSW) theory, coarsening by convective mass flow and coalescence by stirring speed. Characterization regarding the morphology of primary  $\alpha$ -Al and eutectic Si has been carried out.

#### 4.1 Effect of Time on EEM Dissolution During Stirring

Figure 4.1 illustrates the effect of time on EEM dissolution during stirring. Microstructures at various stirring times comprised  $\alpha$ -Al and eutectic Si phase. Figure 4.1(a) shows that as-cast A356 alloy exhibits a columnar dendritic growth with secondary dendritic arm spacing (SDAS) of 58 $\mu$ m. While Fig. 4.1(b) demonstrates a reduction in SDAS value to 49  $\mu$ m. Likewise, the

value of SDAS decreases from 42 to 22  $\mu\text{m}$  in Fig. 4.1(c-d). Figure 4.1(e) illustrates rosette morphology of  $\alpha\text{-Al}$  phase. Reduction in the size of dendrites implied deformation of dendrites due to shearing which leads to fragmentation and partial melting of dendrites during slurry formation [94]. Figure 4.1(f) exemplifies globular  $\alpha\text{-Al}$  phase having an average grain size about 55 $\mu\text{m}$  for stirring time of 25 seconds. Hence, from the given results, it is cleared that shear flow and along the curved interfaces stimulated the transformation of dendrites into globular morphology.

For a stirring time of 30 seconds, the EEM was completely dissolved in the melt. From above results, it is clear that as stirring times increased,  $\alpha\text{-Al}$  phase changed its morphology from dendritic to rosette and finally globular morphology.

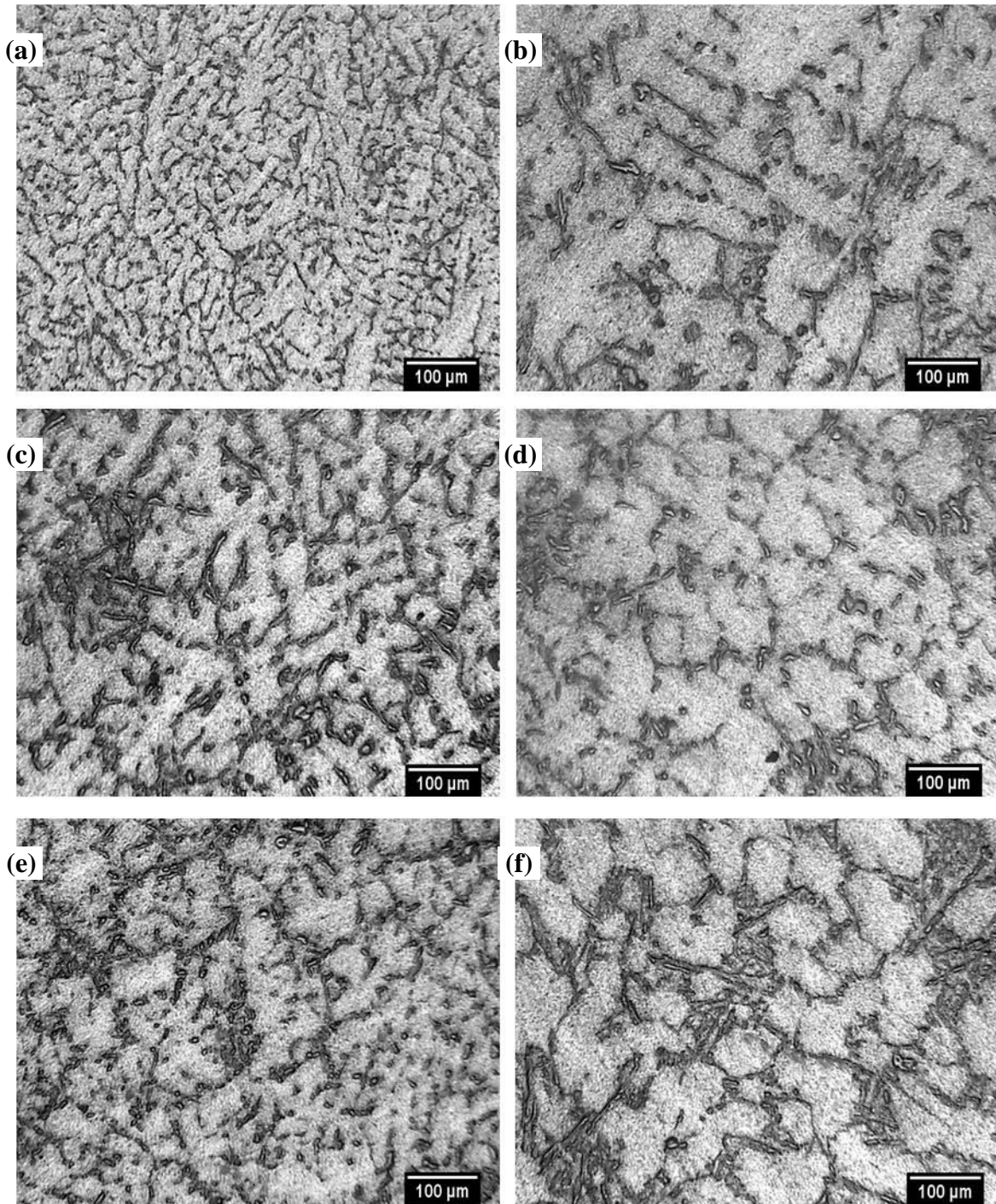


**Fig.4.1 Optical micrographs of EEM for primary  $\alpha$ -Al phase at stirring time (a) 0, (b) 5, (c) 10, (d) 15, (e) 20 and (f) 25 seconds.**

Figure 4.2 shows the mass of EEM after immersion of EEM in the melt at different stirring times.

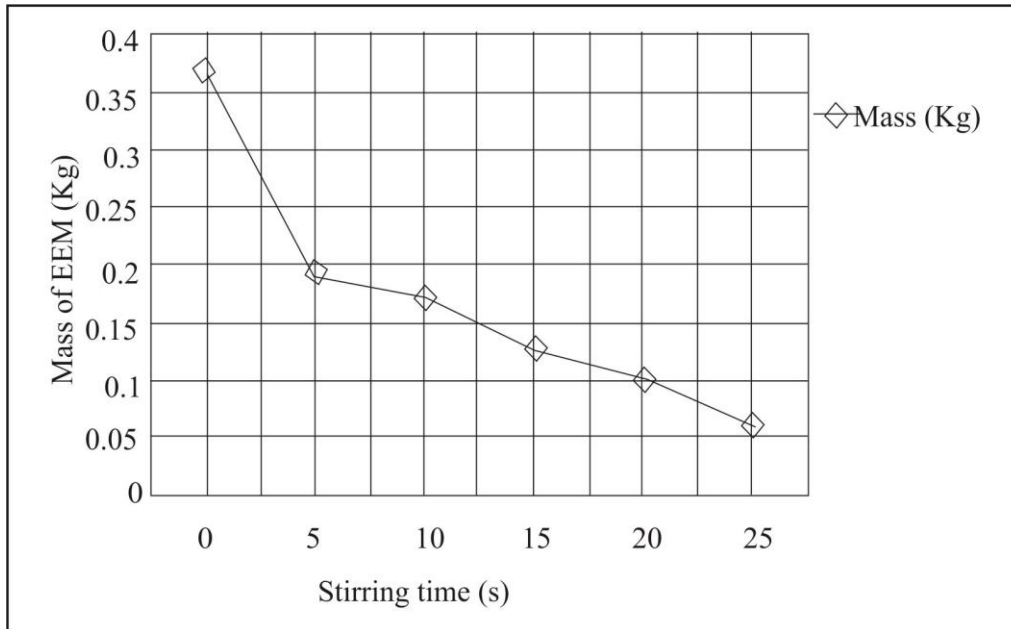


**Fig.4.2 Weight of EEM with various stirring time.**

The effect of various time intervals on eutectic Si is given in Fig. 4.3(a-f). Figure 4.3(a) depicts long needle type structure for stirring time of 0 sec. Figure 4.3(b-f) reveals that as stirring time increased the size of Si needles decreased and rounding of edges of Si needles for stirring time of 25 seconds takes place. Some of the Si needles also converted into a somewhat globular morphology. This is ascribed into the fact that stirring time of 25 seconds comprised enough time for transformation in globular morphology [94-96].



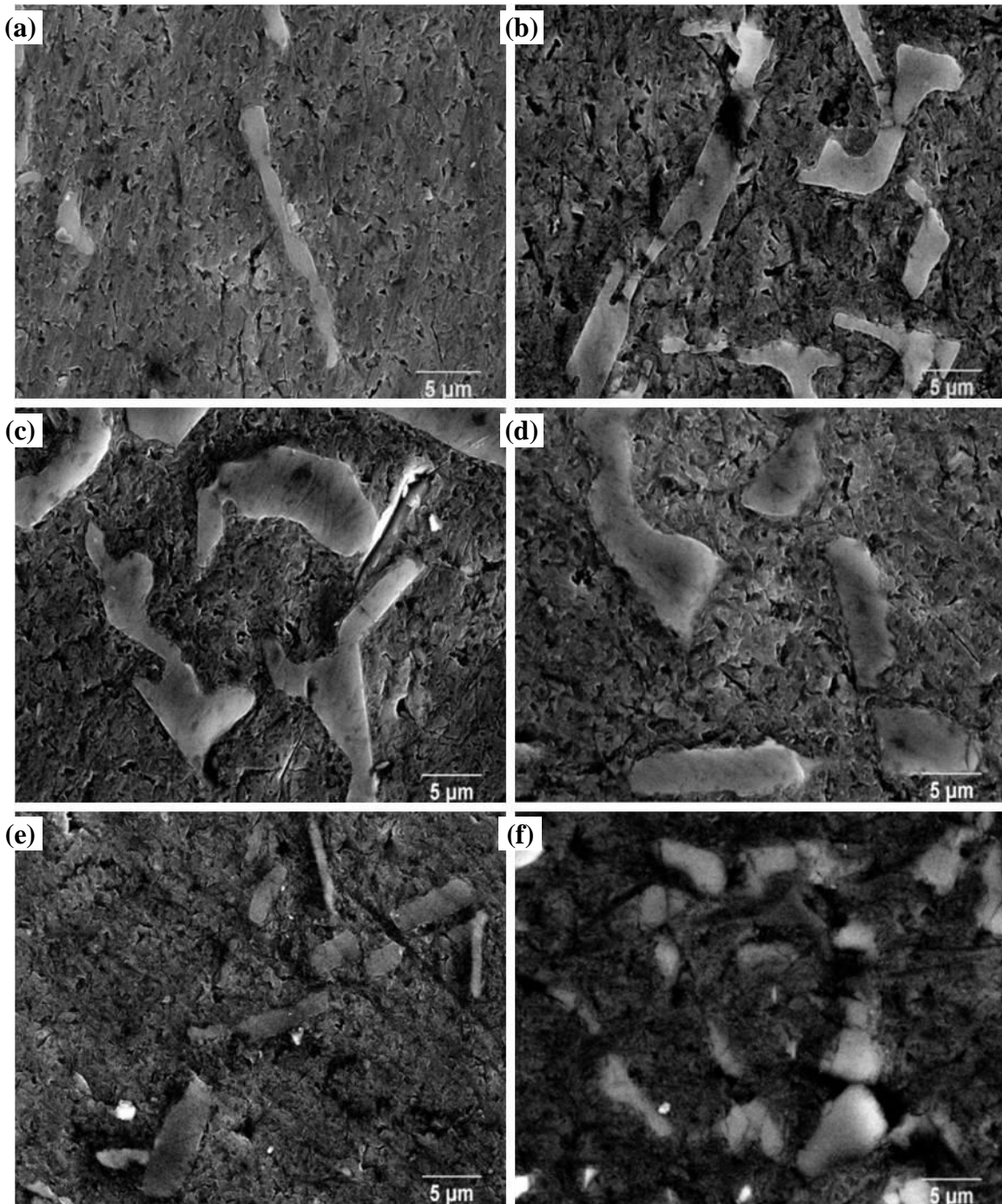


**Fig. 4.3 SEM micrographs of EEM for eutectic Si at stirring time (a) 0, (b) 5, (c) 10, (d) 15, (e) 20 and (f) 25 seconds.**

#### **4.2 Effect of Stirring Speed on Microstructure; Without and With Baffles**

When a cylindrical EEM was dissolved in the melt and stirred at 400 rpm, there was an exchange of heat between the melt and solid EEM. The rotating cylinder set the melt into a rotational flow itself. This turbulent flow is a variant of the Taylor-Couette flow [97] since the initial Reynolds number is around 16000 at 400 rpm. Stirring at higher stirring speeds

comprised Reynolds number about 24000 at 600 rpm, 32000 at 800 rpm, 40000 at 1000 rpm and 48000 at 1200 rpm. Calculation for Reynolds number at different stirring speeds is given in appendix 3.

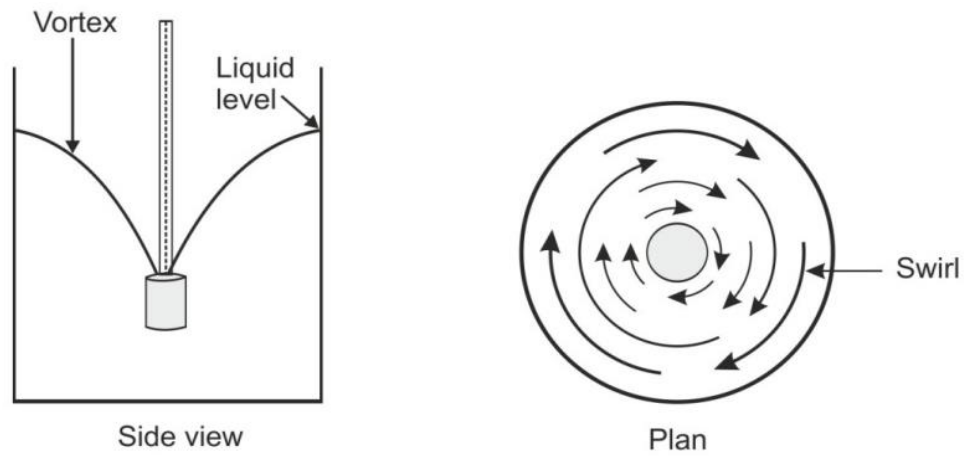
The heat transfer, between the melt and EEM, takes place. The rate of heat transfer depends on the boundary conditions between the melt and the EEM. The heat transfer at the melt-EEM interface is governed by convection and conduction. The rotational motion of the EEM can be interpreted based on the principle of fluid mechanics and convective heat transfer [94]. The rotational flow induces itself a thermal boundary layer at the cylindrical EEM. Outside the boundary layer, the temperature is almost constant, while inside the boundary layer a steep temperature gradient exists. Due to this gradient, heat transfer between the melt and the EEM is accelerated. The process of immersion and melting can be explained as heat to EEM is moved by heat diffusion until the flow field in melt is established and thus, the boundary layer increased heat transfer from the melt to the EEM. Once the surface of the EEM is at eutectic temperature, the EEM melts rapidly, first by dissolving the interdendritic eutectic while the temperature in the still solid part of the EEM increases further. The dissolution of eutectic opens the dendritic structure feeling the shearing motion of the surrounding fluid and melting off dendrite arms can take place ejecting these into the melt. This process starts naturally from the periphery and is ending at the center. The ejected dendrite arms subsequently, work as nuclei for solidification and as the entities which coarsen and form the solid-liquid structure. Ultimately, the slurry with 30 wt.% solid fraction is acquired with a globular  $\alpha$ -Al phase. The fluid flow pattern inside the melt is complex once the solid EEM penetrates while rotating into the melt (it is not a simple Taylor-Couette flow). Especially when the EEM is completely dissolved in the melt a turbulent flow pattern will exist, slightly damped by the viscosity of the slurry. The stirrer design, rotation speed, crucible geometry and slurry viscosity determine the flow pattern.

The stirrer creates a flow pattern in the system owing to spread of liquid throughout the crucible and returned eventually to the stirrer. The stirrer comprised three major tasks; (i) dissolve solid into a liquid, (ii) prevent agglomeration of the solid droplets in any part of the crucible and (iii) provide convective heat transfer to the cooling surface [98].

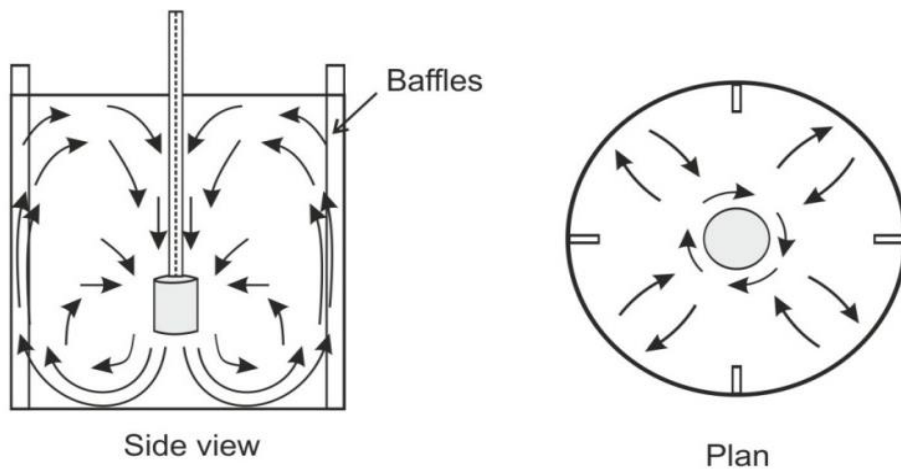
The velocity of the fluid in crucible has three velocity components and overall flow pattern in the crucible depends on the local variation of these three elements. The first element is radial which works in a direction perpendicular to the shaft of the stirrer. The second component is

longitudinal and acts in a direction parallel to the shaft. The third element is tangential or rotational and moves in a direction tangent to a circular path around the shaft as shown in Fig. 4.4(a). In general, the radial and tangential components are in a horizontal plane and the longitudinal component in the vertical direction. The radial and longitudinal components are useful which give necessary flow for the mixing action. The tangential flow creates a vortex at the surface of the liquid as shown in Fig. 4.4(a).

Without baffle, the crucible produced swirling motion and due to this vortex formation takes place which lacks adequate mixing. In such situations, agglomeration of particles may occur. Vortex formation leads to air aspiration which is not desirable. This phenomenon can be avoided by using baffles along the crucible walls. Typically, four baffles of equal width and 1/10 of crucible diameter were placed vertically along the crucible walls at 90° intervals as shown in Fig. 4.4(b). The baffles were coated with lime to avoid the iron pick from the melt. The purpose of baffles was to suppress vortex formation and convert swirling motion into a preferred flow pattern so that proper mixing may take place [99-100]. Baffles impede the rotational flow without interfering with radial or longitudinal flow; as a result vortex formation was avoided and particles agglomeration was also minimized.



(a)



(b)

**Fig. 4.4 Typical flow pattern in (a) un baffled and (b) baffled crucible.**

Figure 4.5(a) exhibits the optical micrograph for as-cast A356 alloy where the dendritic  $\alpha$ -Al phase is present. Figure 4.5(b-f) for rheometal processed A356 alloy at different stirring speeds. Figure 4.5(b-f) reveals that the A356 alloy exhibited globular  $\alpha$ -Al phase. High stirring speeds reduce the average grain size of  $\alpha$ -Al phase and produces fine grains.

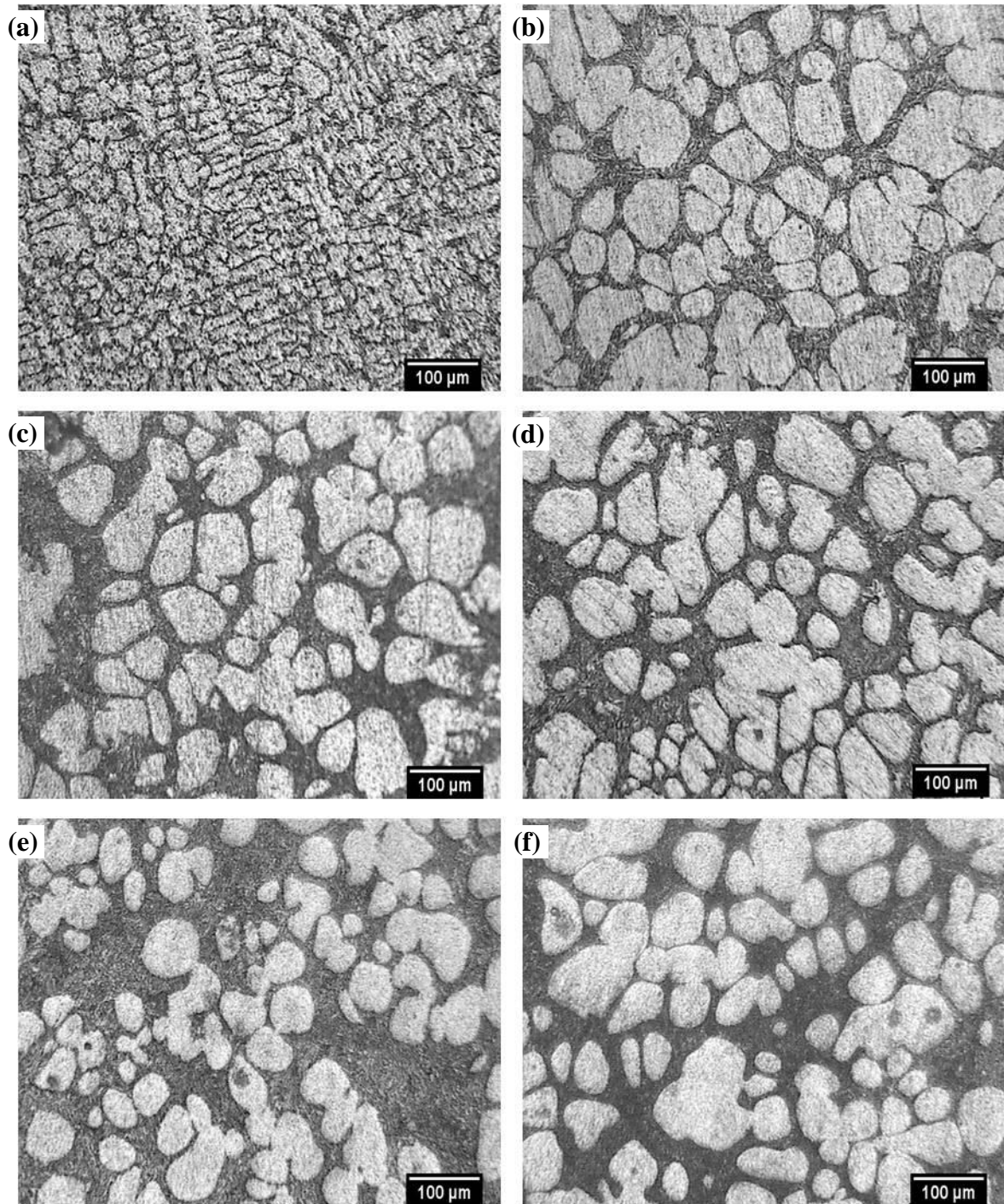


**Fig. 4.5 Optical micrographs of(a) as-cast, stirred at (b) 400, (c) 600, (d) 800, (e) 1000 and (f) 1200 rpm water quenched semi-solid slurry at 0 min holding time.**

Figure 4.6 shows the effect of stirring speeds on average grain size and shape factor of  $\alpha$ -Al phase. The results manifested that as shear force increases, the shape factor upto 1000 rpm continually increases. As stirring speed increases further to 1200 rpm, the shape factor decreases. At 1200 rpm high turbulence creates a chance of entrapment of gas porosity.

Therefore, the best results were obtained for stirring speed of 1000 rpm regarding average grain size and shape factor.

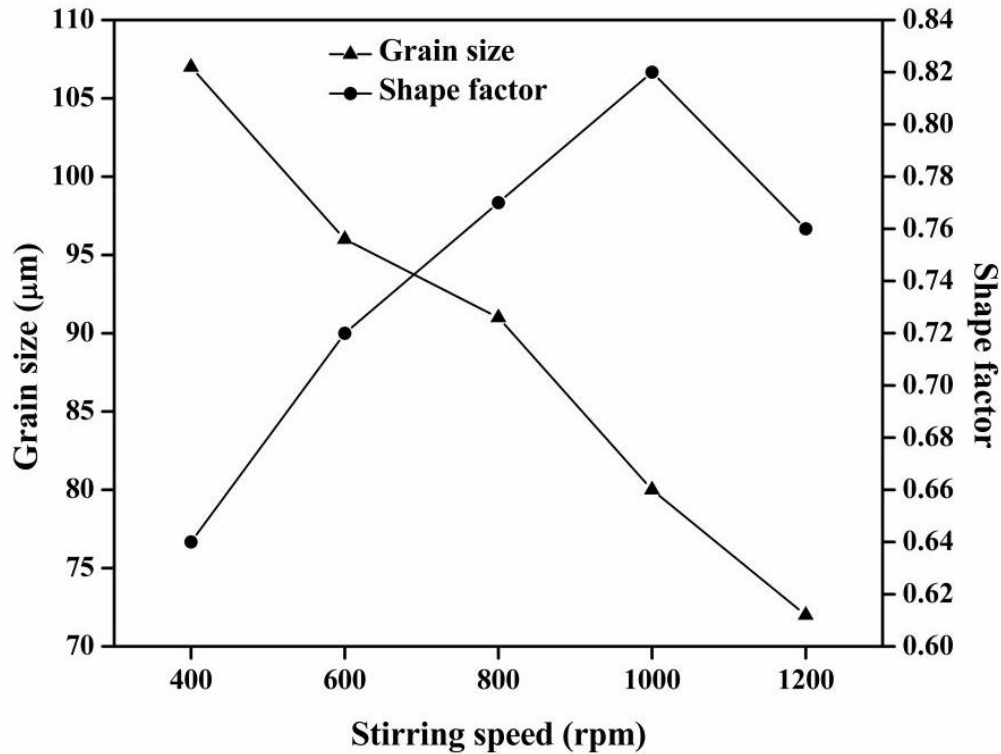
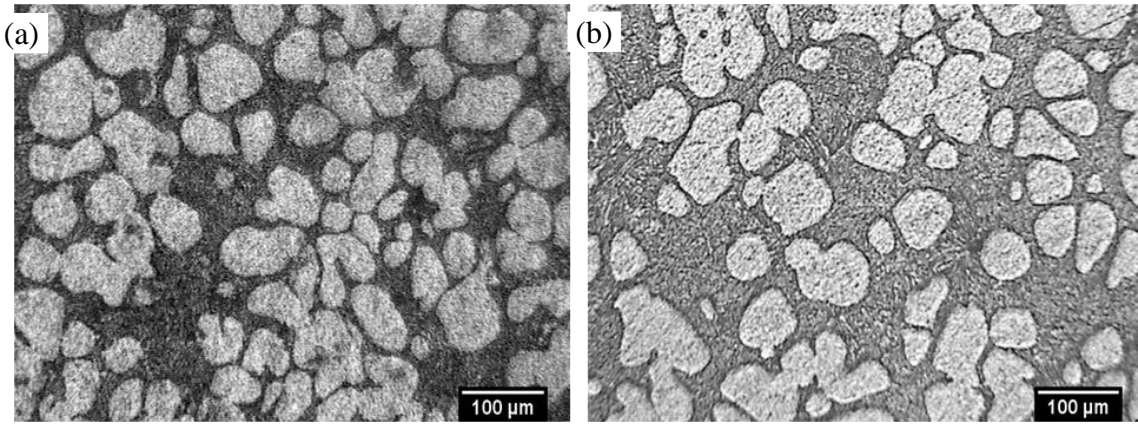


Fig. 4.6 Effect of stirring speed on average grain size and shape factor of primary  $\alpha$ -Al phase.

Figure 4.7(a-b) shows the microstructures for A356 alloy processed without and with baffle. The figures displayed that the sample with baffles exhibited fine (average grain size about 68μm) and more globular primary  $\alpha$ -Al phase (shape factor 0.85) than the sample without baffle (average grain size 76 μm and shape factor about 0.80). This is a consequence of the modified flow pattern, which forced the melt to accelerate near the crucible walls and thereby produced a refined and more spherical structure. The sample without baffle comprises porosity volume fraction of 1.23%, while the sample with baffle has 0.81% porosity volume fraction.



**Fig. 4.7 Microstructures of rheometal processed A356 alloy (a) without and (b) with baffle stirred at 1000rpm.**

While rotating EEM is immersed in melt; swirling motion takes place. EEM is cold with respect to rest of the melt. Due to enthalpy exchange, the EEM starts dissolving. Although during stirring melt also comes in contact with crucible wall at the periphery. However, in the vicinity of EEM, the melt will experience cooling. This gives rise to the nuclei formation around the EEM which are thrown apart by centrifugal force. Meanwhile fresh melt comes in contact with EEM and more nuclei forms around EEM. These nuclei subsequently grow and assume more or less spherical shape. Within 30 sec the entire EEM dissolves in melt and semi-solid mass of desired percentage form [101-102].

The formation of non-dendritic structure at different stirring speed is observed. This is in accordance with earlier findings by Fan et al. [103]. Based on their observations as the stirring speed and intensity of turbulence increased, the variations from dendrites to spheres via rosettes due to the change in the diffusion geometry in the liquid around the growing solid phase takes place.

Figure 4.8(a-f) illustrates the effect of stirring speed on the morphology of eutectic silicon. Figure 4.8(a) exhibits long and coarser silicon needles for as-cast A356 alloy.



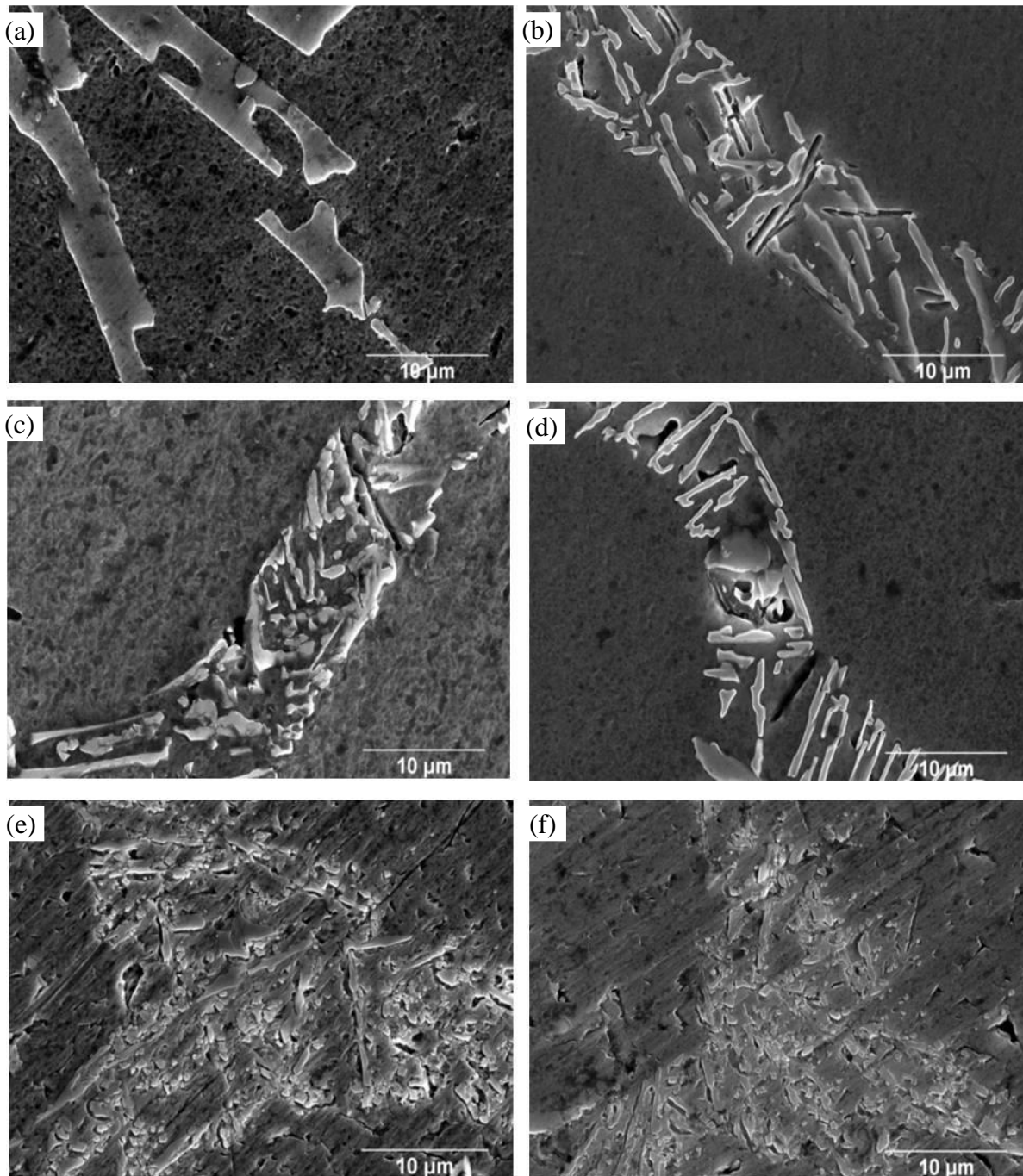


**Fig. 4.8** Effect of stirring speed on morphology of eutectic silicon for (a) as-cast (b) 400, (c) 600, (d) 800, (e) 1000 and (f) 1200rpm at 30% solid fraction and 0min holding time.

Figure 4.8(b-f) shows that shearing restricted the growth of Si needles. Hence, the refined solidification structure leaving the eutectic silicon less space to grow and the Si needles become shorter and finer.

The process of grain refinement at higher stirring speed can be clarified based on copious nucleation theory. In conventional casting method, heterogeneous nucleation occurs at the mold



wall and most of the nuclei move into the hot section and is melted either while the melt is stirred or due to gravity induced melt flows (which is not important for Al-Si alloys, since the density difference between the Al alloy and the pure Al phase is small). Because of this only a small fraction of nuclei survives and participates in final microstructure.

In conventional casting process nucleation occurs at crucible walls. The nuclei are oriented arbitrarily with respect to the heat flow, being normal to the crucible wall. The growth velocity of nuclei depends on its orientation with respect to the heat flow. Those nuclei, which are favorable, oriented to the heat flow direction, survive and a columnar front establishes. The release of latent heat in front of this columnar front leads to an increase in temperature in the center of a crucible till liquidus is reached. Due to three kind of structures (thin shell of fine grains, columnar zone and coarser inner zone), thick castings in a mold have an anisotropic structure and properties. While in thin casting, most often only the columnar zones are observed.

The shearing action of the liquid leads to a uniform temperature of the liquid. Due to stirring under shear force, heterogeneous nucleation in the whole liquid takes place. Because of this each nuclei survives and participates in the formation of uniform microstructures [103]. So based on above discussion it is cleared that for lower stirring speed, the sites for heterogeneous nucleation are less when compared to the nucleation sites for high stirring speed. The presence of more number of nucleating sites leads to the grain refinement of  $\alpha$ -Al phase at high stirring speed.

### **4.3 XRD Analysis**

XRD analysis for as-cast A356 and stirred at 1000 rpm is shown in Fig.4.9. The diffractogram reveals that  $\alpha$ -Al and eutectic Si phases are observed. For rheometal sample a small left shift (0.26) of  $\theta$  peak for both  $\alpha$ -Al and eutectic Si seen as compared to the as-cast sample. Due to quenching, the solubility of Si may increase in Al and hence more Si may be retained in the Al lattice which altered the lattice parameters. This is the reason why the peak shifted.

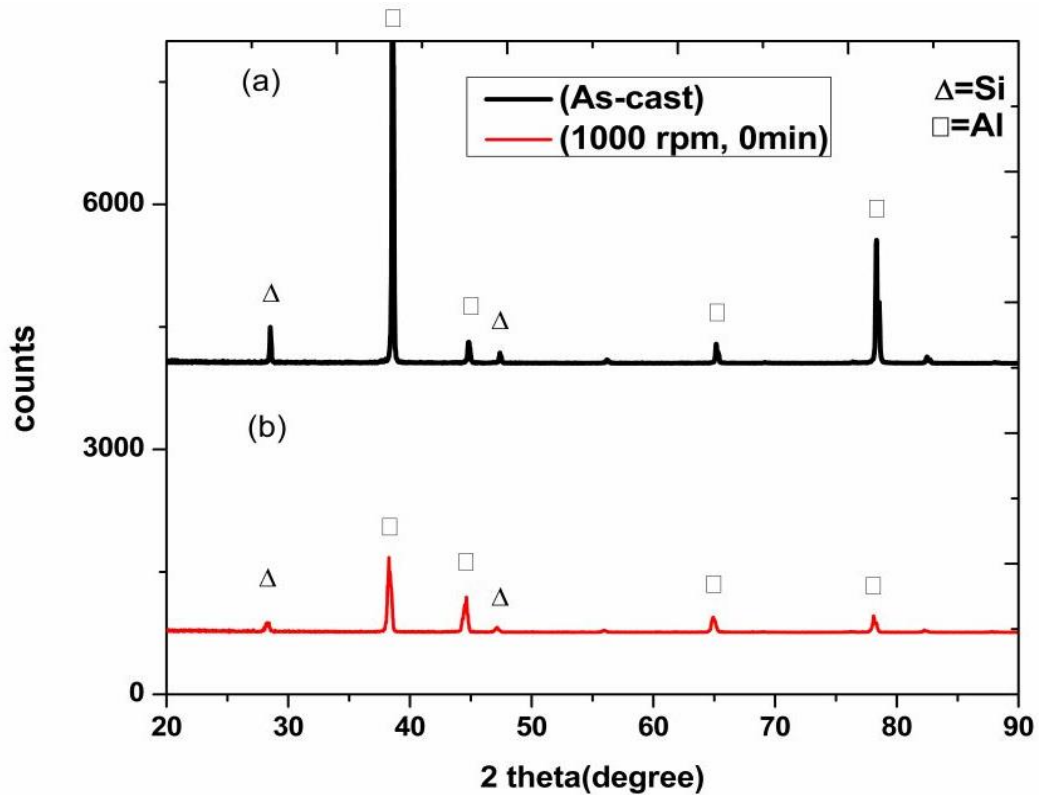


Fig. 4.9 XRD analysis for (a) as-cast and (b) 1000 rpm, 0min in A356 alloy.

#### 4.4 Thermal Analysis

Figure 4.10 shows thermal analysis for cooling of two selected samples (as-cast and stirred at 1000rpm). Both samples exhibited similar behavior. In thermal analysis different peaks are, peak 1 = correspond to eutectic temperature, peak 2 = correspond to liquidus temperature.

The temperatures for exothermic reaction thus evaluated in the as-cast condition from Fig.4.10 (Table 4.1) are  $T_{\text{eutectic}}=563^{\circ}\text{C}$ ,  $T_{\text{liquidus}}= 605^{\circ}\text{C}$  and temperatures for rheometal processed sample from Fig.4.10 are  $T_{\text{eutectic}} = 561^{\circ}\text{C}$ ,  $T_{\text{liquidus}}= 603^{\circ}\text{C}$ .

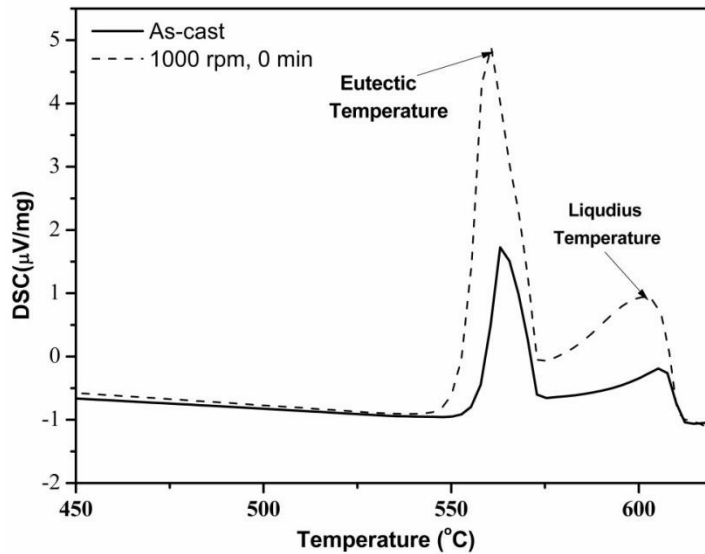


Fig. 4.10 DSC analysis for as-cast and 1000 rpm, 0min in A356 alloy.

**Table.4.1: Data obtained from DSC curve**

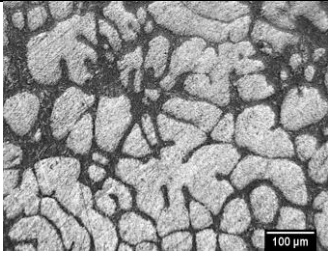
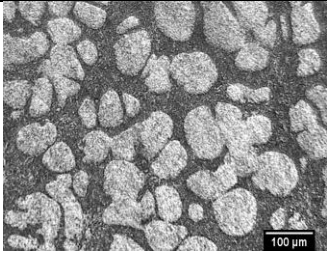
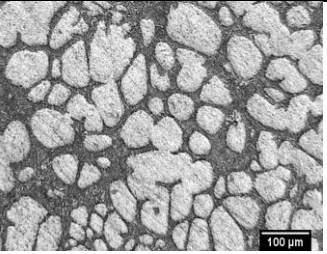
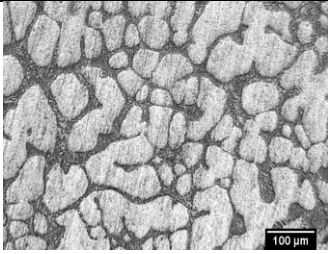
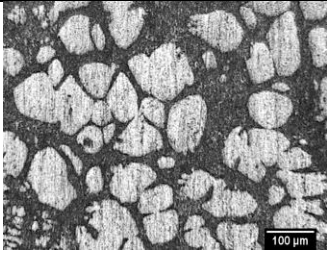
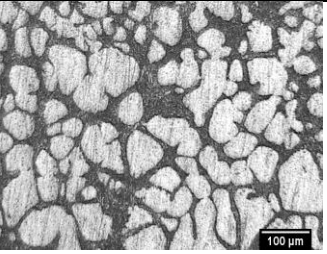
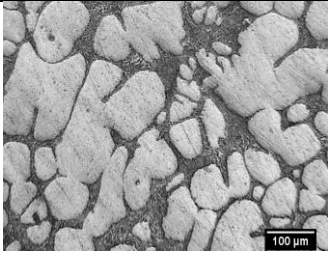
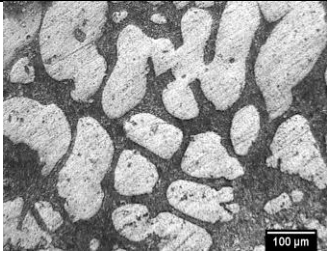
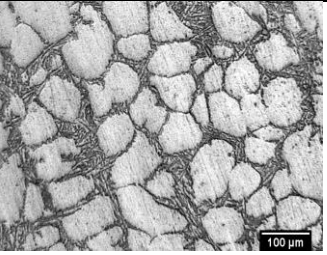
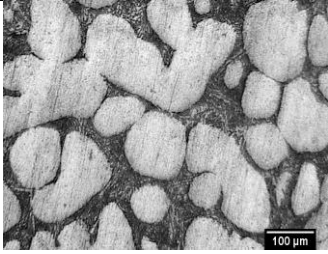
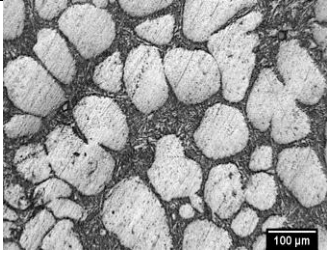
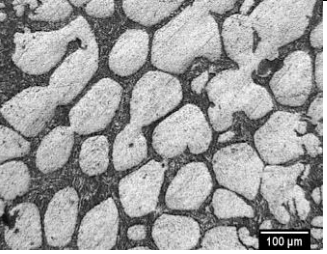
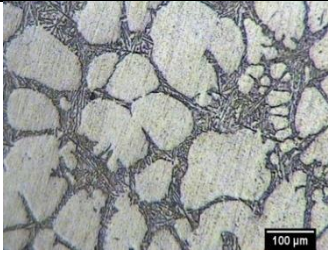
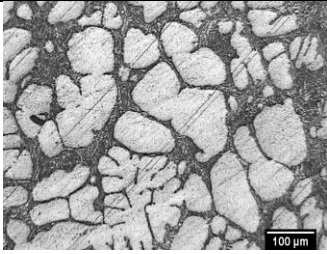
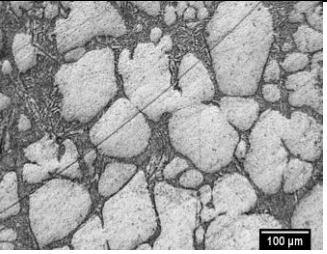
Sample	Exothermic reaction	
	Eutectic Temp ( $^{\circ}\text{C}$ )	Liquidus Temp ( $^{\circ}\text{C}$ )
As-cast	563	605
1000rpm, 0min	561	603

Ardakan et al. [104] studied the rheocasting process of hyper-eutectic Al-Si alloys with different Mg content at a rotation speed of 250 rpm. Their observation showed that reduction in the eutectic temperature led to modification of eutectic Si. Nafisi et al. [105] studied the effect of modifier in the conventional cast and semi-solid cast A356 alloy. Their observation showed that additions of modifier in the melt shifted the eutectic temperature to lower temperature, which directed modification in the morphology of eutectic Si.

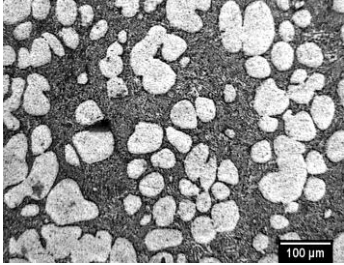
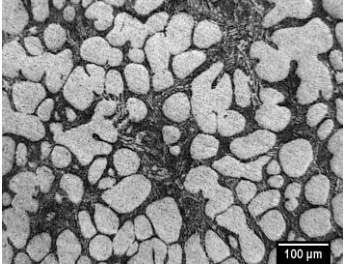
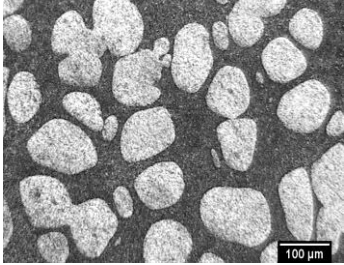
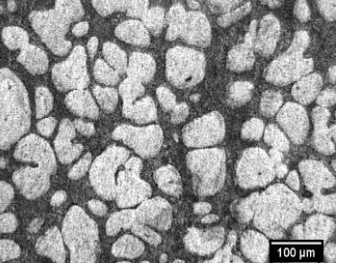
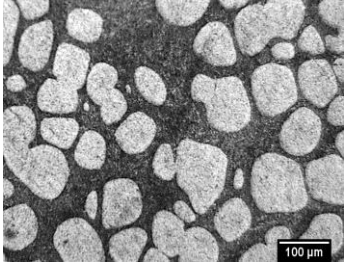
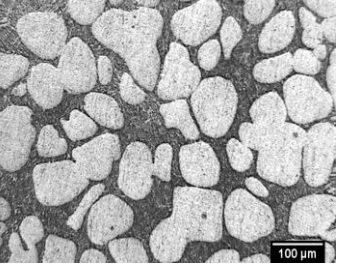
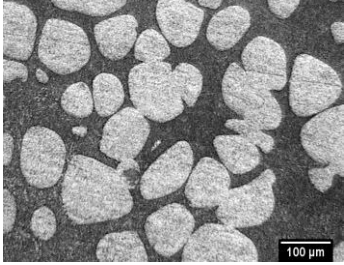
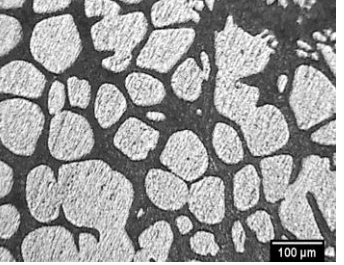
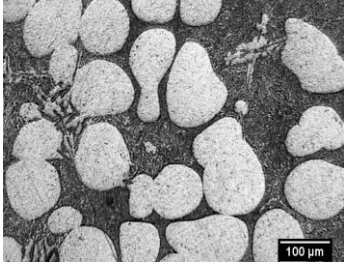
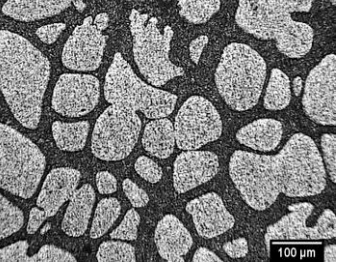
The above findings showed that as modifier leads to modification of Si morphology by reducing the eutectic temperature, stirring exhibited similar effect without addition of modifier. Stirring of a melt using EEM lowers the eutectic temperature. This behavior can be understood by the DSC data provided in table 4.1.

#### **4.5 Coarsening Kinetics: Without Baffles**

Coarsening is a diffusive-competitive multi-particle growth problem. The curvature of particles controls the diffusion of solute and thus the dissolution and growth kinetics of the particles. When the matrix has precipitates of various sizes, this drives the solute transport from small to large precipitates. This is due to Gibbs-Thomson effect in which the solubility of a particle is directly proportional to its curvature [106]. Figure 4.11 shows the microstructures for the A356 alloy in the semi-solid state. Dendrites in as-cast condition changed into globular morphology when the alloy slurry was stirred at various stirring speeds.

Time (min)	Stirring speed (rpm) (a)		
	400	600	800
0			
3			
5			
10			
15			

**Fig. 4.11 (a) Microstructure of RSF processed A356 alloy at different rpm (400, 600 and 800) with different holding times.**

Time (min.)	Stirring speed (rpm) (b)	
	1000	1200
0		
3		
5		
10		
15		

**Fig. 4.11 (b) Microstructure of RSF processed A356 alloy at different rpm (1000-1200) with different holding times.**



The average grain sizes for all quenched samples at different stirring speed and holding times are shown in Fig. 4.12.

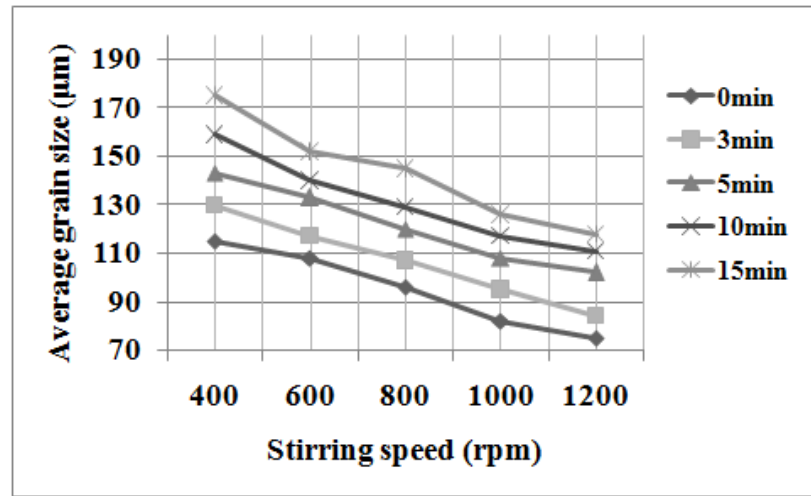


Fig. 4.12 Variation of average grain size in A356 alloy with stirring speed and holding time.

Result reveals that as holding time increased the average grain size of  $\alpha$ -Al phase increased which showed the agreement with the trend of Lifshitz, Slyozov and Wagner (LSW) theory [107]. Various mechanisms to explain microstructure evolution during coarsening are as given below:

(a) **Diffusive- LSW theory**

In the current section, an attempt is made to find out the average grain size of primary  $\alpha$ -Al phase at different holding times using diffusive Ostwald ripening. Ostwald ripening reduces the total interfacial energy [108]. On isothermal holding the microstructure evolution by coarsening and diffusion from high curvature interface to lower curvature interface occurs [109]. The equation for the average grain size is

$$D_M^3 - D_0^3 = K_{fs} K_{LSW} (t - t_0) \quad (4.1)$$

Where  $D_M$  = average radius of the particles after time  $t$ ,  $D_0$  = initial average radius at time  $t_0$ ,  $K_{fs}$  = solid fraction coefficient and  $K_{LSW}$  = growth constant for pure diffusive mass transports [110] and expressed as:

$$K_{LSW} = \frac{8\Gamma dT_0}{9m_L(C_S - C_L)} \quad (4.2)$$

Where,  $C_S$  and  $C_L$  are the solute concentration in the solid and liquid phase respectively,  $m_L =$  slope of the liquids line,  $d =$  solute diffusion coefficient in liquid,  $T_0 =$  temperature at  $t_0$  and  $\Gamma =$  capillary constant expressed as:

$$\Gamma = \frac{V_m \gamma}{\Delta H_f} \quad (4.3)$$

Where,  $V_m =$  molar volume,  $\gamma =$  solid/liquid interfacial energy and  $\Delta H_f =$  heat of fusion of the alloy. The rate constant depends on the fraction solid. This effect is accounted in equation (46) by introducing the factor  $K(f_s)$

$$K(f_s) = 1 + 3.78\sqrt{f_s} - 6.5f_s^2 + 21.79f_s^3 \quad (4.4)$$

The theoretical value of coarsening rate constant  $K_{calc} (= K(f_s) \times K_{LSW})$  in equation (47) is calculated by using the given parameters [111] in appendix 4.  $K_{calc}$  for current investigation is about  $0.551 \mu\text{m}^3/\text{s}$ . The detailed calculations for  $K_{calc}$  are provided in appendix 5. The experimental values of  $K$  obtained from Fig. 4.13 vary in the range of 949 to  $4678 \mu\text{m}^3/\text{s}$ , (table 4.2) which are much higher than the calculated one.

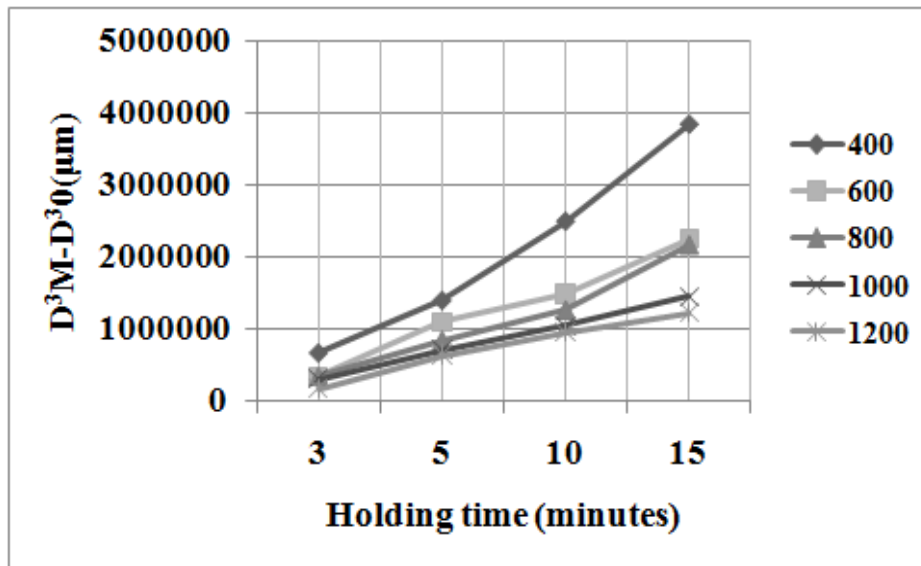


Fig. 4.13 Variation of cube of mean particle size with holding time.



**Table.4.2: Experimental value of coarsening rate constant (K)**

Stirring speed (rpm)	Holding time (min)			
	3	5	10	15
400	3756	4678	4165	4265
600	1899	3643	2474	2502
800	1891	2810	2103	2404
1000	1700	2361	1750	1610
1200	949	2131	1576	1356

Other investigators [112-114] have observed higher coarsening rate in semi-solid processing experiment. Jain et al. [112] in RSF process for 15% solid fraction obtained an experimental value of the coarsening rate constant about  $322 \mu\text{m}^3/\text{s}$ . Kaufmann et al. [113] observed a coarsening rate 166 and  $430 \mu\text{m}^3/\text{s}$  for new rheocasting and conventional thixocasting process respectively. Zoqui et al. [114] investigated electromagnetic stirring rheocasting process and acquired coarsening rate constant about 1043 and  $3099 \mu\text{m}^3/\text{s}$ . Therefore, the competitive growth of particles related to diffusive Ostwald ripening can-not be the only coarsening mechanism. Other phenomena like convective coarsening and coalescence may contribute for coarsening in the average grain size of primary  $\alpha$ -Al phase.

#### (b) Coarsening due to convective mass flow

A theory for coarsening due to convective mass flow can be given as

$$D^2 - D_0^2 = AK_{LSW} \frac{(1-f_s)^{2/3}}{f_s} \omega^{1/3} t \quad (4.5)$$

Where  $\omega$ = rotation frequency, A= constant including the diffusion coefficient,  $f_s$ = solid fraction, t=time [115]. From the above equation, it is cleared that grain size depends on the square root of time.

The comparison between the theoretically and experimental value of coarsening rate constant  $K$  has also been carried out. The theoretical value of  $K$  can found using the parameters [111] in appendix 4. The detailed calculations for  $K_{\text{calc}}$  are given in appendix 6. The average calculated

value of coarsening rate constant due to convective mass flow  $K_{cal}$  for present investigation is about  $\sim 3408 \mu\text{m}^2/\text{sec}$ , and experimental values obtained from Fig. 4.14 varied in the range 8 to  $24 \mu\text{m}^2/\text{sec}$  (table 4.3). So it is cleared that  $K_{cal}$  is much higher than  $K_{exper}$ , which is just reverse of diffusive-LSW theory.

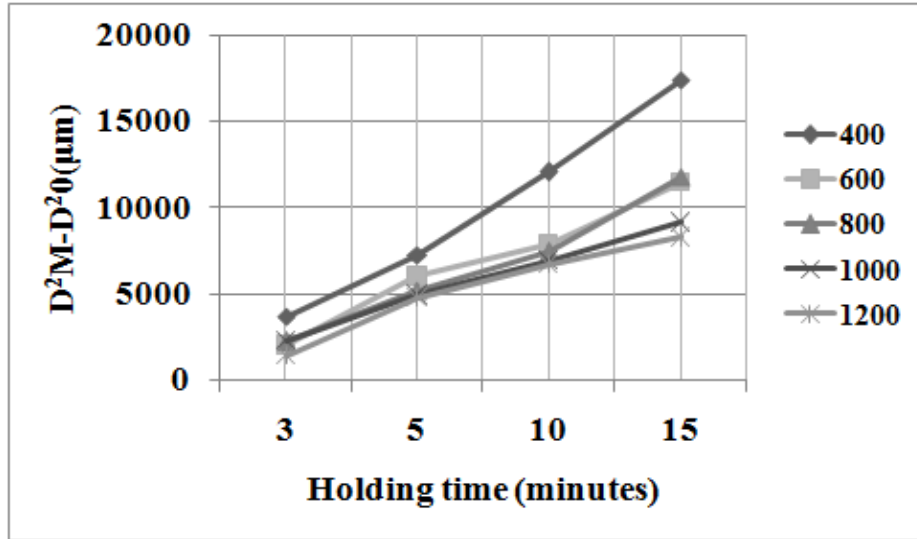


Fig. 4.14. Variation of square of mean particle size with holding time.

Table.4.3: Experimental value of coarsening rate constant due to convective mass flow

Stirring speed (rpm)	Holding time (min)			
	3	5	10	15
400	20	24	20	19
600	13	20	13	13
800	12	17	12	13
1000	11	16	11	10
1200	8	15	11	9

### (c) Analysis of coalescence by shear flow

Since coarsening due to diffusive-LSW theory and convective mass flow are unable to describe the morphological changes for rheometal processed alloys, coalescence phenomena might be considered too. Due to stirring, the shearing motion can lead to coalescence of fragmented and partially melted dendrites in the melt. Hence, coalescence forms the aggregates of large particle

size. Independent of the type of fluid flow (laminar or turbulent) such aggregates owing to velocity gradients in the melt, moved at different speeds and on passing may collide or aggregate. However, pure collisions can-not explain the morphological changes. Takajo et al. [116] proposed a model of concurrent diffusive Ostwald ripening and collisions of particles in liquid phase sintering of Cu-Co alloys. Theoretical observations showed that combination of Ostwald ripening and coalescence with size independent collision rate leads to Ostwald ripening law (cube root growth of the average particle size), but the rate of coarsening kinetics depends on the collision rate (which would be proportional to stirring frequency). This model described just opposite of what is observed: high stirring frequency leads to smaller coarsening rate constant [Fig.4.13 and Fig.4.14].

Therefore, aggregation and coalescence phenomenon, as well as pure diffusive Ostwald ripening or convective-diffusive Ostwald ripening alone and a combination of Ostwald ripening and coalescence can-not describe the change in morphology of primary  $\alpha$ -Al phase (as in Fig.4.13 and Fig.4.14). Before proceeding let us summarize the major experimental findings:

- (i) The average grain size of primary  $\alpha$ -Al phase decreases as the stirring speed increases for all isothermal holding times.
- (ii) The average grain size of primary  $\alpha$ -Al phase increases with holding time, but the rate of coarsening kinetics decreases as stirring speed increases.

However, the basic idea of Takajo et al. [116] approach seems to be correct. The morphological changes occurred as a result of mechanisms acting concurrently: during shear flow aggregation process occurred and aggregates performed Ostwald ripening by diffusion. However, Ostwald ripening did not take place between the particles (distributed in the melt) but along the surface of the aggregates. This means the aggregates worked as entities with different curvatures, including convex and concave ones (at the neck of coalescence) and these curvatures difference, drive a diffusion current such that, the aggregates formed by shear collisions, round while stirred and hold isothermally. This was quite similar to liquid phase sintering (without stirring of course). The shear flows around the aggregates (which also rotate) enhanced mass transport in diffusion boundary layer attached to them.

Another possibility that cannot be ruled out during experiments is de-agglomeration processes. If agglomeration occurred then it might be possible that during isothermal holding necks melt-

back and thus particles became free from an aggregate and may disperse in the matrix. This de-agglomeration would be enhanced as stirring speed increased (enhanced solute transport).

There was another possibility leading to enhanced coarsening rate constants. Shearing and stirring induce turbulence flows, which was complicated by the existence of particles dispersed in the fluid matrix. Generally in turbulent flow mass transport is not describable by classical diffusion. However, the presence of turbulent eddies has to be taken into account, flow is escorted with so-called turbulent diffusion [98]. Turbulent diffusion is much faster than molecular diffusion. The random motion of the fluid is responsible for mixing, with a so-called eddy diffusion coefficient. The eddy diffusion coefficient depends on properties of fluid flow and fluid velocity [96]. A rough estimate leads to the following relation. The Schmidt number relates kinematic viscosity  $\nu$  to molecular diffusion ( $D$ ) as  $S_c = \nu/D$ . The turbulent kinematic viscosity can be expressed as  $\nu_{\text{turb}} \sim \nu \text{Re}/\text{Re}_{\text{crit}}$ , where  $\text{Re} =$  Reynolds number and  $\text{Re}_{\text{crit}}$  the critical Reynolds number. Assuming that for turbulent diffusion a Schmidt type relation is valid then  $D_{\text{turb}} \sim D \text{Re}/\text{Re}_{\text{crit}}$ . The critical Reynolds number for flow through a packed bed around is 2000 and for a stirred vessel around is 10000 [117]. The Reynolds number varies in the range of 16000 to 48000 when stirring speed varies from 400 to 1200 rpm. Thus ratios ( $\text{Re}/\text{Re}_{\text{crit}} \approx 1.6$  to 4.8), between stirred vessel and packed bed around is 8 to 24. Thus the turbulent diffusion is enhanced by the Reynolds number by a factor of 5 to 10 when compared to molecular diffusion. This estimate showed that observed large coarsening rate could just be due to enhanced mass transport by turbulent diffusion.

#### 4.6 Coarsening Kinetics: With Baffles

The micrographs show in Fig.4.11 revealed that stirring speed of 1000 rpm is found optimum regarding average grain size and shape factor. Therefore, experiments for coarsening kinetics with the use of baffle were performed at 1000 rpm stirring speed. Figure 4.15 shows the microstructures of the A356 alloy without and with baffle sheared at 1000 rpm with different holding time.

Time (min)	Stirring speed (1000rpm)	
	Without Baffle	With Baffle

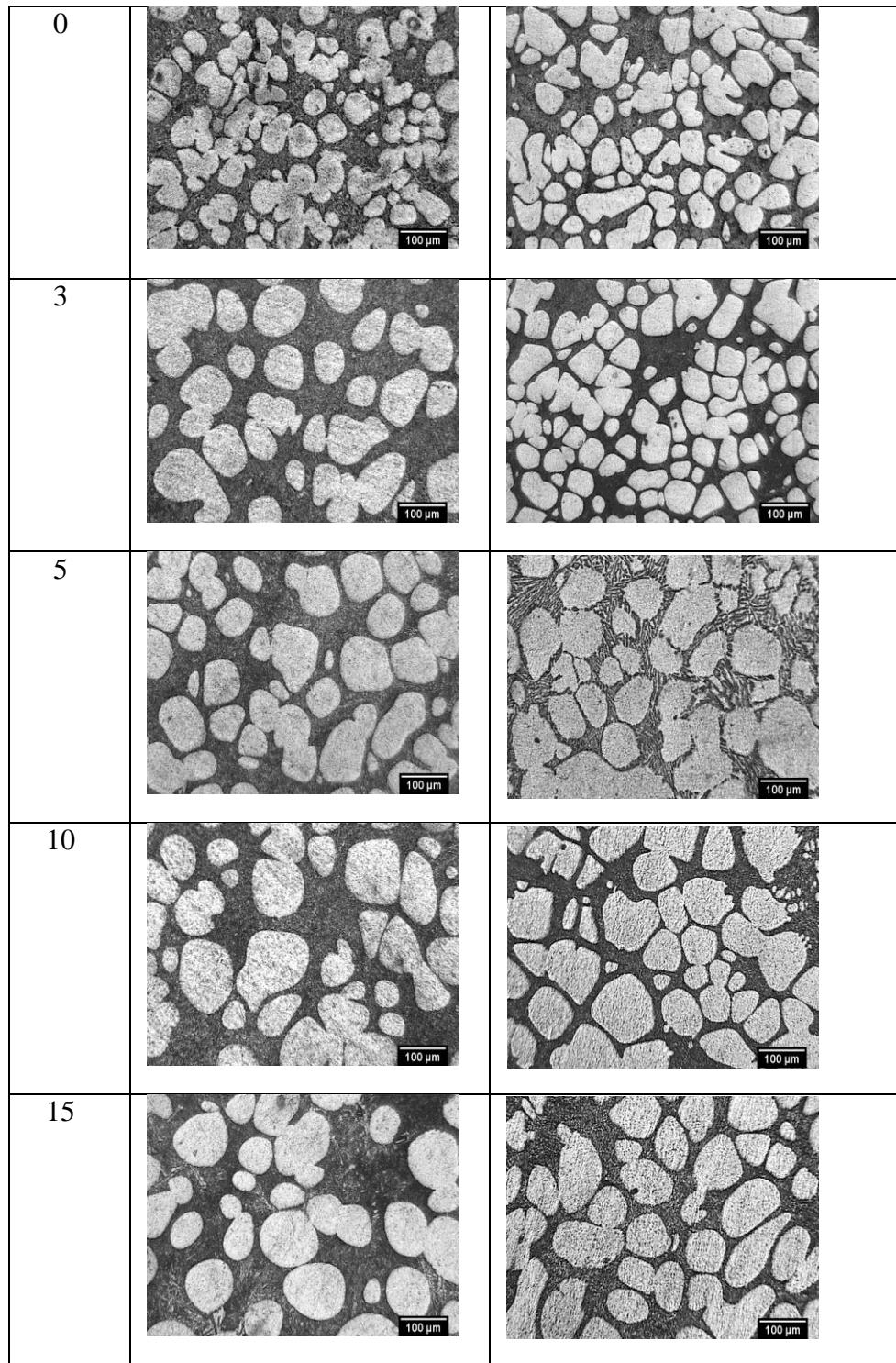
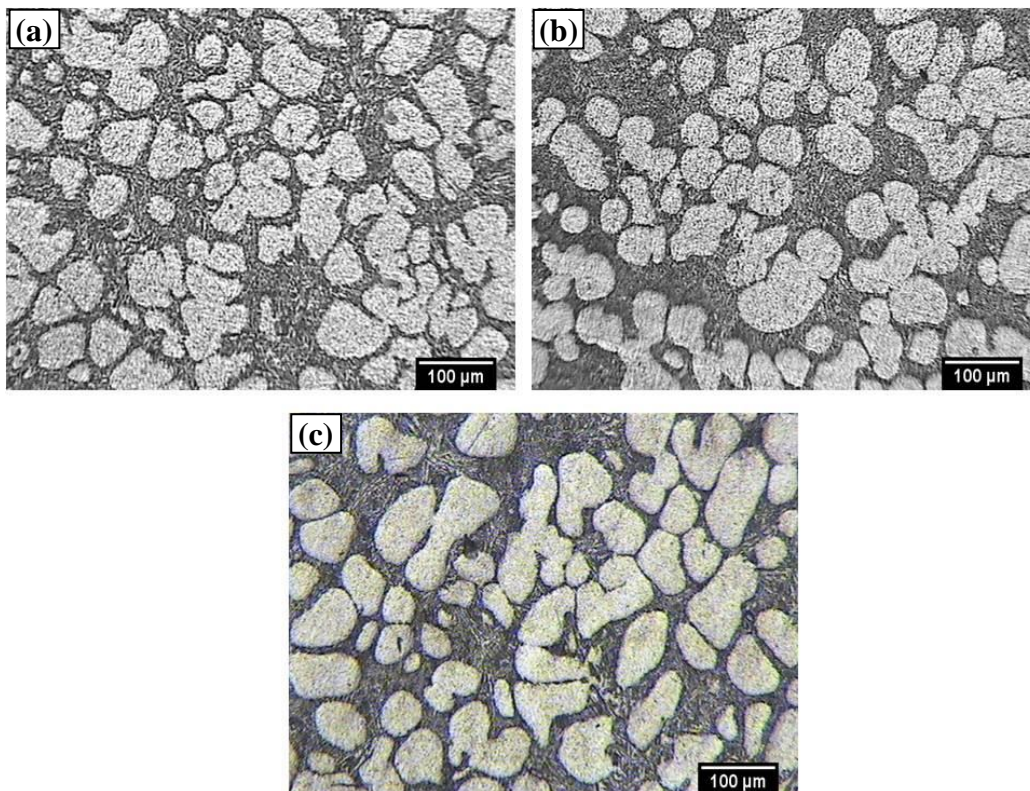


**Fig. 4.15 Microstructure of RSF processed A356 alloy (a) without and (b) with baffle stirred at 1000 rpm with different holding times.**

The microstructures with baffle exhibits similar trend of coarsening kinetics as shown in Fig.4.11. From microstructures observations, it is clear that samples with baffle at different holding time comprise fine and more globular  $\alpha$ -Al phase compared with samples prepared without baffle. This change is due to the melt to accelerating along the crucible wall and producing a fine and more spherical structure.

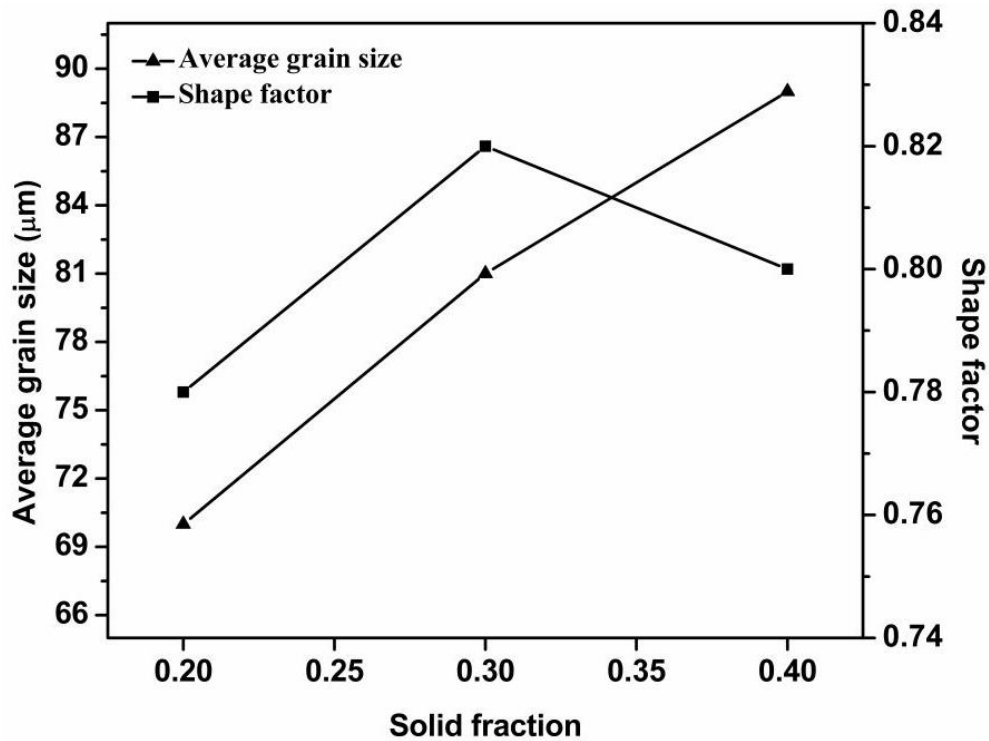
#### 4.7 Effect of Solid Fraction

Figure 4.16 represents the microstructure of A356 alloy stirred at 1000 rpm with solid fraction of 20, 30 and 40wt.%.



**Fig. 4.16 Microstructure of RSF processed alloys at (a) 20, (b) 30 and (c) 40wt.% solid fraction for 1000rpm, 0min.**

Figure 4.17 demonstrates the effect of the solid fraction on average grain size and shape factor for  $\alpha$ -Al.



**Fig. 4.17 Effect of solid fraction on average grain size and shape factor of primary  $\alpha$ -Al particles.**

From Fig.4.16 and Fig.4.17 it is evident that the average grain size of  $\alpha$ -Al phase continuously increases. The average grain size of  $\alpha$ -Al phase is 70  $\mu\text{m}$  for 20 wt.% solid fraction which increases upto 89  $\mu\text{m}$  for 40 wt.% solid fraction. Higher solid fraction led to coarsening by coalescence owing to increased particle collisions. However shape factor, upto 30wt.% solid fraction continuously increases, afterward further increment in solid fraction led to deviation in shape factor. Shape factor 0.82 showed the best globularity of semi-solid slurry at 30 wt.% solid fractions. So 30 wt.% solid fraction found to be optimum regarding average grain size and shape factor.

Figure 4.18 (a-c) shows the effect of the solid fraction on the morphology of eutectic Si. The observations reveals that in Fig. 4.18 (a-b) Si needles are small in size as compared to Si needles as shown in Fig. 4.18 (c). This is attributed to the fact that higher solid fraction led to the formation of large Si needles which is associated with agglomeration and sintering of these pieces to form large clusters.

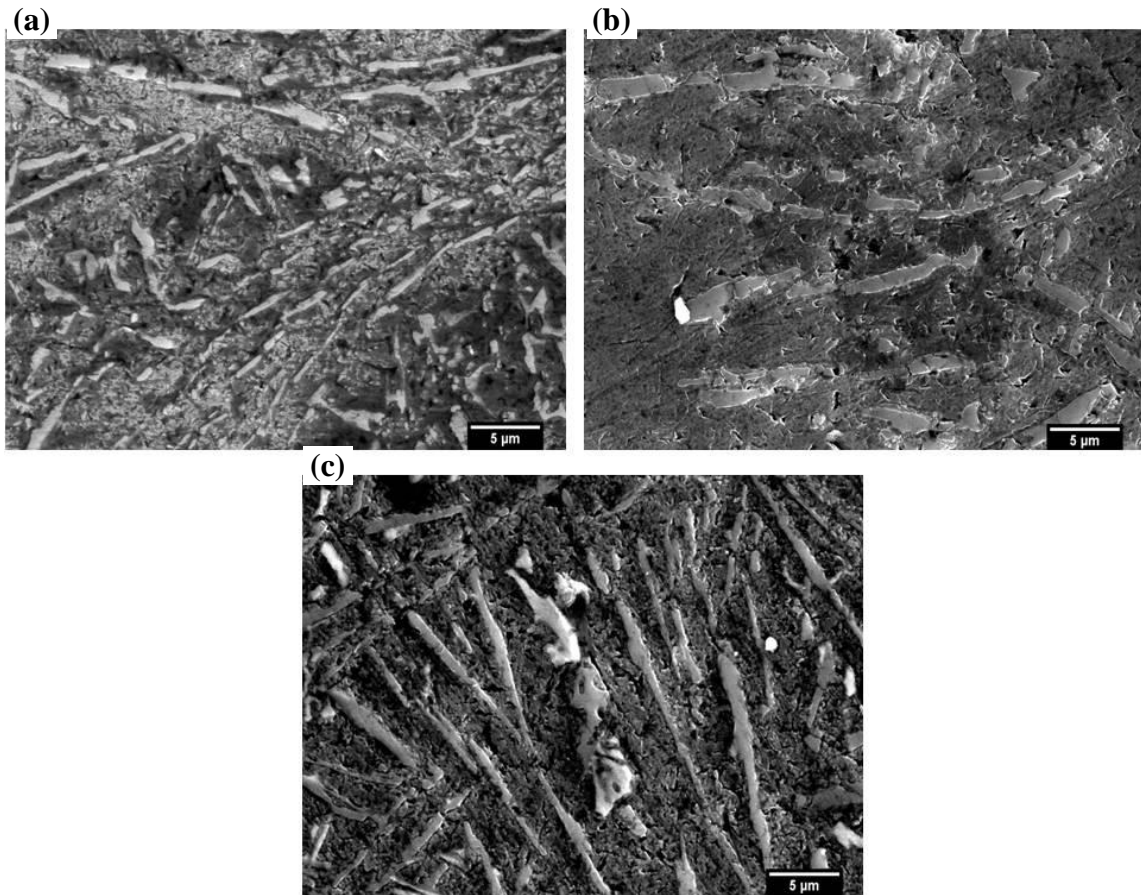


**Fig. 4.18** Effect of solid fraction (a) 20, (b) 30 and (c) 40 wt.% on Si morphology.

#### **4.8 SEM Analysis of Al-5Ti-1B Master Alloy**

Figure 4.19 represents the SEM micrograph of Al-5Ti-1B master alloy with X-ray mapping. From micrograph, it is cleared that master alloy exhibited the blocks of  $TiAl_3$  particles and homogeneous distribution of  $TiB_2$  particles linked within the matrix of Al.



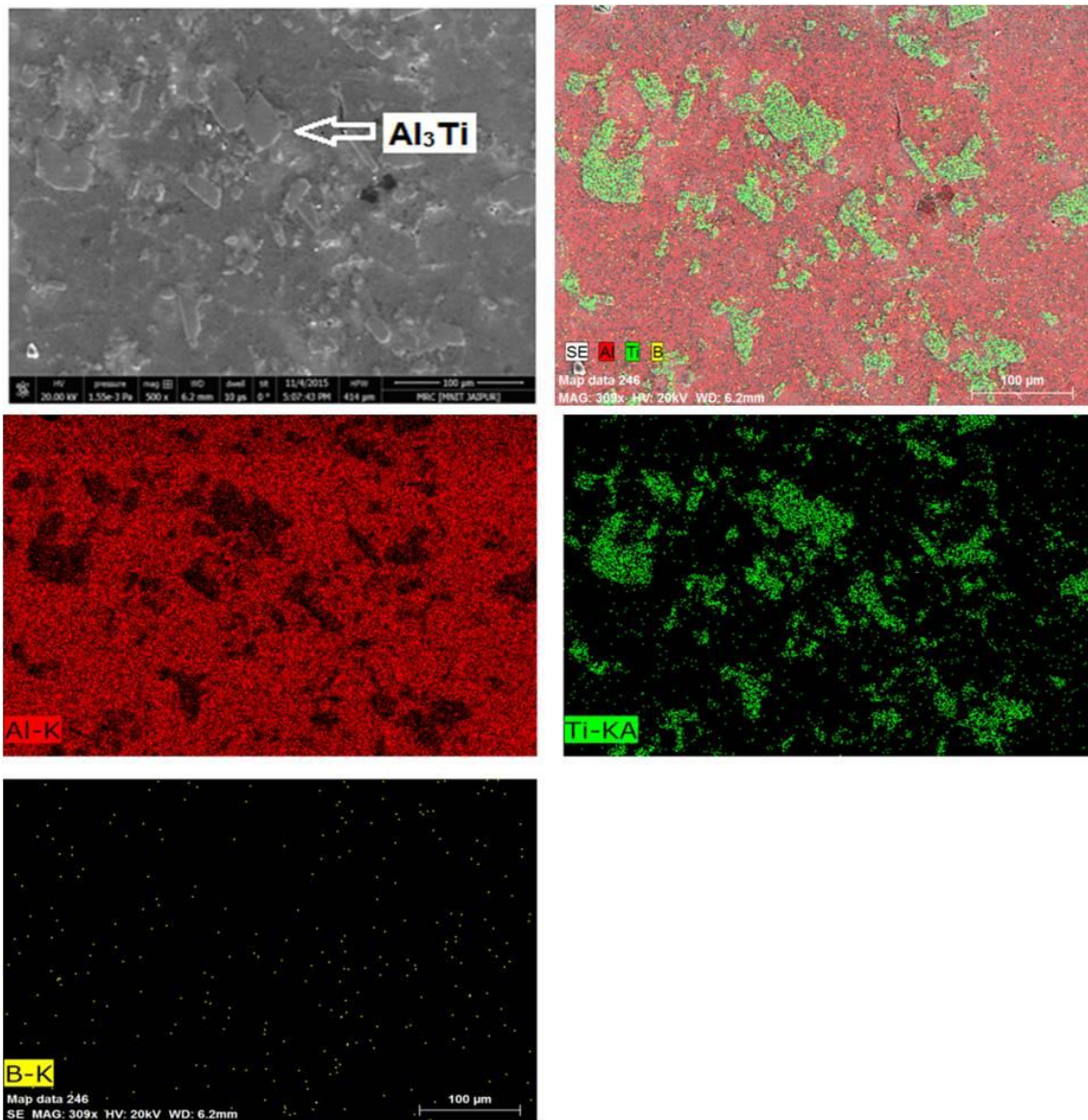
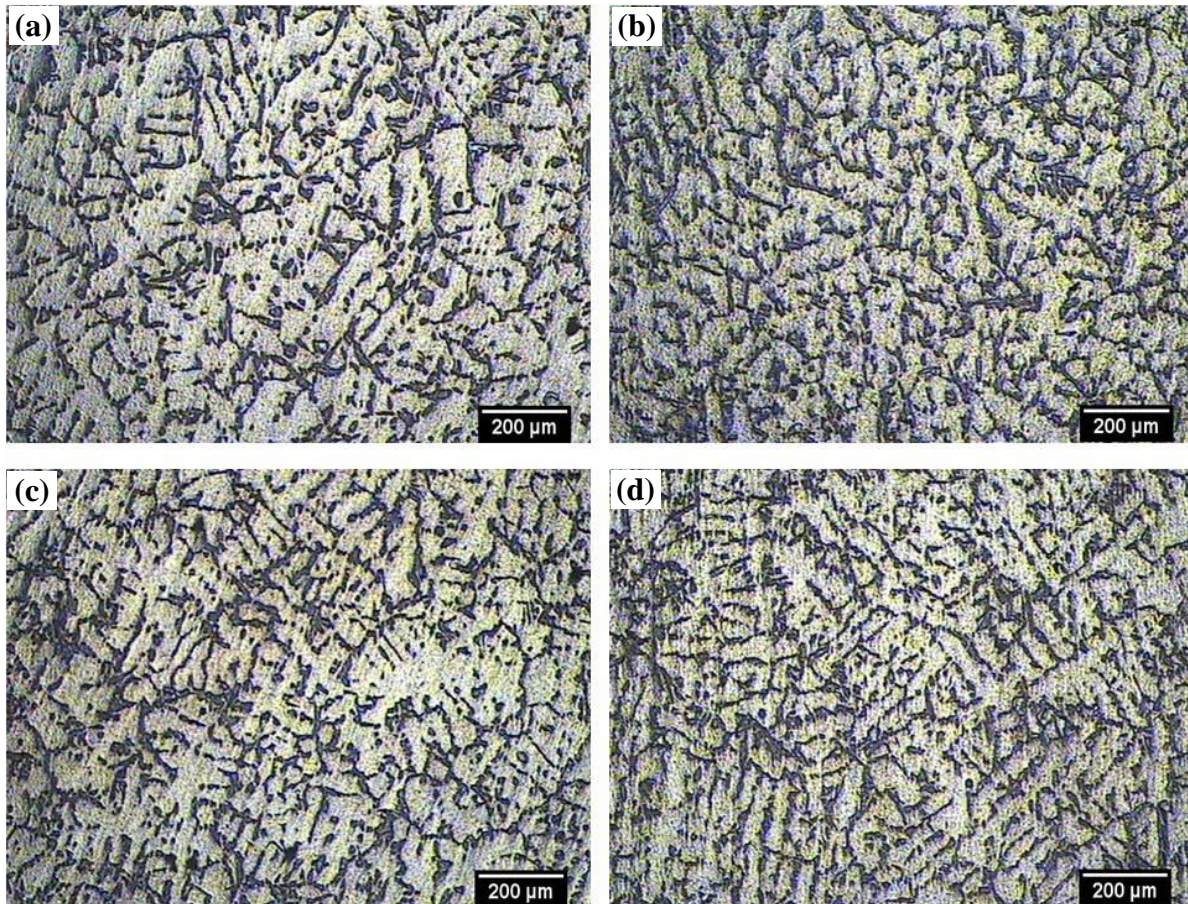


Fig. 4.19 SEM micrographs of Al-5Ti-1B master alloy with X-ray mapping.

#### 4.9 Effect of Grain Refiner in Conventional Cast A356 Alloy

Figure 4.20 shows the optical micrographs for varying content of Al-5Ti-1B grain refiner in conventional cast A356 alloy.



**Fig. 4.20** Microstructures of A356 alloy with varying content (a) 0.2, (b) 0.4, (c) 0.6 and (d) 0.8 wt.% grain refiner.

The addition of grain refiner to melt released nucleating sites which suppressed the formation of dendritic morphology [118]. Figure 4.21 shows that SDAS reduced continuously upto 0.6 wt.% grain refiner, afterwards SDAS value increases. Since 0.8wt.% grain refiner shows an increment in SDAS value. Hence, 0.6 wt.% grain refiner seems to be optimum and this optimum level of grain refiner was further used to observe the effect of grain refiner on the morphology  $\alpha$ -Al in the semi-solid state.



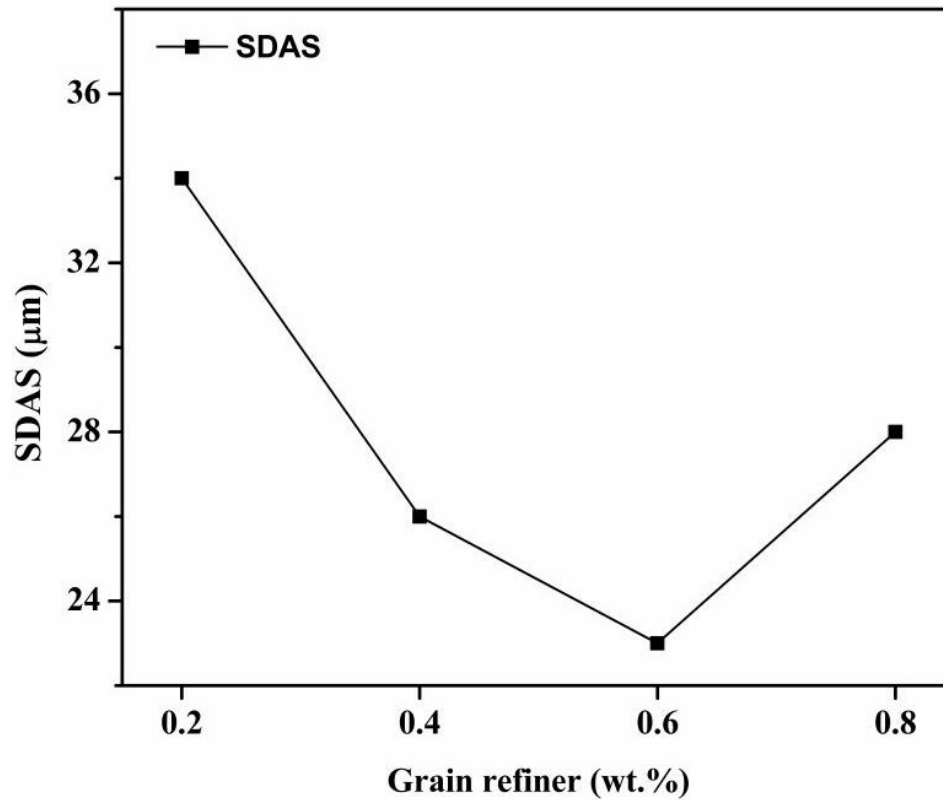


**Fig. 4.21 Effect of grain refiner on SDAS of A356 alloy.**

Similar findings, with different content of Al-5Ti-1B on the morphology of Al-Si alloy in conventional casting method, were observed by Murty et al. [27]. Their observations showed that 0.6 wt.% of Al-5Ti-1B gives the optimum grain refinement.

#### **4.10 Comparison of A356 Alloy in Different Processing Conditions**

##### **4.10.1 XRD analysis**

Figure 4.22 (a) shows the XRD pattern for Al-5Ti-1B master alloy. XRD pattern illustrated the presence of tetragonal  $\text{Al}_3\text{Ti}$ , hexagonal close packed (HCP)  $\text{TiB}_2$  and face-centered cubic (FCC)  $\alpha\text{-Al}$ . Figure 4.22 (b) to (d) exhibits the XRD analysis for without and with grain refined A356 alloy.

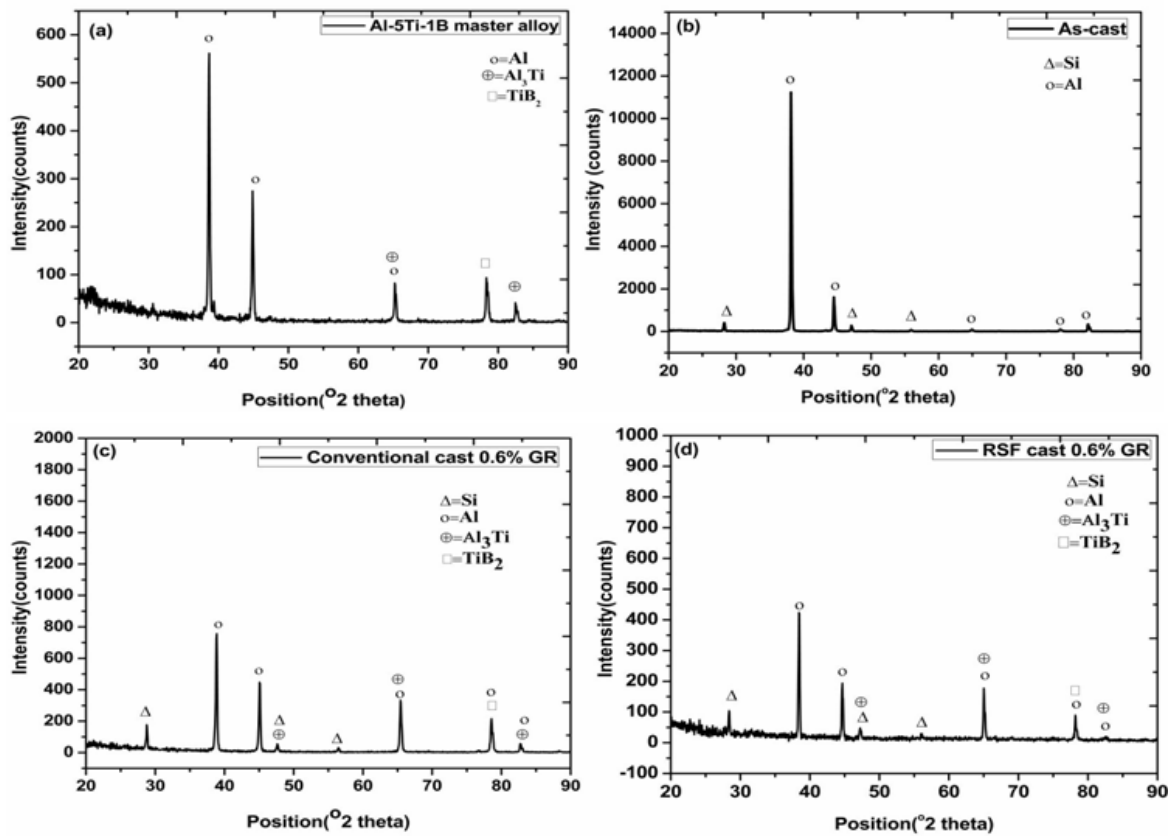


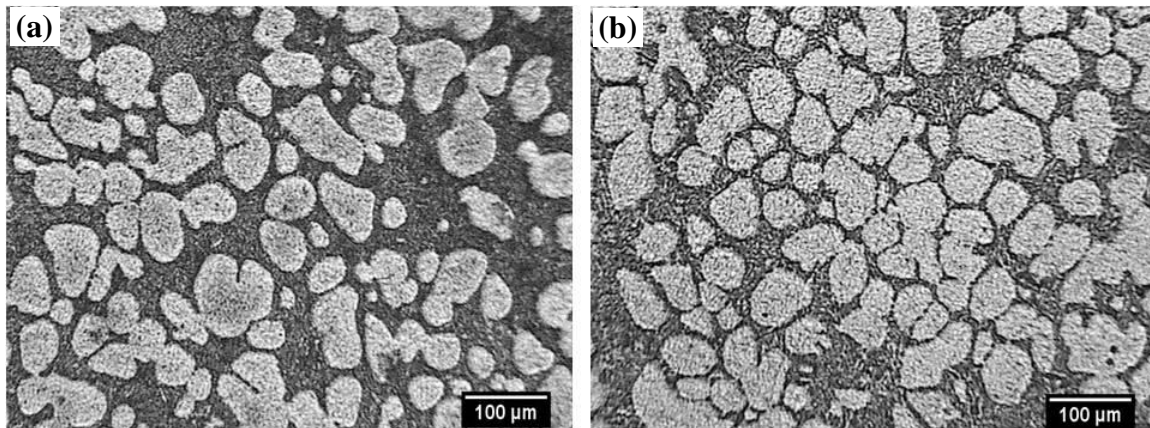
Fig. 4.22 XRD pattern for (a) Al-5Ti-1B master alloy, (b) as-cast, (c) conventional cast and (d) RSF cast A356 alloy.

Figure 4.22(b) reveals that as-cast A356 alloy exhibited  $\alpha$ -Al and Si phase. Figure 4.22(c-d) depicts XRD with 0.6% Al-5Ti-1B grain refiner for conventional cast and RSF cast A356 alloy respectively. The grain refined A356 alloy showed four phases namely  $\alpha$ -Al, eutectic Si,  $\text{Al}_3\text{Ti}$ , and  $\text{TiB}_2$  phases. These  $\text{Al}_3\text{Ti}$  phases provide the nucleating sites for heterogeneous nucleation and lead to the grain refinement for primary  $\alpha$ -Al phase [119-122].

#### 4.10.2 Microstructural observations

Variation in the morphology of  $\alpha$ -Al without and with grain refiner is shown in Fig. 4.23. The rheometal processed A356 alloy without grain refiner exhibits average grain size of  $\alpha$ -Al phase about 81  $\mu\text{m}$ , while the grain refined sample show average grain size of 68  $\mu\text{m}$ . So it is clear that addition of grain refiner to melt leads to further refinement of  $\alpha$ -Al as a bonus to already refined structure due to shearing. The addition of grain refiner increased the active nucleants in the melt and due to this nucleation of new grains takes place [123]. Because of these nucleating sites, globularity increased, but the growth of  $\alpha$ -Al particles decreases. The addition of Ti in

melt also restricted the grain growth and constitution super-cooling leads to the segregation of Ti at interface leading to refinement of  $\alpha$ -Al phase [124].



**Fig.**  
**4.23**

**Microstructures of RSF processed A356 alloy sheared at 1000 rpm for (a) without and (b) with 0.6% Al-5Ti-1B grain refiner.**

## CHAPTER 5

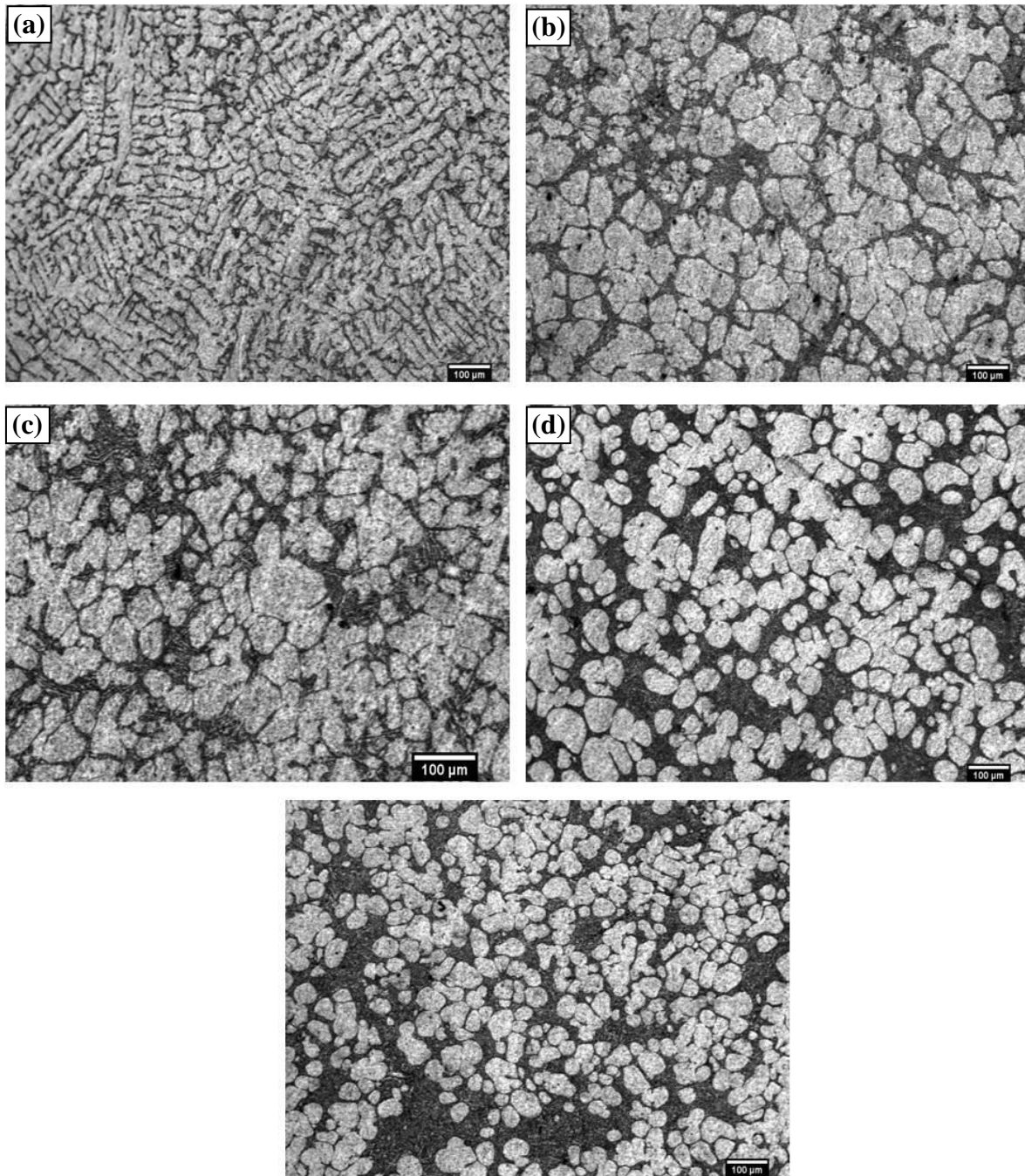
### MECHANICAL PROPERTIES (WITH AND WITHOUT HEAT TREATMENT)

---

This chapter includes the study of the mechanical properties and wears analysis of A356 alloy (with and without heat treatment) in different processing conditions. The mechanical properties and wear analysis of A356 alloy was studied by T5 heat treatment at 170°C for 20 hours. A comparative study between non-heat-treated and heat-treated A356 alloy for different processing conditions also presented. Characterization of the worn surfaces and examination of debris also carried out.

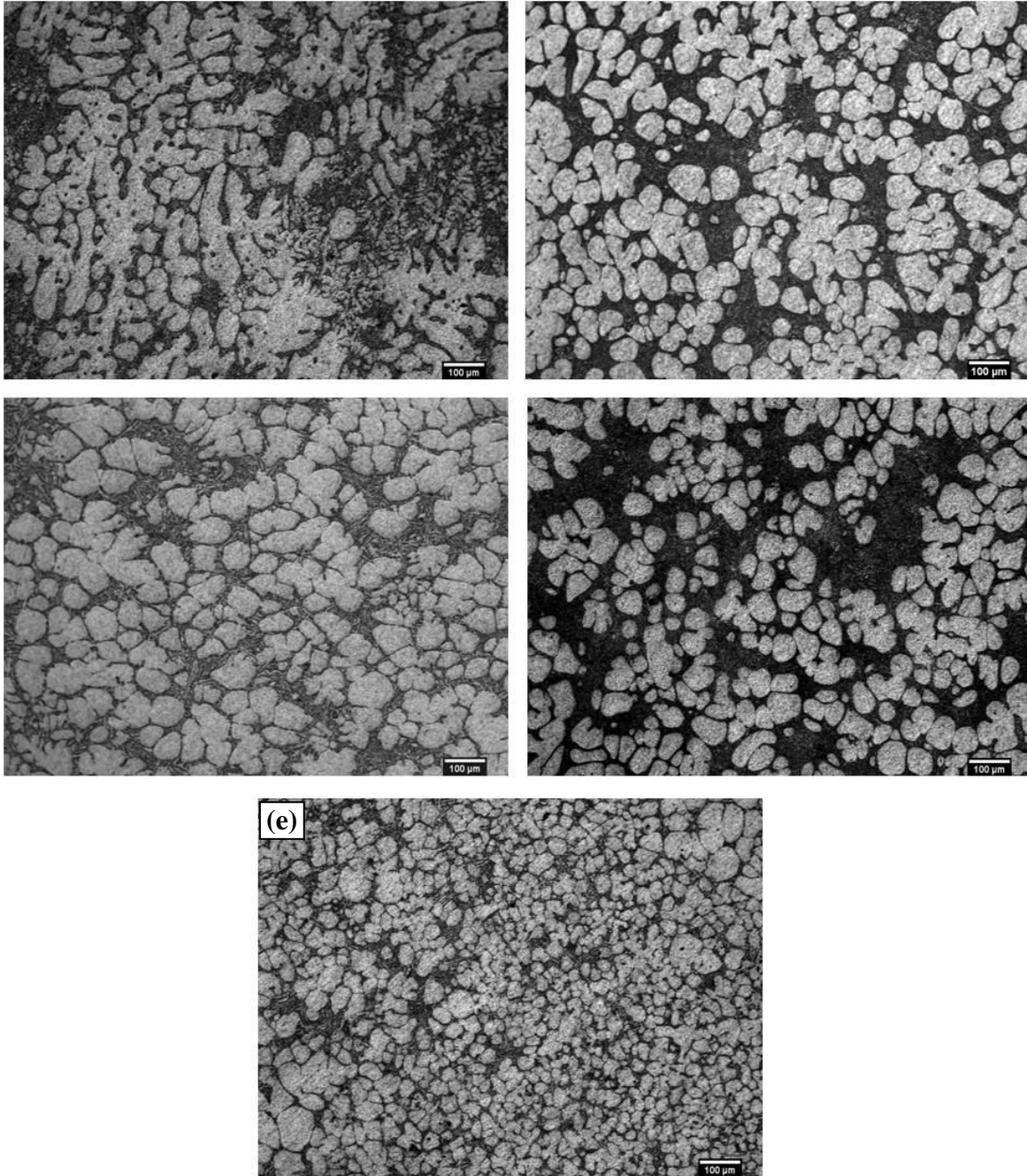
#### 5.1 Microstructural Observations

Figure 5.1(a-e) shows the microstructure of non-heat-treated samples under various conditions. Figure 5.1 (a) represents the microstructure of as-cast A356 alloy having the dendritic morphology of primary  $\alpha$ -Al phase. Figure 5.1(b) illustrates microstructure developed due to the rheometal process in which dendritic structure has changed into globular with the average grain size of 90 $\mu$ m. Shearing developed during rotation of EEM, converts dendrite into globular morphology. Agglomeration of particles due to impingement is also seen [125]. Figure 5.1(c) exhibits a microstructure that has developed in the rheometal process with the provision of baffles. In this case, further refinement in the average grain size of  $\alpha$ -Al up to 80 $\mu$ m has been noted. The tendency of agglomeration of particles is decreased with the use of baffles as evident from Fig. 5.1(c). The addition of grain refiner in the melt without and with baffles further refined the  $\alpha$ -Al phase and globularity of  $\alpha$ -Al has also improved as shown in Fig. 5.1(d-e) respectively. Comparison of microstructural change in Fig. 5.1(a-e) illustrates that fine microstructural features are obtained with the use of baffles and addition of grain refiner in rheometal process [Fig. 5.1(e)].



**Fig. 5.1** Microstructure of RSF non-heat-treated samples (a) A, (b) B, (c) C, (d) D and (e) E.

Effect of T5 treatment on microstructure for similar conditions as represented in Fig.5.1(a-e) is shown in Fig.5.2 (a-e). The fundamental nature of all microstructures remain same with respect to their previous respective conditions. However, heat treatment led to homogenization and refinement of primary  $\alpha$ -Al phase [126-128]. It is viewed from Fig.5.2 (b-e) that aspect ratio of  $\alpha$ -Al phase reached close to one due to heat treatment. The above results revealed that T5 heat-treatment gives rise to fine and uniformly distributed  $\alpha$ -Al phase which is beneficial for mechanical properties of the alloy as shown in Fig. 5.2(a-e).



**Fig. 5.2** Microstructure of RSF heat-treated samples (a) A, (b) B, (c) C, (d) D and (e) E.

## **5.2 XRD Analysis**

The XRD analysis of A356 alloy in different processing conditions is given in Fig.5.3. The XRD analysis showed the presence of  $TiAl_3$  particles in the alloy which provides more nucleating sites for grain refinement and improved the mechanical properties and wear resistance of the alloy.



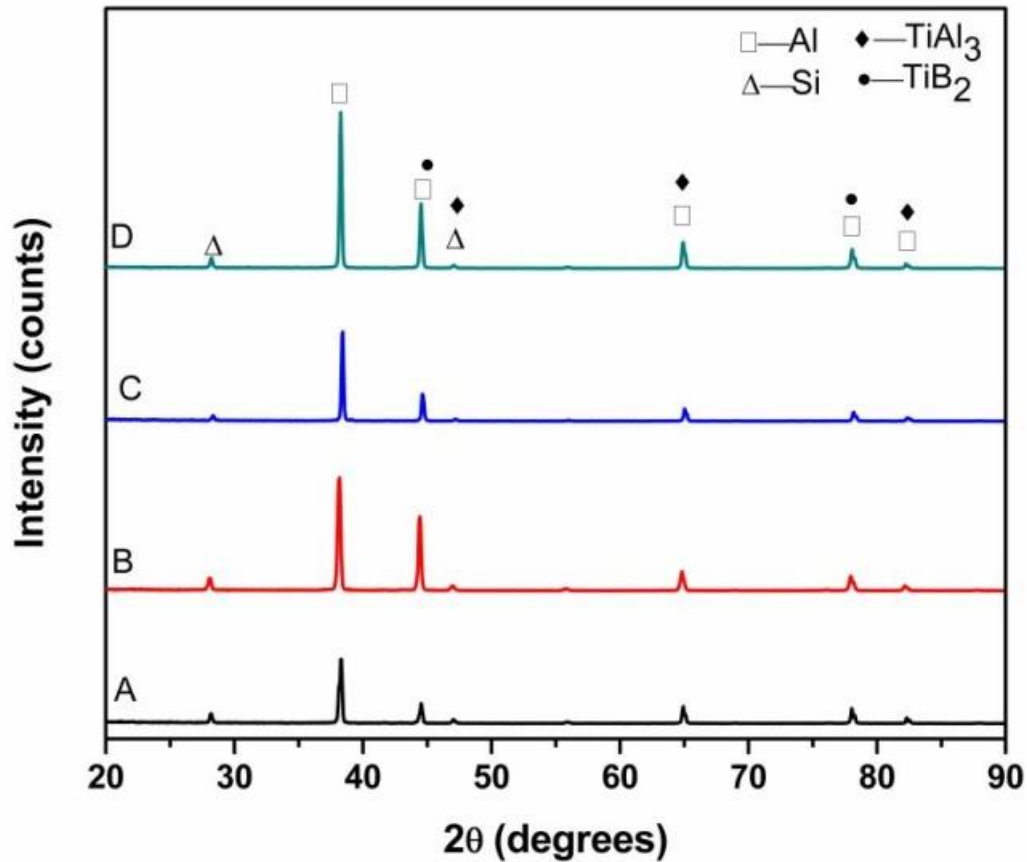


Fig. 5.3 XRD of A356 alloy for (a) non-heated sample A, (b) heat-treated sample A, (c) non-heated sample E and (d) heat-treated sample E.

### 5.3 Effect of Heat Treatment on Porosity

In solidification of Al alloys the dissolved hydrogen creates porosity decreases mechanical properties of the alloy. Porosity is specified concerning voids or cavities formed in the casting during solidification. The heat treatment applied to Al and its alloys reduces chemical segregation of cast structures and improves their work ability. Due to heat treatment the dissolution of hydrogen relatively decreases, which reduces the gas porosity and shrinkage porosity [129]. The variations of porosity volume fraction for non-heat-treated and heat-treated samples in different processing conditions are publicized in Fig.5.4.

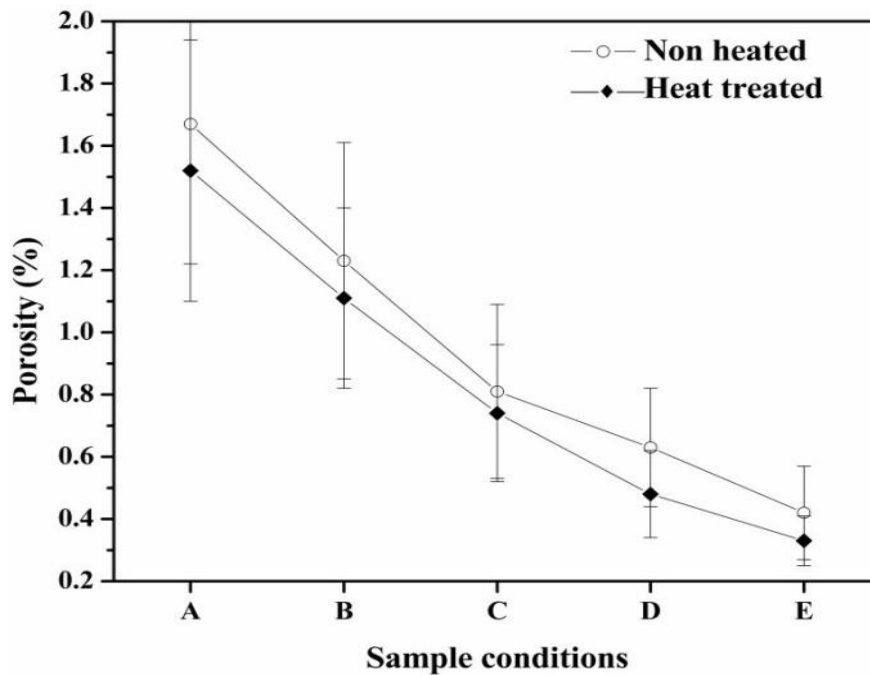


Fig. 5.4 Effect of heat treatment on porosity in different processing conditions.

From Fig. 5.4 it is scrutinized that as the process conditions from sample A to sample E changed the porosity level decreased. T5 heat treatment showed a further reduction in porosity from sample A to sample E when compared with their respective samples in non-heat-treated condition. T5 heat-treatment leads to grain refinement and uniform distribution of eutectic Si in Al matrix helps in reduction the level of porosity [130]. Non-heat-treated sample A has 1.67% porosity, while heat-treated sample A exhibits 1.52% porosity. Chen [131] deliberated that the alloy with porosity level up to 2%, decreased the mechanical properties of the alloy. Therefore, percentage porosity has to be depressed so that it does not affect the mechanical properties adversely. In the present investigation, non-heat-treated sample E illustrates 0.42% porosity, whereas heat-treated sample E comprises 0.33% porosity volume fraction. As sample E showed minimum porosity, therefore, sample E have improved mechanical properties than other conditions.

#### 5.4 Mechanical Properties

Figure 5.5 demonstrates the hardness of A356 alloy from sample A to sample E in both conditions i.e. without and with T5 heat treatment. The hardness of sample E in non-heat-treated condition is improved by 23% when compared with the non-heat-treated sample A (61BHN). It is also interesting to see that due to T5 heat treatment the hardness enlarged by

25% from sample A to sample E. There is about 5% improvement in hardness for all heat-treated specimens (A to E) as compared with sample without heat-treatment.

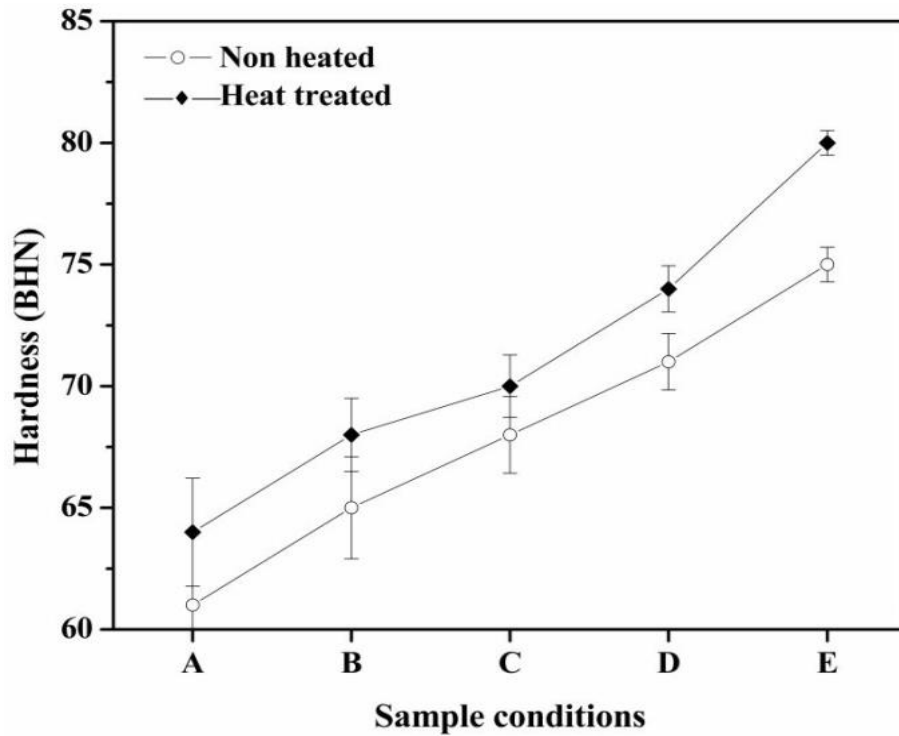


**Fig. 5.5 Effect of heat treatment on hardness of A356 alloy.**

Figure 5.6(a-c) correspond to variation of UTS, yield strength and elongation (%) values for different samples before and after T5 heat treatment. From Fig. 5.6(a-c), it is evident that non-heat-treated sample A illustrates lowest tensile properties owing to dendritic morphology and coarse sharp edged Si needles. Fig. 5.6(a-c) also reveals that heat-treated sample E exhibit best tensile properties as compared to other non-heat-treated and heat-treated conditions.

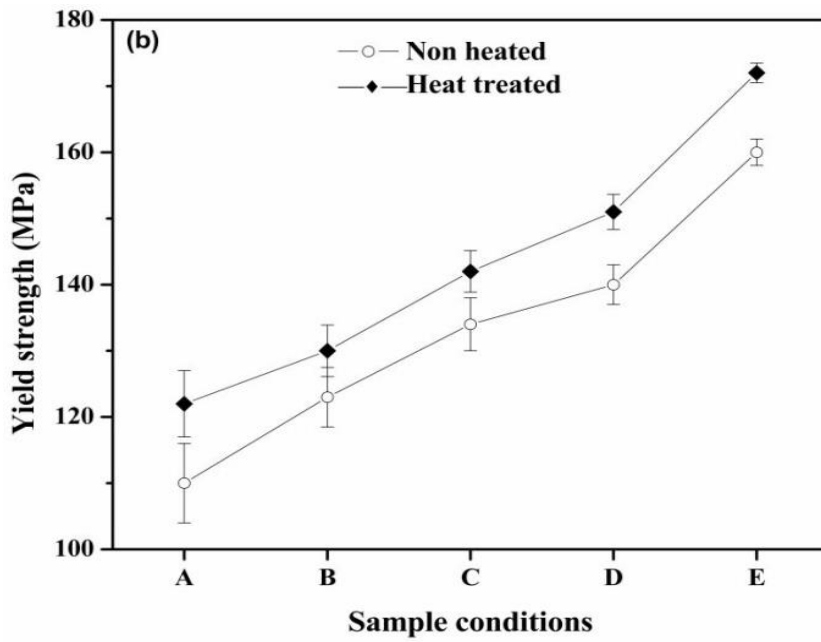
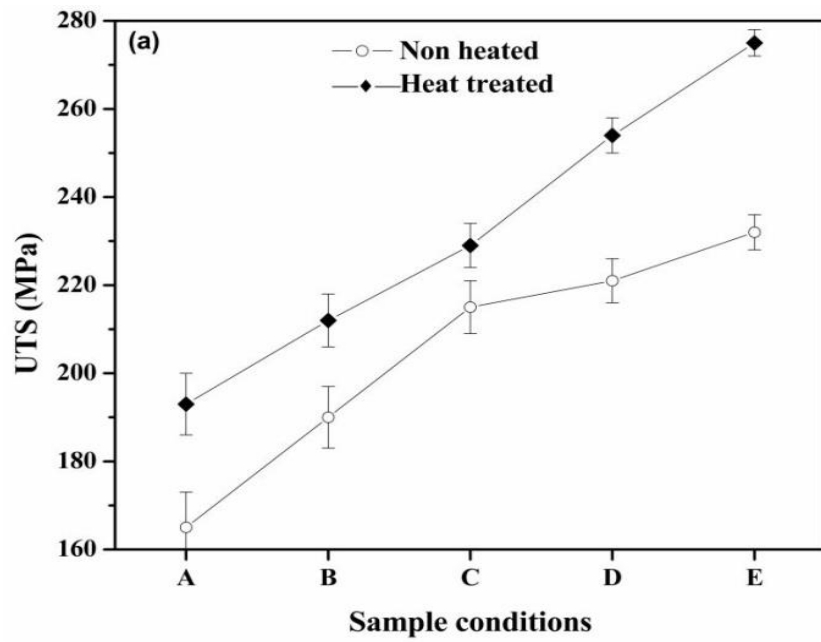


Fig. 5.6 Effect of heat treatment on (a) tensile strength and (b) yield strength of A356 alloy

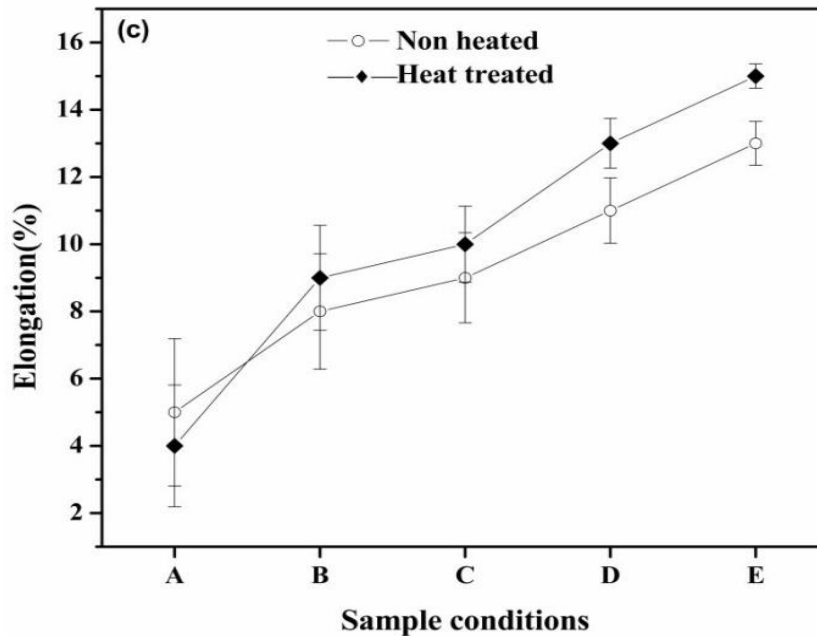


Fig. 5.6 Effect of heat treatment on (c) elongation of A356 alloy.

During rheometal process, shearing takes place which refines the  $\alpha$ -Al phase and Si morphology [132]. Therefore, sample B illustrated the improvement in mechanical properties as compared to sample A. When baffled crucible is used in the rheometal process, baffle modified flow which minimizes the vortex formation and reduces the aspiration effect, and thus porosity decreased. Therefore, further refinement in the morphology of primary  $\alpha$ -Al phase and Si morphology takes place which improved the mechanical properties of sample C as compared to sample B. When grain refiner is added to without and with baffled crucible, then further improvement in the morphology of primary  $\alpha$ -Al phase and Si needles took place which improved the mechanical properties of sample D as compared to sample C. Sample E demonstrated the best tensile properties as compared to other non-heat-treated samples. There is a reduction in elongation (%) for heat-treated sample A when compared with non-heat-treated sample A. T5 heat treatment leads to hardening of  $\alpha$ -Al phase and precipitation of  $Mg_2Si$  phase which results in decreasing the ductility of heat-treated sample A than the ductility of non-heat-treated sample A.

T5 heat treatment leads to homogenization of the primary  $\alpha$ -Al phase and precipitation of  $Mg_2Si$  phase which further improved the mechanical properties of A356 alloy [133-136]. Although during heat treatment the  $Mg_2Si$  phase retards ductility. But due to homogenization

and spherical morphology of  $\alpha$ -Al phase, this effect get minimized. Hence some improvement in ductility is observed even in the presence of  $Mg_2Si$  phase.

The quality index (QI) can be used to observe the effect of heat treatment in different processing conditions [137]. The quality index gives the information about the quality of the parts cast with A356 alloy. The QI explain the direct relation between ductility and UTS into a single term. The QI for A356 alloy in different processing condition is shown in Fig. 5.7 and can be given by Eq. 51.

$$QI(MPa) = UTS(MPa) + 150 \log(\%E) \quad (51)$$

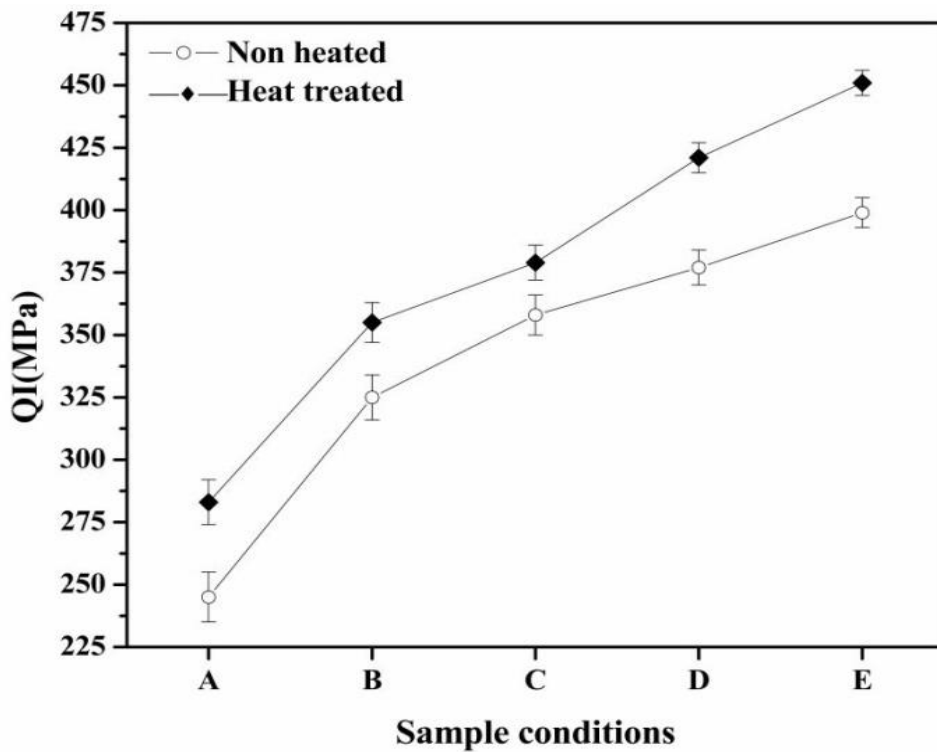
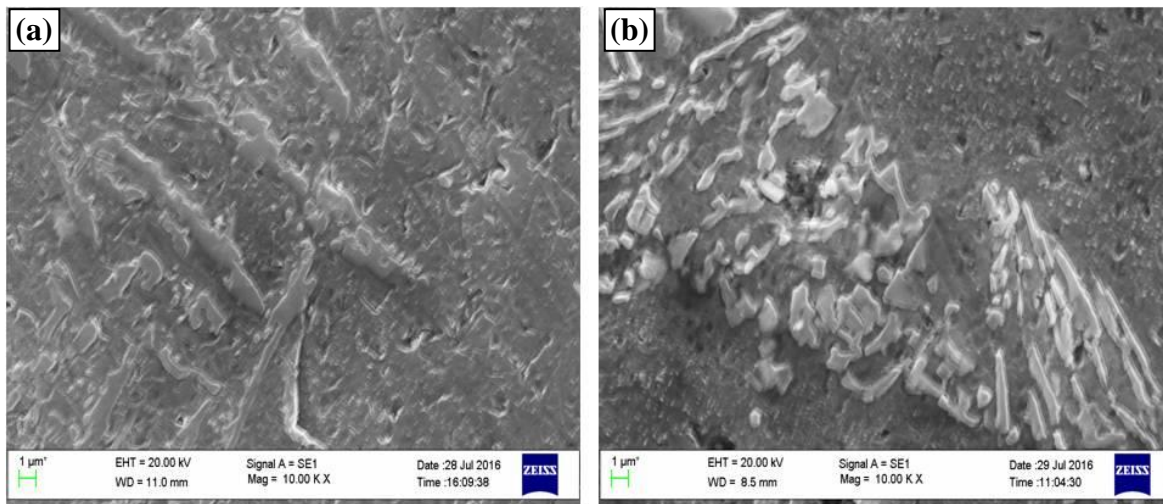


Fig. 5.7 Quality index (QI) of A356 alloy in different processing conditions.

Moller et al. [138] reported the QI for T4, T5 and T6 heat treatment about 442, 396 and 466 MPa values respectively. In the present investigation, sample E showed 451MPa for T5 heat treatment. From above results for QI, it is cleared that T5 heat treatment significantly improved the tensile properties which are beneficial of A356 alloy cast by the rheometal process.

## 5.5 Effect of Heat Treatment on the Morphology of Eutectic Si

In Fig. 5.8 (a-b) SEM micrographs demonstrate the morphological changes of eutectic Si for the non-heat-treated condition. From Fig. 5.8(a) it is noticeable that sample A has long Si needles. These Si needles worked as a stress riser and declined the tensile properties of the alloy. While sample E in Fig. 5.8(b) display the refinement and roundness of sharp corner of Si needles which reduces the stress level and aid in improving the mechanical properties of the alloy [139-140].



**Fig. 5.8 Morphology of eutectic Si in non-heat-treated (a) as-cast and (b) baffle with grain refiner.**

Figure 5.9(a-b) reveals the SEM micrographs of eutectic Si for heat treated A356 alloy for sample A and E. From Fig. 5.9(a-b) it is evident that artificial aging leads to further refinement and globularization of Si needles when compared with the several non-heat-treated conditions (Fig. 5.8a-b). The breakup of large irregularly shaped eutectic Si is similar to that of using Sr as a modifier in the casting [141-142]. Therefore, heat-treated conditions from sample A to E showed improved mechanical properties in comparison to without heat-treated conditions from sample A to E.

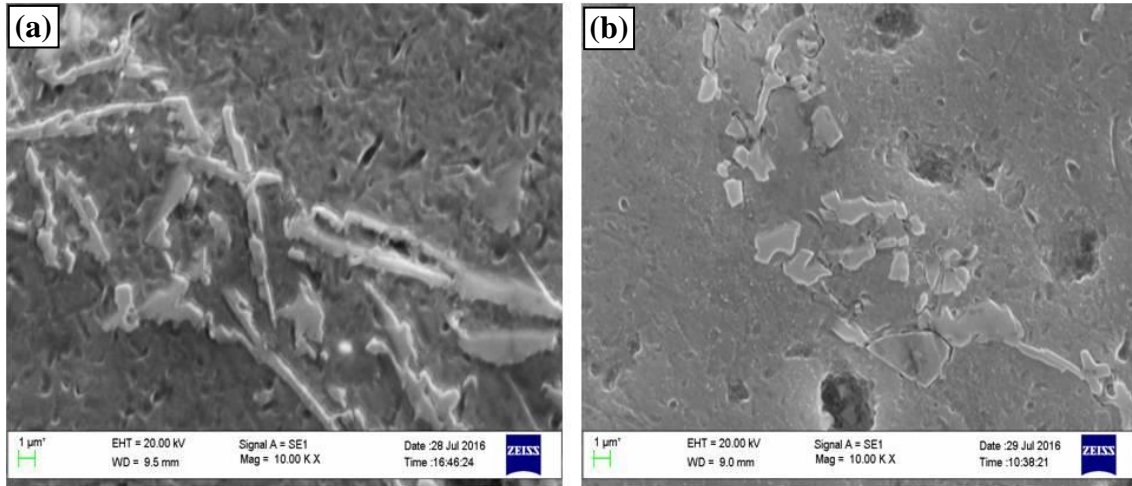


**Fig. 5.9 Morphology of eutectic Si in heat-treated (a) as-cast and (b) baffle with grain refiner.**

### 5.6 EDS Analysis

EDS analysis of the non-heat-treated and heat-treated sample is also carried out to support the results obtained in the microstructure and mechanical properties. Figure 5.10 and Fig. 5.11 show the EDS analysis of sample E without and with heat treatment respectively. So from both Fig. 5.10 and Fig. 5.11 it is confirmed that T5 heat treatment leads to the precipitation of  $Mg_2Si$  intermetallic phase at grain boundaries.

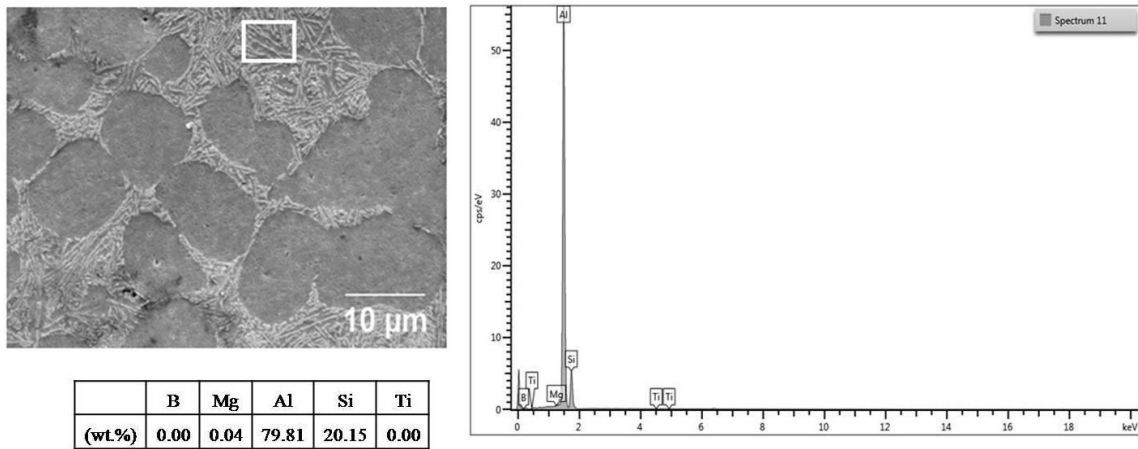


**Fig. 5.10 EDS analysis of non-heat-treated sample E.**



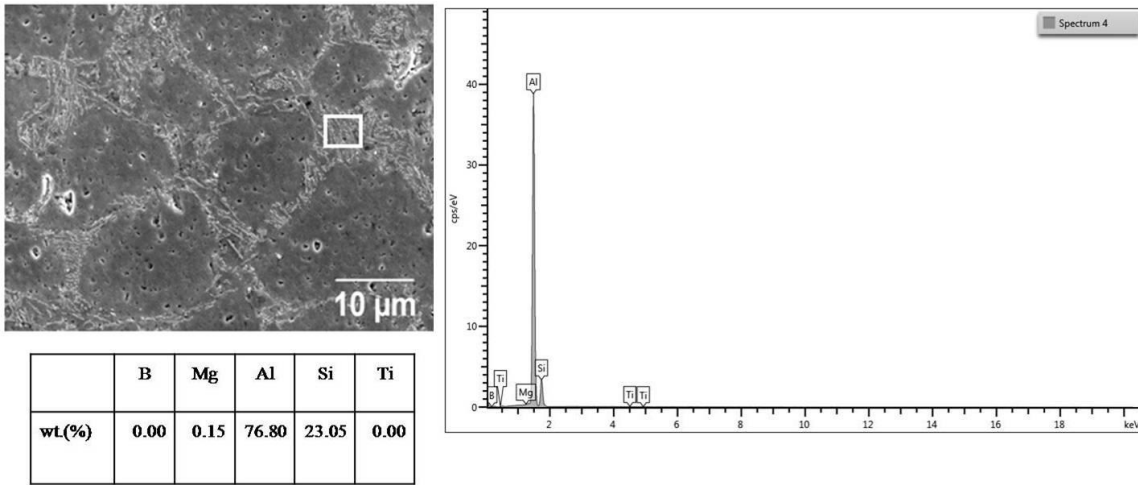


**Fig. 5.11 EDS analysis of heat-treated sample E.**

### 5.7 Fractography

SEM was employed for fracture surface after the tensile test to observe the mode of fracture. The fracture surfaces of non-heat-treated A356 alloy in different processing conditions are shown in Fig. 5.12(a-e). Since sample A in Fig. 5.12(a) comprises cleavage pattern which is an indication of low ductility. While Fig. 5.12(b) shows a quasi-cleavage pattern with very few dimples: is an indication of improvement in elongation (%) when compared with sample A. Use of baffles and addition of grain refiner aids to refinement in average grain size of primary  $\alpha$ -Al phase and rounding of eutectic Si, therefore, the analysis of fracture surfaces from Fig. 5.12(c-e) reveals more dimples when compared with sample B. Presence of dimples shows a further improvement in the ductile behavior of A356 alloy.

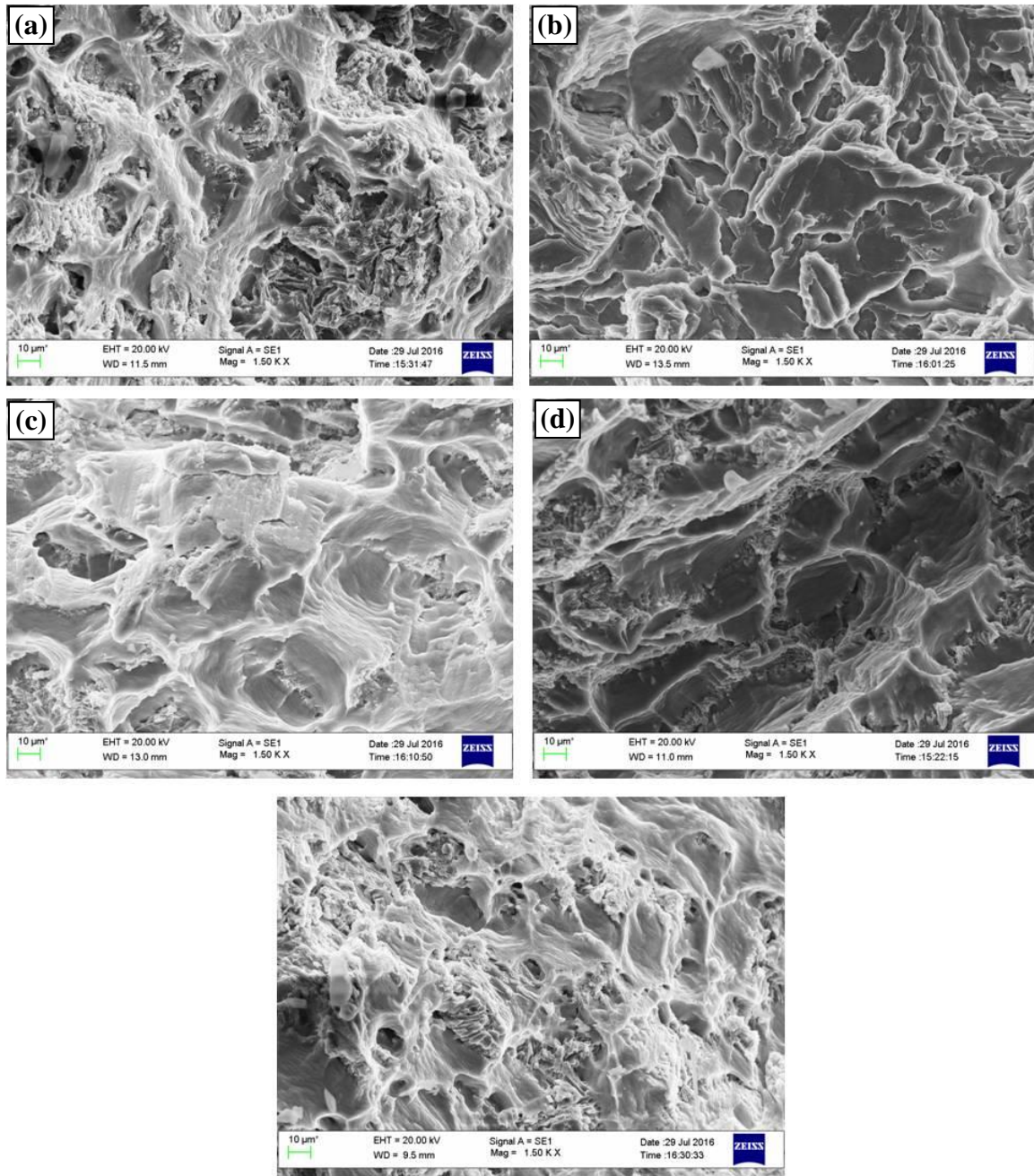


**Fig. 5.12** Fracture surface of RSF non-heat treated A356 alloy in different processing conditions; (a) A, (b) B, (c) C, (d) D and (e) E.

T5 heat treatment leads to uniform distribution of dimple morphology than non-heat treated A356 alloy in similar conditions. Therefore, heat treated A356 alloy from sample A to E in Fig. 5.13(a-e) comprises more dimples when compared with their respective non-heat treated conditions.

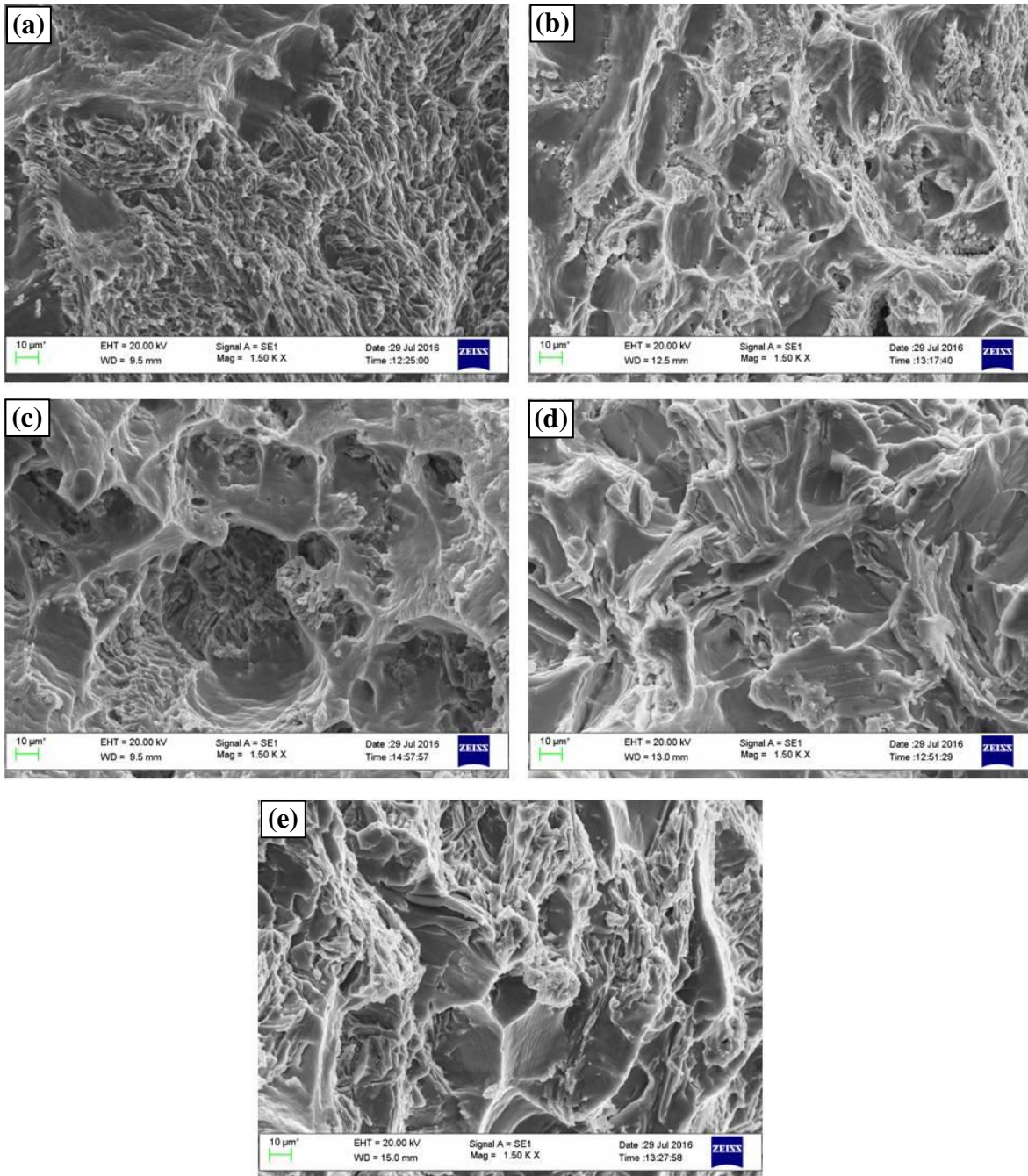


**Fig. 5.13 Fracture surface of RSF heat treated A356 alloy in different processing conditions; (a) A, (b) B, (c) C, (d) D and (e) E.**

## 5.8 Wear Analysis

### 5.8.1 Analysis of specific wear rate

Figure 5.14 illustrates the specific wear rate (SWR) of A356 alloy for sample A to E under both non-heat-treated and heat-treated conditions.

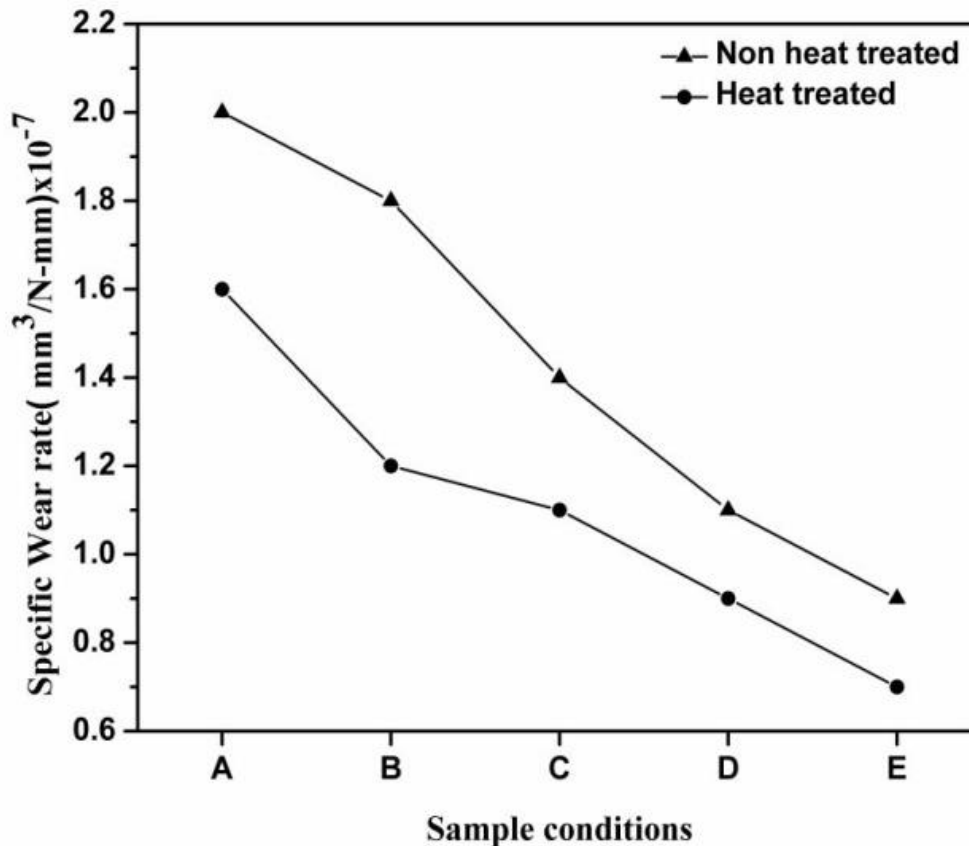


Fig. 5.14 Specific wear rate in various processing conditions.

The results showed that for the non-heat treated samples as the processing conditions changed, the SWR decreased. This is observed because as the processing conditions from sample A to sample E changed the average grain size continuously decreased. The similar trends also take place for all heat-treated specimens, as the processing conditions changed the SWR continuously decreased. The observations also revealed that heat-treated samples exhibit lower specific wear rate than their respective non-heat-treated condition. The reason being that heat treatment increased the strength of the matrix and hardness. It is also noticed that sample A in both conditions showed higher specific wear rate in comparison to respective specimens B to E. Sample E showed maximum wear resistance or lower specific wear rate in both conditions. It is

attributed to the fact as the processing conditions changed from A to E, the refinement of primary  $\alpha$ -Al phase occurred.

### **5.9 SEM Analysis of Worn Surfaces**

Figure 5.15 and Fig. 5.16 illustrate the SEM micrographs of worn surface of A356 alloy before and after heat treatment under different processing conditions. Figure 5.15(a) demonstrates the worn surface of an as-cast A356 alloy which exhibits deep grooves all over the surface, oxide layers and craters. Figure 5.15(b) shows the worn surface of sample B where worn surface illustrated similar marks of entrapped debris, abrasive grooves and oxide layer as shown in Fig. 5.15(a). However, the marks are lesser in number than that observed in Fig. 5.15(a). Figure 5.15(c) shows SEM micrograph of sample C. The worn surface for sample C showed the lesser number of entrapped debris and oxide layer when compared to Fig. 5.15(a-b). In Fig. 5.15(d) the worn surface of the sample D exhibits oxide film, a lesser number of entrapped debris in comparison to Fig. 5.15(a-c). Figure 5.15(e) represents the worn surface for sample E in which few discontinues parallel grooves and oxides particles are observed and less damage has occurred owing to higher wear resistance in comparison to samples A to D.



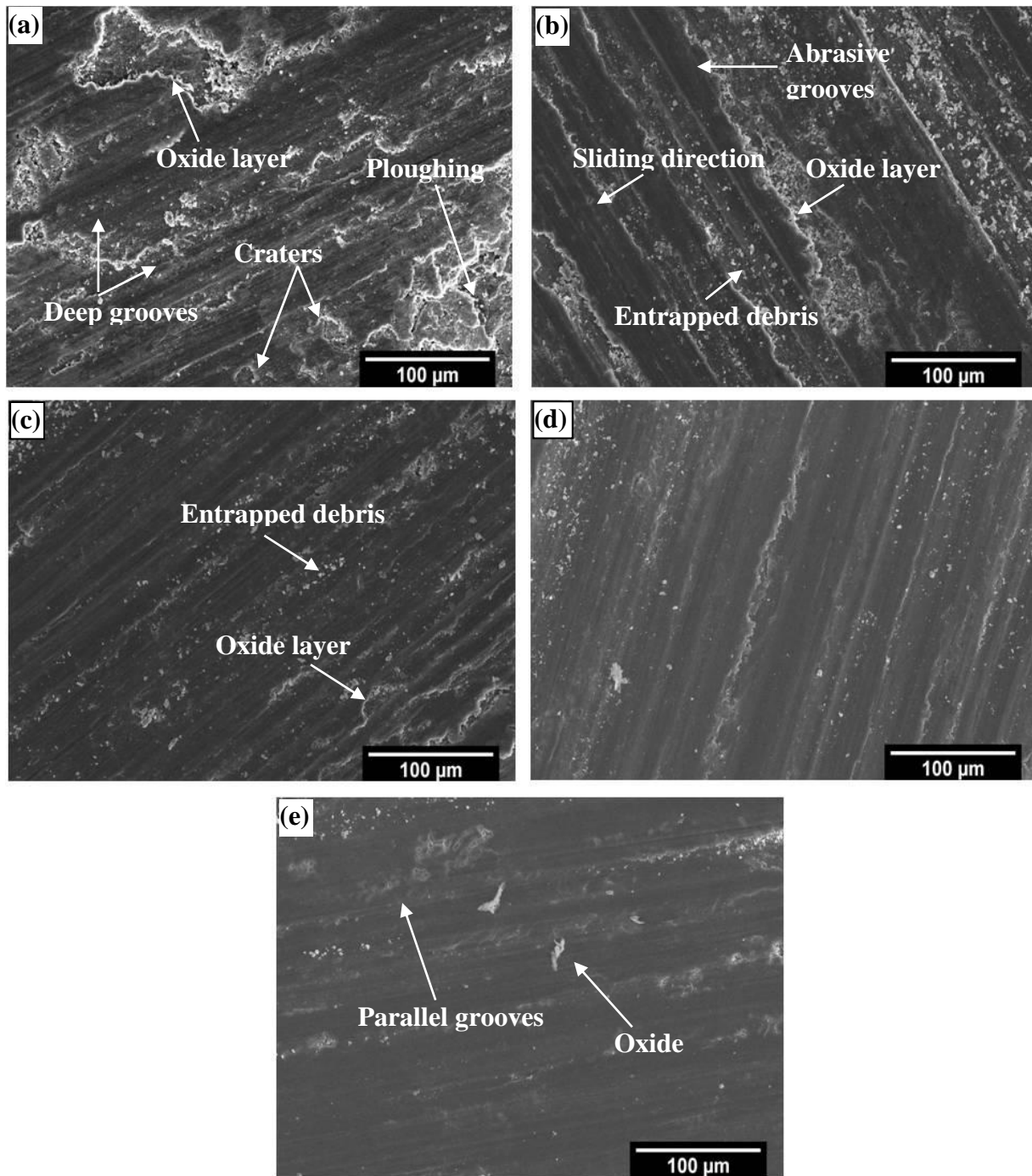


**Fig. 5.15 SEM micrographs of worn surfaces for non-heat-treated samples (a) A, (b) B, (c) C, (d) D and (e) E.**

In present investigation as sliding begins under the action of applied load, the frictional forces transfer the material on counterface. Due to applied load and speed, A356 sample surface breaks into fine particles. In the mild area of wear, fracture of the oxide layer from the surface of wear pin occurs. Since the load level is not high enough to cause deep penetration and

deformation of metal below the oxide layer, oxide particles form between pin surface and counterface of steel [143-144].

Effect of T5 heat treatment on SEM micrographs of the worn surface with similar conditions as in Fig. 5.15(a-e) is dispensed in Fig. 5.16(a-e). From Fig. 5.16(a) it is cleared that heat-treated sample A represents few adhesive region, abrasive grooves and entrapped debris. The heat-treated specimen B in Fig. 5.16(b) shows abrasive grooves, few oxides layer and entrapped debris in comparison to non-heat-treated sample B in Fig. 5.15(b). Figure 5.16(c) shows the worn surface of heat-treated sample C. In this case the worn surface have oxide layer and parallel grooves all over the surface. Fig. 5.16(d) illustrates the worn surface of sample D where the worn surface revealed minor damage. The worn surface in Fig. 5.16(e) exhibits fine parallel grooves with few oxide layers and less damage of the worn surface of sample E [19]. This explains that sample E exhibited high wear resistance in comparison to samples A to D for heat-treated samples. Thus heat-treated sample E showed minimum wear loss as compared to other samples under both conditions.

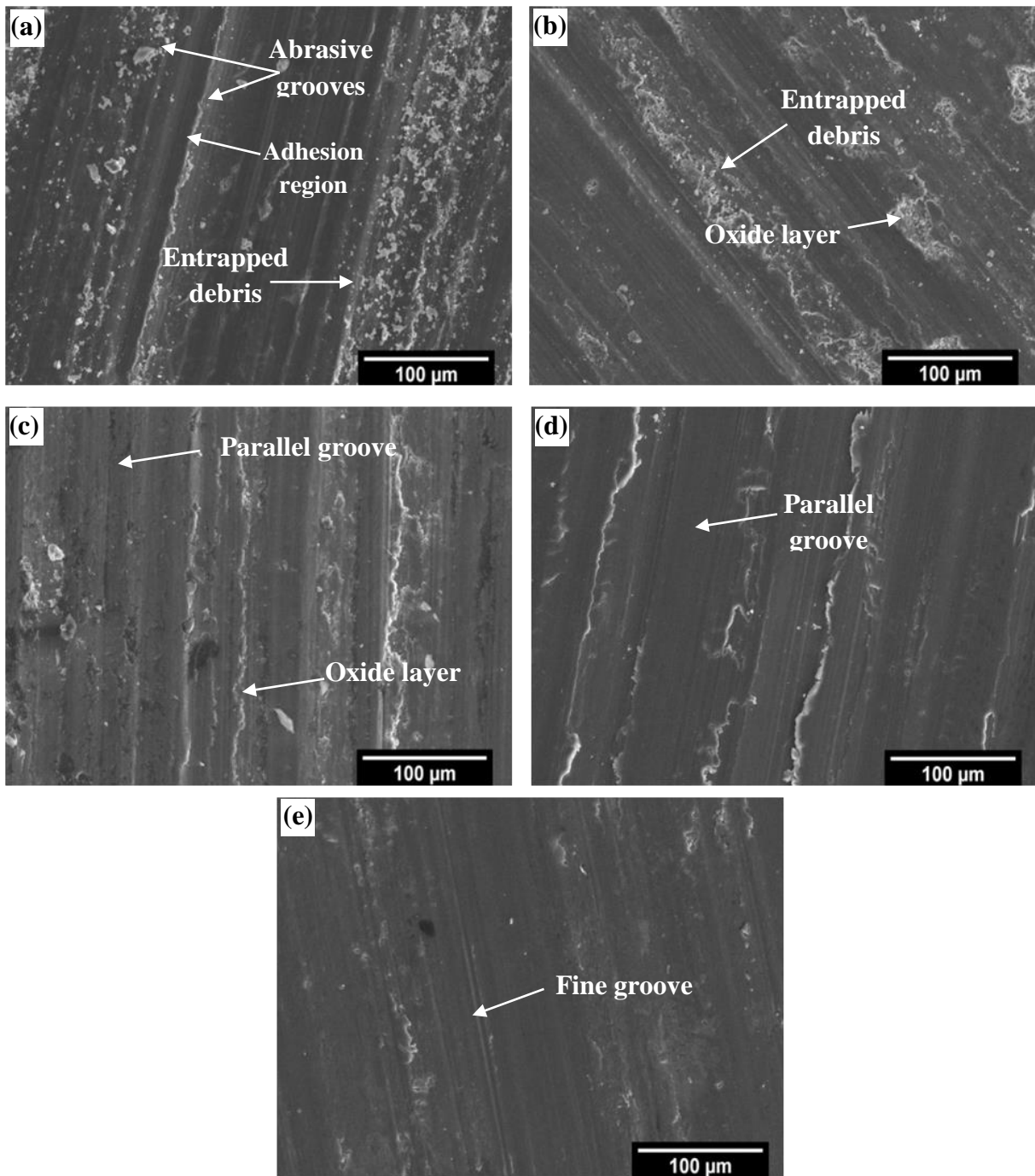


**Fig. 5.16** SEM micrographs of worn surfaces for heat-treated samples (a) A, (b) B, (c) C, (d) D and (e) E.

The existences of ploughing showed abrasive wear mechanism, while crater is a feature of delamination type of wear [145-146]. The adhesive wear mechanism occurred due to the transition of hard particles to the counterface, which can be controlled by the hardness. Therefore, hardness plays a role in controlling the wear during sliding beside strength [147].



## 5.10 Analysis of Wear Debris

Figure 5.17 (a-b) illustrates SEM micrograph of wear debris for non-heat-treated sample A and sample E. Figure 5.17(c) shows the SEM micrograph of heat-treated sample E. From Fig. 5.17(a) it is depicted that sample A demonstrates the debris of bigger size, while sample E in Fig. 5.17(b) has small debris when compared to sample A. Figure 5.17(c) shows that heat-treated sample E exhibited the fine debris. The fine debris is an indication of higher wear resistance for the A356 alloy.

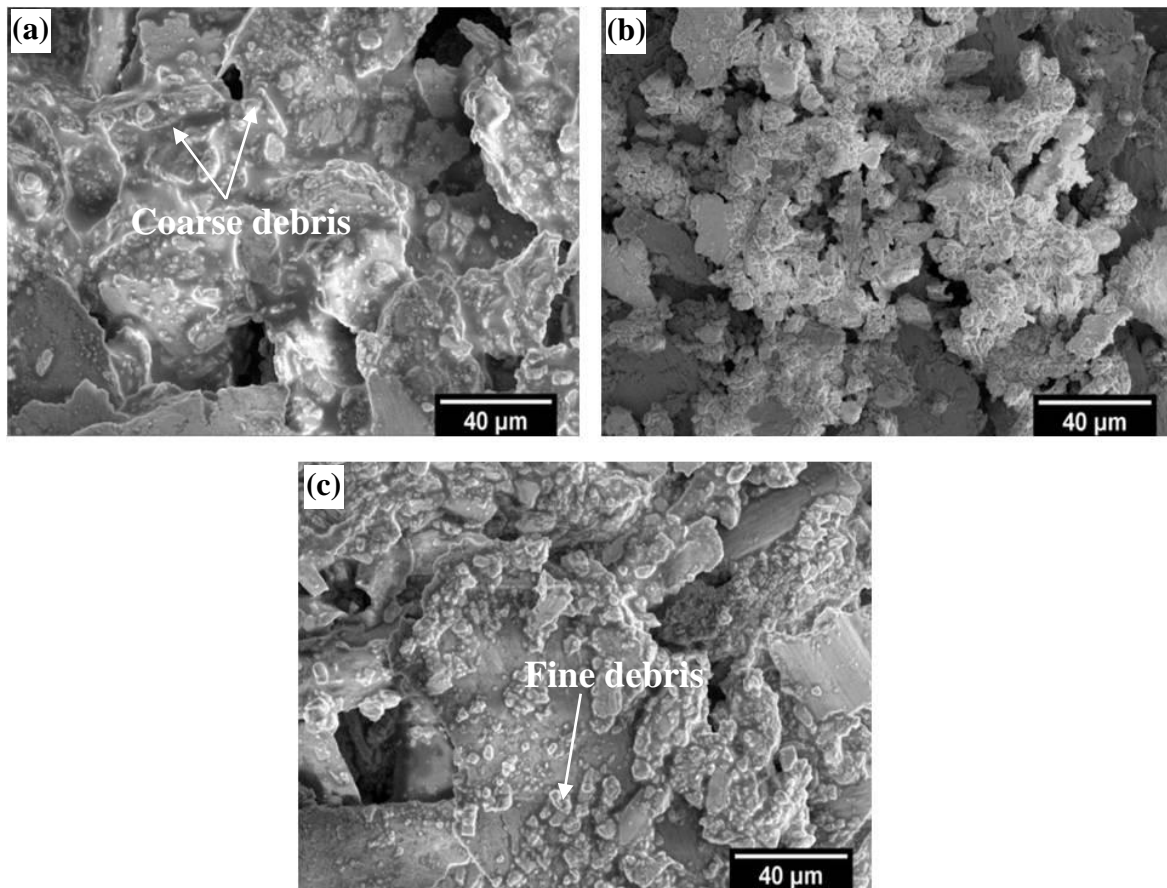


**Fig. 5.17 SEM micrographs of worn surfaces for non-heat-treated samples (a) A, (b) E and (c) heat- treated sample E.**

Since as-cast A356 alloy has dendritic  $\alpha$ -Al phase with coarse Si needles which leads to initiating a crack and their propagation and caused severe wear [128]. It is evident that globular  $\alpha$ -Al phase and refinement of eutectic Si for sample B to E improved mechanical properties and wear resistance of the alloy. The addition of 0.6wt.% grain refiner in the melt released more heterogeneous nucleating sites ( $\text{TiAl}_3$  and  $\text{TiB}_2$ ) in the melt and led to the refinement in the

average grain size of  $\alpha$ -Al phase. Heat treatment improved mechanical properties and provided strength to the matrix of  $\alpha$ -Al phase [88]. From SEM analysis it is observed that no single wear mechanism is responsible and more than one mechanism takes place for material loss from the sliding surface. Therefore, this is a complex phenomenon. From wear analysis, it is clear that A356 alloy with fine and more globular primary  $\alpha$ -Al phase comprised higher wear resistance in comparison to the with coarse and less globular  $\alpha$ -Al phase.

## CHAPTER 6

### CONCLUSIONS AND FUTURE WORK

---

Based on present investigations the following conclusions are made.

- Microstructural changes from dendritic to rosette and later to globular morphology as a function of stirring time takes place.
- The outcome indicates that an increase in stirring speed reduces the average grain size of  $\alpha$ -Al phase. The optimum results are obtained at 1000 rpm regarding average grain size and shape factor.
- The use of baffles comprises a fine and more globular primary  $\alpha$ -Al phase than samples processed without baffles. Baffles reduce aspiration of air.
- The average grain size of primary  $\alpha$ -Al phase increases with holding time, but the rate of coarsening kinetics decreased as the stirring speed increased.
- There was a contribution of diffusive LSW and convective mass flow in the morphological changes during RSF process. However, both were unable to satisfy the explanation fully. Therefore, the coalescence phenomena were also considered. In coalescence processes, particles combine and form the aggregates of large particles.
- When a grain refiner was added to the melt, it provides more nucleation sites and suppressed the growth of  $\alpha$ -Al and leads to additional refinement.
- Microstructural evolution showed that non-heat treated as-cast A356 alloy reveals a dendritic morphology of primary  $\alpha$ -Al and coarse Si needles.
- These long Si needles worked as stress risers, which lead to poor mechanical properties and wear resistance of the alloy.
- Due to this, deep abrasive grooves, oxide layers and craters were seen in the as-cast A356 alloy. While rheometal process showed globular morphology which helped in improving the mechanical properties and wear resistance of the A356 alloy. The addition of grain refiner and use of baffle decreased the average grain size of primary  $\alpha$ -Al phase and porosity.
- T5 heat treatment led to the homogenization of primary  $\alpha$ -Al phase and precipitation of  $Mg_2Si$  phase which results in further improvement in mechanical properties and wear resistance of the alloy when compared to their respective non-heat-treated conditions.

## **Future Work**

The suggestions for future work are;

- Tomography studies on A356 alloy can be explored to get the internal structure of the samples.
- TEM studies can be studied to observe the orientation relationship of the phase present in the alloy.
- Extensive study about the machinability and corrosion resistance of A356 alloy may also be performed.

## References

1. Y. Sirong, L. Dongcheng and N. Kim, Microstructure evolution of SIMA processed Al2024, *Material Science and Engineering A*, 420, 2006,165-170.
2. D. B. Spencer, R. Mehrabian and M. C. Flemings, Rheological behavior of Sn-15% Pb in the crystallization range, *Metallurgical Transactions*, 3(7), 1972, 1925–1932.
3. O. Lashkari and R. Ghomashchi, The implication of rheology in semi-solid metal processes: an overview, *Journal of Material Processing Technology*, 182, 2007, 229–240.
4. M. Wessen, O. Granath and H. Cao, Influence of holding time on particle size of an A356 alloy using new rapid slurry formation process, *International Conference of High Tech Die Casting*, Vicenza, Italy, 2006, 1-11.
5. Z. D. Zhao and W.M. Mao, Preparation of semi-solid AlSi7Mg alloy slurry”, *Acta Metallurgica Sinica*, 21(2), 2008, 139-145.
6. <http://www.rheomet.com>
7. <http://www.rheometal.com>
8. V. Raghvan, *Material Science and Engineering*, PHI, edition 4, 2000.
9. S. Nafisi, PhD thesis, Effects of grain refining and modification on the microstructural evolution of semi-solid 356 alloy, University of Quebec, 2006.
10. M. Taheri, Lecture 2, Fundamentals of nucleation, *Material Science and Engineering*, Drexel University, 2011.
11. K. T. Kashyap and T. Chandrashekar, Effects and mechanisms of grain refinement in aluminium alloys, *Bulletin of Material Science*, 24(4), 2001, 345–353.
12. O. P. Khanna, *A text book of foundry technology*, edition 2, Dhanpat Rai & Sons, 1996.
13. S. Klein, PhD thesis, Nucleation in undercooled melts of pure Zr. And Zr. Based alloys, Ruhr-University Bochum, 2010.
14. D. Kohli and A. Sharma, Solidification and grain refinement in aluminium alloys, *Foundry*, 2009, 81-87.
15. H. Men, Z. Fan, Effects of solute content on grain refinement in an isothermal melt, *Acta Materialia* 59, 2011, 2704–2712.
16. J. Campbell and R. A. Harding, *The freezing of castings*, IRC in Materials, The University of Birmingham, Edition 1, 1993.

17. R. K. Mahenti, K. Lal, A. N. Sinha and C. S. Sivaramakrishnan, A novel technique for hyper eutectic aluminium-silicon alloy melt treatment, *Materials Transactions, JIM*, 34(12), 1993, 1207-1211.
18. M.A. Easton and D. S. John, Grain refinement of aluminum alloys: part I. the nucleant and solute paradigms-a review of the literature, *Metallurgical and Materials Transactions A*, 30(6), 1999, 1613-23.
19. M. A. Easton and D. S. John, Grain refinement of aluminum alloys: part II. confirmation of, and a mechanism for, the solute paradigm, *Metallurgical and Materials Transactions A*, 30(6), 1999, 1625-33.
20. G. W. Boone, R. F. Carver and W. C. Setzer, Performance characteristic of metallurgical grain refiner in hypo-eutectic Al-Si alloy, *Proceeding of the International Symposium on Production, Refining, Fabrication and Recycling of Light Metals*, Ontario, Canada, 1990.
21. S. Nafisi and R. Ghomashchi, Grain refining of conventional and semi-solid A356 Al-Si alloy, *Journal of Materials Processing Technology*, 174, 2006, 371–383.
22. R. Haghayeghi, PhD thesis, Grain refinement and nucleation processes in aluminium alloys through liquid shearing, Brunel University, United Kingdom, 2009.
23. R. J. Kissling and J.F. Wallace, Grain refinement of aluminum castings, *Foundry*, 1963 78–82.
24. P. Kunnam and C. Limmaneevichitr, Effect of process parameters on morphology and grain refinement efficiency of  $TiAl_3$  and  $TiB_2$  in aluminium casting. *Journal of Materials Science and Technology*, 24, 2008, 54-56.
25. P. S. Mohanty and J. E. Gruzleski, Grain refinement mechanisms of hypoeutectic Al-Si alloys, *Acta Materialia*, 44(9), 1996, 3749-3760.
26. P. Schumacher, A. L. Greer, J. Worth, P. V. Evans, P. Fisher and A. H. Green, New studies of nucleation mechanisms in Al-alloys: implications for grain-refinement practice. *Material Science and Technology*, 14, 1998, 394-404.
27. A. L. Greer, A. M. Bunn, A. Tronche, P. V. Evans, and D. J. Bristow, Modelling of Inoculation of Metallic Melts: Application to Grain Refinement of Aluminium by Al-Ti-B. *Acta Materialia*, 48, 2000, 2823-2835.
28. M. Johnsson, L. Backerud and G. K. Sigworth, Study of the mechanism of grain refinement of aluminium after additions of Ti-containing and B-containing master alloys, *Metallurgical and Materials Transactions A*, 24, 1993, 481-491.

29. H. T. Li, Y. Wang, and Z. Fan, Mechanisms of enhanced heterogeneous nucleation during solidification in binary Al–Mg alloys, *Acta Materialia*, 60, 2012, 1528–1537.
30. D. B. Spencer: PhD thesis, Rheology of liquid-solid mixtures of lead-tin MIT, Cambridge, MA, 1971.
31. Z. Fan, Semi-solid metal processing, *International Material Review*, 47,2002, 49-85.
32. K. P. Young, C. P. Kyonka and J. A. Courtois, Fine grained metal composition, U. S. Patent 4, 1982, 415.
33. C.S. Rice and P.F. Mendez, Slurry-based semi-solid die casting, *Advanced Materials and Processes*, 10, 2001, 49-52.
34. J. Jorstad, M. Thieman, R. Kamm, M Loughman and T. Woehlke, Sub-liquidus casting: process concept and product properties, *American Foundry Society Transactions*, 80, 2003, 03-16.
35. J. Jorstad, M. Thieman and R. Kamm, SLC; the newest and most economical approach to semi-solid metal casting, 7<sup>th</sup> International Conference on Semi-Solid Processing of Alloys and Composites, Tsukuba, Japan, 2002, 701-706.
36. L. Ratke and A. Sharma, Microstructural studies of A357 alloy cast by RSF process, *Transactions of Indian Institute of Metals*,62,2009, 327-330.
37. A. Sharma, Synthesis of semi-solid slurry and effect of inoculants on microstructure of A356 alloy cast by rapid slurry forming (RSF) process, *La Metallurgia. Italiana*, 4, 2013, 53-58.
38. U.A. Curle: Ph.D. thesis, Properties of R-HPDC Al-Zn-Mg-Cu aluminium alloys, University of Witwatersrand, Johannesburg, 2015.
39. M. Reiner, Deformation strain and flow: an elementary introduction to rheology, H. K. Lewis, London, 1969.
40. M. J. Adams, B. J. Briscoe and M. Kamjab, The deformation and flow of highly concentrated dispersions, *Advances in Colloid and Interface Science*, 44, 1993, 143–182.
41. H. A. Barnes, A handbook of element of rheology, 1<sup>ST</sup> edition, Cambrian Printers, L lanbadarn Road, Aberystwyth, 2000.
42. V. Wazer, Viscosity and flow measurement: a laboratory handbook of rheology, Inter science Publisher, 1963.
43. G. Schramm, A practical approach to rheology and rheometry, Gebrueder Haake Publisher, 1994.

44. L. Ma, C. Denny, L. Davis, G. Obaldo, V. Gustavo and B. Canovas, Engineering properties of food and other biological materials, ASAE Publisher, 1998.
45. J.O. Wilkes, Fluid mechanics for chemical engineers, Second Edition, Prentice Hall Professional Technical Reference Publisher, 2006.
46. T. Basner, Rheocasting of semi-solid A357 aluminum alloy, SAE Technical Paper Series, 2000, 1-5.
47. M. C. Flemings, Behavior of metals in the semi-solid state, Metallurgical Transactions, A22, 1991, pp.957-981.
48. R. A. McLelland, N. G. Henderson and H. V. Atkinson, Anomalous rheological behavior of semi-solid alloy slurries at low shear rates, Material Science and Engineering A, 232(1-2), 1997, 110-118.
49. H. Atkinson, Current status of semi-solid processing of metallic materials, Advances in Material forming, 2007, 81-98.
50. A. Rouff, V. Favier and R. Bigot, Characterization of thixoforging steel during extrusion tests, Proceedings of 7<sup>th</sup> International Conference on Semi-Solid Processing of Alloys and Composites, 2002, 355-360.
51. Z. Fan and J. Y. Chen, Modeling of rheological behavior of semi-solid metal slurries part 2, steady state behavior, Material Science and Technology, 18, 2002, 243-249.
52. S. Nafisi, O. Lashkari, R. Ghomashchi and A. Charette, Effect of different fraction solids on the fluidity of rheocast 356 Al-Si alloy, Proceedings of Multi Phase Phenomena and CFD Modeling and Simulation in Materials Processes, TMS Publication, North Carolina, 2004, 119-128.
53. C. Beckermann, Modelling of macro-segregation: applications and future needs, International Materials Reviews, 47(5), 2002, 243.
54. D. Brabazon, D.J. Browne and A. J. Carr, Experimental investigation of the transient and steady state rheological behavior of Al-Si alloys in the mushy state, Materials Science and Engineering A, 2003, 69-80.
55. D. H. Kirkwood, M. Suery, P. Kapranos, H. V. Atkinson, K. P. Young, M. Suery, C. H. Peng and K. K. Wang, Semi-solid processing of alloys, Springer, Berlin, Heidelberg, 124, 2010.
56. M. Modigell and J. Koke, Time-dependent rheological properties of semi-solid metal alloys, Mechanics of Time-Dependent Materials, 3, 1999, 15-30.



57. V. Pouya and S. A. Sadough, An enhanced Herschel–Bulkley model for thixotropic flow behavior of semi-solid steel alloys, *Metallurgical and Materials Transactions B*, 44, 2013, 1304-131.
58. M. C. Flemings, R. G. Riek and K. P. Young, Rheocasting, *Materials Science and Engineering*, 25, 1976,103-117.
59. S. Simlandi, N. Barman and H. Chattopadhyay, Study on rheological behavior of semi-solid A356 alloy during solidification, *Transactions of Indian Institute of Metals*, 65, 2012, 809–814.
60. A. Y. Malkin, *Rheology fundamental*, Chemtec publication, 1994.
61. J. Koke and M. Modigell, Flow behavior of semi-solid metal alloys. *Journal of Non-Newtonian Fluid Mechanics*, 112(2-3), 2003, 141–160.
62. L. Ratke, A. Sharma and D. Kohli, Effect of process parameters on properties of Al-Si alloys cast by rapid slurry formation (RSF) technique, *The 3rd International Conference on Advances in Solidification Processes*, IOP Conf. Series: Materials Science and Engineering, 27, 2011, 1-7.
63. P. A. Joly and R. Mehrabian, The rheology of a partially solid alloy, *Journal of Materials Science*, 11(8), 1976, 1393-1418.
64. N. Barman, P. Kumar and P. Dutta, Studies on transport phenomena during solidification of an aluminum alloy in the presence of linear electromagnetic stirring, *Journal of Materials Processing Technology*, 209, 2009, 5912–5923.
65. O. Granath, M. Wessen and H. Cao, Determining effect of slurry process parameters on semi-solid A356 alloy microstructures produced by rheometal process, *International Journal of Cast Metals Research*, 21(5), 2008, 349-356.
66. J. J. Cheng, D. Apelian and R. D. Doherty, Processing-structure characterization of rheocast IN-100 super alloy, *Metallurgical Transactions A*, 17(11), 1986, 2049-2062.
67. S. Turng and K. K. Wang, Rheological behavior and modelling of semi-solid Sn-15% Pb alloy, *Journal of Material Science*, 26(8), 1991, 2173-2183.
68. P. Das, S. K. Samanta, P. Dutta, Rheological behavior of Al-7Si-0.3Mg alloy at mushy state, *Metallurgical and Materials Transactions B*, 46 (3), 2015, pp.1302–1313.
69. L. Zheng and M. Weimin, Effect of pouring temperature on semi-solid slurry of ZL101 alloy prepared by slightly electromagnetic stirring, *China foundry*, 6(1), 2009, 9-14.
70. Y. Birol, Evolution of globular microstructures during processing of aluminum slurries, *Transactions of Non-ferrous Metals Society of China*, 23(1), 2013, 1-6.

71. Y. Birol, A357 thixoforming feedstock produced by cooling slope casting, *Journal of Materials Processing Technology*, 186(1-3), 2007, 94–101.
72. O. Lashkari and R. Ghomashchi: Evolution of primary  $\alpha$ -Al particles during isothermal transformation of rheocast semi-solid metal billets of A356 Al–Si alloy, *Canadian Metallurgical Quarterly*, 53(1), 2014, 47-54.
73. N. Haghdaei, A. Z. Hanzaki, S. H. Manesh, H. R. Abedi and S. B. H. Irani, The semi-solid microstructural evolution of a severely deformed A356 aluminum alloy, *Materials and Design*, 49, 2013, 878–887.
74. H. V. Atkinson and D. Liu, Coarsening rate of microstructure in semi-solid aluminium alloys, *Transactions of Non-ferrous Metals Society of China*, 20(9), 2010, 1672-1676.
75. Q.G. Wang, Microstructural effects on the tensile and fracture behavior of aluminum casting alloys A356/357, *Metallurgical and Materials Transactions A*, 34(12), 2003, 2887-2899.
76. B. S. Barborá, B. Vlastimil and P. Maxim, Properties of Al alloy castings produced by rheocasting method SEED measured by indentation, Brno, Czech Republic, EU, *Metal* 2015.
77. R. Burapa, S. Janudom, T. Chuchep, R. Canyook and J. Wannasin, Effects of primary phase morphology on mechanical properties of Al-Si-Mg-Fe alloy in semi-solid slurry casting process, *Transactions of Non-ferrous Metals Society of China*, 20(3), 2010, 857-861.
78. L. S. Lin, W. S. Sen, Z. Z. Ming, A. N. Ping and M. Y. Wu, Effect of semi-solid processing on microstructure and mechanical properties of 5052 aluminium alloy, *Transactions of Non-ferrous Metals Society of China*, 20(3), 2010, 758-762.
79. L. B. Chao, P. Y. Koo and D. H. Sheng, Effects of rheocasting and heat treatment on microstructure and mechanical properties of A356 alloy, *Materials Science and Engineering A*, 528(3), 2011, 986–995.
80. E. Rabinowicz, *Friction and wear of materials*, Second edition, Wiley, New York, 1995.
81. M. J. Kadhim, PhD thesis, Study of wear in aluminium based alloys, University of Technology, Baghdad, 1982.
82. I. Huchings, *Tribology: friction and wear of engineering materials*, First edition, Butterworth-Heinemann Publisher, 1992.
83. N. P. Suh, *Tribophysics*, Prentice-Hall Publisher, 1986.

84. K. J. Stout, T. G. King and D.J. Whitehouse, Analytical techniques in surface topography and their application to a running in experiment, *Wear*, 43(1), 1977, 99-115.
85. S.A. Kori and M.S. Prabhudev, Sliding wear characteristics of Al-7Si-0.3Mg alloy with minor additions of copper at elevated temperature, *Wear*, 271(5-6), 2011, 680– 688.
86. P. DAS, B. K. Show, A. Rathore and S. K. Samanta, Wear behavior of cooling slope rheocast A356 Al alloy, *Tribology Transactions*, 58(6), 2015, 1054–1066.
87. A. K. Dey, P. Poddar, K. K. Singh and K. L. Sahoo, Mechanical and wear properties of rheocast and conventional gravity die cast A356 alloy, *Materials Science and Engineering A*, 435–436,2006, 521–29.
88. K. S. Alhawaria, M. Z. Omar, M. J. Ghazali, M. S. Salleha and M.N. Mohammed, Wear properties of A356/Al<sub>2</sub>O<sub>3</sub> metal matrix composites produced by semi-solid processing, *Procedia Engineering*. 68, 2013, 186 –192.
89. K. G. B. Kumar, P. G. Mukunda and M. Chakraborty, Influence of grain refinement and modification on dry sliding wear behaviour of Al-7Si and Al-7Si-2.5Cu cast alloys, *Journal of Materials Processing Technology*, 186(1-3), 2007, 236–245.
90. N. V. Thuong, H. Zuhailawati, A. A. Seman, T. D. Huy and B. K. Dhindaw, Microstructural evolution and wear characteristics of equal channel angular pressing processed semi-solid cast hypoeutectic aluminum alloys, *Materials and Design*. 67, 2015, 448–456.
91. P. Falak and B. Niroumand, Rheocasting of an Al–Si alloy, *Scripta Materialia*, 53, 2005, 53–57.
92. M. Cosic and M. Dojcinovic, Microstructural of AlSi18CuMg alloy produced by the rheocasting process, 12<sup>th</sup> International conference on Accomplishments in Electrical and Mechanical Engineering and Information Technology (DEMI 2015), Serbia, 2015.
93. O. Pompe and M. Rettenmayr, Microstructural changes during quenching, *Journal of Crystal Growth*, 192, 1998, 300-306.
94. M. M. Kaykha, A. Kamarei, M. Safari and V. Arbabi, Semi-solid structure and parameters for A360 aluminum alloy prepared by mechanical stirring, *World Academy of Science, Engineering and Technology, International Scholarly and Scientific Research and Innovation* 5(1), 2011, 674-676.
95. H. Mirzadeh and B. Niroumand, Effects of rheocasting parameters on the microstructure of rheo-centrifuged cast Al-7.1 wt%Si alloy, *Journal of Alloy and Compound*. 474, 2009, 257–263.

96. M. Reisi and B. Niroumand, Effects of stirring parameters on rheocast structure of Al–7.1wt.% Si alloy, *Journal of Alloy and Compound*, 470,2009, 413–419.
97. H. S. Dou, B. C. Khoo and K. S. Yeo, Instability of Taylor-Couette flow between concentric, rotating cylinders, *International Journal of Thermal Science*, 47(11), 2008, 1422-1435.
98. P. J. W. Roberts and D. R. Webster, *Turbulent diffusion in environmental fluid mechanics theories and application*, ASCE, Reston, USA, 2002, 1-42.
99. P. Melali, P. Ashtijoo and B. Niroumand, Effect of stirring speed and flow pattern on the microstructure of a rheocast Al-Mg alloy, *Metallurgical Materials Engineering*, 21(1), 2015, 35-43.
- 100.S. Ji and Z. Fan, Solidification behavior of Sn-15 wt.% Pb alloy under a high shear rate and high intensity of turbulence during semi-solid processing, *Metallurgical and Materials Transactions A*, 33(A), 2002, 1-10.
- 101.B. Niroumand and K. Xia, *Proceedings of the 8<sup>th</sup> International Conference on Semi-Solid Processing of Alloys and Composites*, Cyprus, 2004.
- 102.P. S. Mohanty, R. L. Guthrie and J. E. Gruzleski, Studies on addition of inclusions to molten aluminium using a novel technique, *Metallurgical and Materials Transactions B*,26, 1995, 103–110.
- 103.Z. Fan and G. Liu, Solidification behavior of AZ91D alloy under intensive forced convection in the RDC process, *Acta Materialia*, 53, 2005, 4345–4357
- 104.A. H. Ardakan and F. Ajersch, Effect of conventional and rheocasting processes on microstructural characteristics of hypereutectic Al–Si–Cu–Mg alloy with variable Mg content, *Journal of Material Processing Technology*, 210, 2010, 767–775.
- 105.S. Nafisi and R. Ghomashchi, Effects of modification during conventional and semi-solid metal processing of A356 Al-Si alloy, *Material Science and Engineering A*, 415, 2006, 273–285.
- 106.M. Perez, Gibbs–Thomson effects in phase transformations, *Journal of Scripta Materialia*, 52, 2005, 709-712.
- 107.A. Baldan, Progress in Ostwald ripening theories and their applications to nickel-base super alloys, *Journal of Materials Science*, 37(11), 2002, 2171–2202.
- 108.M. Hitchcock and Z. Fan, Solidification behavior under intensive forced convection, *Journal of Material Science Forum*, 519–521, 2006, 1747–1752.

- 109.S. Terzi, L. Salvo, M. Suery and A. K. Dahle, Coarsening mechanisms during isothermal holding of a dendritic Al-10wt%Cu alloy, *Transactions of Indian Institute of Metals*, 62, 2009, 447-449.
- 110.P. W. Voorhees and L. Ratke, *Growth and coarsening*, Berlin, Springer, 2002.
- 111.M. Ramadan and N. Fathy, Solidification microstructure of rheocast hyper-eutectic Al-18Si alloy, *Journal of Metallurgical Engineering*, 2(4), 2013, 149-154.
- 112.A. Jain, L. Ratke and A. Sharma, Non-dendritic structural changes in Al-7Si alloy cast through rapid slurry formation (RSF) process, *Transactions of Indian Institute of Metals*, 65(6), 2012, 545-551.
- 113.H. Kaufmann, H. Wabusseg and P.J. Uggowitzzer, Metallurgical and processing aspects of the NRC semi-solid casting technology, *Aluminium*, 76(1-2), 2000,70-75.
- 114.E. J. Zoqui, M. T. Shehata, M. Paes, V. Kao and E. E. Sadiqi, Morphological evolution of SSM A356 during partial remelting, *Materials Science and Engineering A*, 325, 2002, 38-53.
- 115.L. Ratke and M. Host, Convective contributions to Ostwald ripening in dispersions at low Peclet numbers, *Journal of Colloid Interface Science*, 141(1), 1991, 226-238.
- 116.S. Takajo, W. A. Kaysser and G. Petzow, Analysis of particle growth by coalescence during liquid phase sintering, *Acta Metallurgica*. 32(1), 1984, 107-113.
- 117.M. Ostklint, M. Wessen and A. Jarfors, Microstructure and material soundness in liquidand rheocast AM50 and effect of section thickness, *International Journal of Cast Metals Research*, 27(4), 2014, 235-241.
- 118.K. Sukumaran, B. C. Pai and M. Chakraborty, The effect of isothermal mechanical stirring on Al-Si alloy in the semi-solid condition, *Journal of Material Science and Engineering A*, 369, 2004, 275-283.
- 119.M. Emamy, A.R. Daman, R. Taghiabadi and M. Mahmudi, Effects of Zr, Ti and B on structure and tensile properties of Al-10Mg alloy (A350). *International Journal of Cast Metals Research*, 17, 2004, 1-17.
- 120.G. S. V. Kumar, B. S. Murthy and M. Chakraborty, Development of Al-Ti-C grain refiner and study of their grain refining efficiency on Al and Al-7Si alloy. *Journal of Alloys Compounds*, 396, 2005, 143-150.
- 121.N. Iqbal, N. H. V. Dijik, S. E. Offerman, M. P. Moret, L. Katgerman and G. J. Kearley, Real-time observation of grain nucleation and growth during solidification of aluminium alloys, *Acta Materialia*, 53(10), 2005, 2875-2880.

122. G. L. Liu, N. C. Si, S. C. Sun and Q. F. Wu, Effects of grain refining and modification on mechanical properties and microstructures of Al-7.5Si-4Cu cast alloy, *Transactions of Non-ferrous Metals Society of China*, 24, 2014, 946-953.
123. D. Gloria, PhD Thesis, Control of grain refinement of Al-Si alloys by thermal analysis, McGill University, Montreal, Canada, 1999.
124. A. B. Pattnaika, S. Das, B. B. Jha and N. Prasanth, Effect of Al-5Ti-1B grain refiner on the microstructure, mechanical properties and acoustic emission characteristics of Al5052 aluminium alloy, *Journal of Material Research and Technology*, 4(2), 2015, 71-179.
125. P. Das, S. K. Samanta and P. Dutta, Rheological behavior of Al-7Si-0.3Mg alloy at mushy state, *Metallurgical and Materials Transactions B*, 46(3), 2015, 1302-1313.
126. D. Zhang, PhD Thesis, Thermodynamic characterization of semi-solid process ability in alloys based on Al-Si, Al-Cu and Al-Mg binary systems, University of Leicester, 2015.
127. B. Binesh and M. A. Khafri, Phase evolution and mechanical behavior of the semi-solid SIMA processed 7075 aluminum alloy, *Metals*, 42(6), 2016, 1-23.
128. A. Vencel, L. Bobic and Z. Miskovic, Effect of thixocasting and heat treatment on the tribological properties of hypoeutectic Al-Si alloy, *Wear*, 264(7-8), 2008, 616-623.
129. G. T. Zeru, PhD thesis, Development of recycle-friendly secondary cast aluminium alloy for cylinder head applications, Jomo Kenyatta University of Agriculture and Technology, 2014.
130. S. R. Sharma, Z. Y. Ma and R.S. Mishra, Effect of friction stir processing on fatigue behavior of A356 alloy, *Scripta Materialia* 51(3), 2004, 237-241.
131. C. J. Chen, PhD thesis, Optimization of mechanical properties in A356 via simulation and permanent mold test-bars, Case Western Reserve University, 2014.
132. S. Lu, S. Wu, W. Dai, C. Lin and P. An, The indirect ultrasonic vibration process for rheo squeeze casting of A356 aluminum alloy, *Journal of Materials Processing Technology*, 212(6), 2012, 1281-1287.
133. G. Zhihua, X. Junb, Z. Zhifeng, L. Guojun and T. Mengou, Study on rheo-die casting process of 7075R alloys by SA-EMS melt homogenized treatment, 4th International Conference on Advances in Solidification Processes (ICASP-4), IOP Conf. Series: Materials Science and Engineering, 117, 2016, 1-6.
134. M. Rosso, I. Peter and R. Villa, Effects of T5 and T6 heat treatments applied to rheocast a356 parts for automotive applications, *Solid State Phenomena*, 141-143, 2008, 237-242.

- 135.M. Brochu, Y. Verreman, F. Ajersch and D. Bouchard, High cycle fatigue strength of permanent mold and rheocast aluminum 357 alloy, *International Journal of Fatigue* 32(8), 2010, 1233–1242.
- 136.J. H. Li, M. Z. Zarif, M. Albu, B. J. McKay, F. Hofer and P. Schumacher, Nucleation kinetics of entrained eutectic Si in Al–5Si alloys, *Acta Materialia*, 72, 2014, 80–98.
- 137.P. Moldovan, G. Popescu and M. Buțu, Heat treatment of Al-7Si-0.3Mg alloy previously inoculated with a new type of quaternary master alloy, *UPB Scientific Bulletin, Series B: Chemistry and Materials Science*, 69(2), 2007, 91-98.
- 138.H. Moller, G. Govender, W. E. Stump and R. D. Knutsen, Influence of temper condition on microstructure and mechanical properties of semi-solid metal processed Al–Si–Mg alloy A356, *International Journal of Cast Metals Research*, 22(6), 2009, 417-421.
- 139.G. Hongmin, Y. Xiangjie, H. Bin and Z. Guanglei, Rheo-diecasting process for semi-solid aluminium alloys, *Journal of Wuhan University of Technology-Material Science Edition*, 22(4), 2007, 590-595.
- 140.B. A. Dewhurst, MSc thesis, Optimization of the heat treatment of semi-solid processed A356 aluminum alloy, Worcester Polytechnic Institute, Worcester, Massachusetts, 2005.
- 141.E. Ogris, PhD thesis, Development of Al-Si-Mg alloys for semi-solid processing and silicon spheroidization treatment (SST) for Al-Si Cast Alloys, Swiss Federal Institute of Technology Zurich, 2002.
- 142.S. M. Jigajinni, K. Venkateswarlu and S. A. Kori, Effect of a grain refiner cum modifier on mechanical properties of Al-7Si and Al-11Si alloys, *Metals and Materials International*, 19(2), 2013, pp. 171-181.
- 143.A. Sharma and T. V. Rajan, Scanning electron microscopic studies of worn out leaded aluminium silicon alloy surfaces, *Wear*, 174, 1994, 217-228.
- 144.P. C. Meena, A. Sharma and S. Singh, Effect of grain refinement on microstructure and wear behavior of cast Al-7Si alloys, *La Metallurgia Italy*, 1, 2015, 25-34.
- 145.G. Xue, MSc thesis, Tribological studies of eutectic Al-Si alloys used for automotive engine blocks subjected to sliding wear damage, University of Windsor, Ontario, Canada, 2009.
- 146.M. Alipour, B. G. Aghdam, H. E. Rahnoma and M. Emamy, Investigation of the effect of Al–5Ti–1B grain refiner on dry sliding wear behavior of an Al–Zn–Mg–Cu alloy formed by strain-induced melt activation process, *Materials and Design*. 46, 2013, 766–75.

147.F. U. Ozioko, Synthesis and study on effect of parameters on dry sliding wear characteristics of Al-Si alloys, Leonardo Electronic Journal of Practices and Technologies, 20, 2012, 39-48.

## Appendix I

### Charge calculation for preparation of A356 alloy

For the production of 3Kg of Al-7Si alloy the raw material are following:

- Master alloy (Al-13%Si), let assume the value = x
- Pure Al = y

1) Calculating the amount of master alloy required for balance the Si weight in 3 Kg of Al-7Si

The total weight of Si =  $3 \times 7/100 = 0.210$  kg

But the weight of Si in master alloy (Al-13%Si) =  $x \times 13/100$

So by balancing the Si weight:

$$13/100 \times x = 0.210$$

$$x = 0.210 \times 100/13 = 1.62 \text{ kg}$$

The total weight of mater alloy (x) = 1.62 kg

2) The amount of pure Al required is obtained by balancing the weight of Al:

$$\text{Total Al in alloy (Al-7Si)} = 93/100 \times 3 = 2.79 \text{ kg} \quad (1)$$

But the total weight of Al that is required for this alloy, is the sum of Al in master alloy and

$$\text{pure Al that is added} = 1.62 \times 87/100 + y \quad (2)$$

By equating, equations (1) and (2):

$$93/1000 \times 4 = 1.62 \times 87/100 + y$$

$$2.79 = 1.41 + y$$

$$y = 1.38 \text{ kg}$$



Thus, pure Al required is 1.38 kg

## Appendix 2

(i) The calculations for mass of EEM required for preparing 30 wt.% solid fraction

$$M_{\text{melt}} = 1.35 \text{ kg}$$

$$T_o^{\text{melt}} = 700^\circ\text{C} = 700+273 = 973\text{K}$$

$$T_o^{\text{eem}} = 35^\circ\text{C} = 35+273 = 308\text{K}$$

$$C_{p \text{ melt}} = C_{p \text{ eem}} = 0.896 \text{ kJ/kg} - \text{K}$$

$$k = 0.132$$

$$m_L = 6.58$$

$$C_o = 7\text{wt.}\%$$

$$f_s = 30\text{wt.}\%$$

Calculating the semi-solid temperature by Scheil's Equation:

$$T_{\text{SSM}} = T_f - (T_f - T_L)(1 - f_s)^{(k-1)} \quad (3)$$

Where;

$T_f$  = melting point,

$T_L$  = Liquidus temperature

$$T_f = 660^\circ\text{C} = 660+273 = 933 \text{ K}$$

Writing equation of straight line for liquidus line,

$$T_L = T_f - m_L C_o$$

$$T_L = 933 - 6.58(7) = 886.94 \text{ K} \quad (4)$$

Now substitute all the values in Eq.(3)

$$T_{SSM} = 933 - (933 - 886.94) (1 - 0.3) (0.132 - 1)$$

$$T_{SSM} = 870.17\text{K} = 597.17^\circ\text{C}$$

The principle of enthalpy exchange between the two different enthalpy levels can be given by the following equation Using equation

$$Q_{in} = Q_{out}$$

$$\begin{aligned} m_{melt} C_{p \text{ melt}} (T_{melt} - T_{SSM}) + \Delta H_{melt} m_{melt} f_s \\ = m_{EEM} C_{p \text{ EEM}} (T_{SSM} - T_{EEM}) + \Delta H_{EEM} m_{EEM} (1 - f_s) \end{aligned}$$

$$m_{eem} = m_{melt} \frac{[C_{p \text{ melt}} (T_{melt} - T_{SSM}) + \Delta H_{melt} f_s]}{[C_{p \text{ EEM}} (T_{SSM} - T_{EEM}) + \Delta H_{EEM} (1 - f_s)]} \quad (5)$$

$$m_{eem} = 1.35 \frac{[0.896(973 - 870.17) + 0.3(439)]}{[0.896(870.17 - 308) + 0.7(439)]}$$

$$m_{eem} = 0.3726 \text{ kg}$$

This is total weight required for preparing 30 wt.% solid fraction.

**(ii) For 20 wt.% solid fraction**

Similarly the weight of EEM required for preparing solid fraction of 20wt.% can be calculated using above equation. All the values except that of  $f_s$  remain constant. The mass required

$$m_{eem} = 0.264 \text{ kg}$$

**(iii) For 40 wt.% solid fraction**

$$m_{eem} = 0.496 \text{ kg}$$

### Appendix 3

#### Calculations for Reynolds number

$$(Re) = \rho v D / \mu \quad (6)$$

Where;

$\rho$  = density of A356 alloy (2685kg/m<sup>3</sup>),

D = characteristic diameter (0.05m),

$\mu$  = dynamic viscosity (0.008782 Pa.s)

v = velocity ( $\pi D N / 60$ ),

N = stirring speed (rpm)

**(i) For stirring speed = 400 rpm**

$$v = 3.14 \times 0.05 \times 400 / 60$$

$$v = 1.046 \text{ m/sec.}$$

Now substitute all values in Eq.(6)

$$Re = 2685 \times 1.046 \times 0.05 / 0.008782$$

$$Re = 16000$$

Similarly Reynolds number can be calculated for high stirring speed.

Stirring speed (rpm)	Reynolds number
400	16000
600	24000
800	32000
1000	40000
1200	48000

#### Appendix 4

Parameters of the Diffusive-LSW theory used for calculating the theoretical value of coarsening rate constant.

Sr. No.	Parameter	Value
1	Atomic weight(g/mol)	26.98
2	Density(g/cm <sup>3</sup> )	2.685
3	D <sub>0</sub> (m <sup>2</sup> /s)	8.42*10 <sup>-8</sup>
4	Q(KJ/mol)	23.2
5	R(J/mol/K)	8.314472
6	T(K)	870.15
7	V(m <sup>3</sup> /mol)	1.01x10 <sup>-5</sup>
8	δ(J/m <sup>2</sup> )	0.16
9	ΔH <sub>f</sub> (KJ/mol)	439
10	m <sub>L</sub> (K/%Al)	6.58
11	C <sub>s</sub> (%Al)	98.75
12	C <sub>L</sub> (%Al)	90.44
13	α <sup>3</sup>	51.93

## Appendix 5

### Calculations for $K_{\text{calculated}}$ used in diffusive mass flow

These are the calculations for 30wt.% solid fraction.

$$D_M^3 - D_0^3 = K_{fs} K_{LSW} (t - t_0)$$

$$K_{\text{calc}} = K(f_s) \times K_{LSW}$$

$$K_{LSW} = \frac{8\Gamma d T_0}{9m_L(C_s - C_L)}$$

$$\Gamma = \frac{V_m \delta}{\Delta H_f}$$

$$\Gamma = \frac{1.01 \times 10^{-5} \times 0.16}{439000} = 3.68 \times 10^{-12} \text{ m}$$

$$K_{LSW} = \frac{8 \times 3.68 \times 10^{-12} \times (8.42 \times 10^{-8} \times e^{-\frac{23200}{8.314 \times 870}}) \times 870}{9 \times 6.58 \times (98.75 - 90.44)}$$

$$K_{LSW} = \frac{8 \times 3.68 \times 10^{-12} \times 3.533 \times 10^{-9} \times 870}{9 \times 6.58 \times (98.75 - 90.44)}$$

$$K_{LSW} = 1.8 \times 10^{-19} \text{ m}^3/\text{sec} = 0.18 \text{ } \mu\text{m}^3/\text{sec}.$$

Now,

$$K(f_s) = 1 + 3.78\sqrt{f_s} - 6.5f_s^2 + 21.79f_s^3$$

Here  $f_s=0.3$

$$K(f_s) = 3.07$$

$$K_{\text{calc}} = K(f_s) \times K_{LSW} = 3.07 \times 0.18 = 0.6146 \mu\text{m}^3/\text{sec}.$$

$$K_{\text{calculated}} = 0.5526 \mu\text{m}^3/\text{sec}.$$

## Appendix 6

### Calculations for $K_{\text{calculated}}$ used in convective mass flow

These are the calculations for 30wt.% solid fraction.

$$D^2 - D_0^2 = AK_{LSW} \frac{(1 - f_s)^{2/3}}{f_s} \omega^{1/3} t$$

$$K_{\text{calc}} = AK_{LSW} \frac{(1 - f_s)^{2/3}}{f_s} \omega^{1/3}$$

$$K_{LSW} = 0.18 \mu\text{m}^3/\text{sec}. \text{ (Refer from above)}$$

$$A = D_0 e^{-Q/RT}$$

$$A = 8.42 \times 10^{-8} e^{-23200/(8.314 \times 870)} = 3.173 \times 10^{-9} \text{ m}^2/\text{s} = 3.173 \times 10^3 \mu\text{m}^2/\text{s}.$$

### For 400 rpm

$$K_{\text{calc}} = 3.173 \times 10^3 \times 0.18 \frac{(1 - 0.3)^{2/3}}{0.3} \left(\frac{400}{60}\right)^{1/3}$$

$$K_{\text{calc}} = 2750 \mu\text{m}^2/\text{s}.$$

Similarly calculations of  $K_{\text{calc}}$  can be carried out for higher shear rate i.e. 600, 800, 1000 and 1200.

Coarsening rate constant due to convective mass flow (K)

Shear rate	$K_{\text{calc}}(\mu\text{m}^2/\text{sec}.)$
------------	--

400	2750
600	3145
800	3460
1000	3723
1200	3963

## Appendix 7

### List of Publication from this Research work

- **R. Gupta, A. Sharma, U. Pandel, L. Ratke**, “Effect of varying shear force on microstructure of A356 alloy cast through rheometal process”, International Journal of Material Research, 108, 2017, 648-655.
- **R. Gupta, A. Sharma, U. Pandel, L. Ratke**, “Wear analysis of A356 alloy cast through rheometal process”, Material Research Express, 4, 2017, 1-11.
- **R. Gupta, A. Sharma, U. Pandel, L. Ratke**, “Effect of heat treatment on microstructure and mechanical properties of A356 alloy cast through rapid slurry formation (RSF) process”, International Journal of Cast Metals Research, 30, 2017, 283-292.
- **R. Gupta, A. Sharma, U. Pandel, L. Ratke**, “Coarsening kinetics in Al alloy cast through rapid slurry formation (RSF) process”, Acta Metallurgica Slovaca, 23, 2017, 12-21.

### Conference publications

- **R. Gupta, A. Sharma, L. Ratke**, “An overview of rheological behavior of aluminium alloys in semisolid state”, National Conference on Recent Trends in Materials Engineering (RTME), Bahal, Harayana, 2013.

### Other publications

- **R. Gupta, A. Sharma, U. Pandel, L. Ratke**, “Evolution of microstructure in Al-Si alloy cast through rapid slurry formation (RSF) process”, poster presentation at NMD-ATM, Pune, 2014.
- **A. Sharma, R. Gupta, L. Ratke**, “Study of microstructure characteristics of Al-7%Si alloy cast through rheo-metal process”, International Conference on Material Science and Technology (MST) 2014, Pittsburgh, USA, 2014.